Light Management and Optical Loss Mitigation for Photovoltaics: Downshifting, Downconversion, and Tandem Solar Cell Designs

A THESIS SUBMITTED TO THE FACULTY OF THE UNIVERSITY
OF MINNESOTA BY

John William Keil

IN PARTIAL FULFILLMENT OF THE REQUIREMENTS FOR THE
DEGREE OF DOCTOR OF PHILOSOPHY

Vivian E. Ferry, Advisor

July, 2023

Acknowledgments

My success at graduate school would not have been possible without the help of numerous people. First, I would like to thank my advisor, Vivian E. Ferry. Her guidance and support helped me grow as a scientist and engineer, and I have learned valuable research, writing, presentation, and teamwork skills from her that I will carry with me into my future career. Her passion and enthusiasm for research and discovery is inspiring, and I am grateful to have been a part of her group.

My research on luminescent solar concentrators (LSC) involved collaboration from other brilliant scientists who I would like to thank and recognize. I thank Yaling Liu, who I worked closely with on the LSC project. I enjoyed our teamwork and collaboration, and Yaling's drive and positivity helped made the project a great success. I would like to thank Uwe Kortshagen. My work on LSCs benefited greatly from his mentorship, insight, and expertise. I also thank Lorraine Francis, who provided much needed support on film fabrication and processing. Much of the fabrication work would not have been possible without her guidance. I thank Colin Peterson from Marc Hillmyer's group for synthesizing polymer material used in my research.

During my time at the University of Minnesota, I worked alongside many talented members of the Ferry Group. I would like to thank Ryan Connell who I worked closely with when first joining the Ferry group. I learned a lot from him during the first six months of my time in the group, and he helped me quickly grow as a researcher. I would like to thank Eleanor Mayes for teamwork and support during classes and qualifying exams. I thank Bryan Cote who started the research on the CdTe/Si tandem project. He laid a great foundation on what turned out to be an excellent project, and provided guidance on the Lumerical simulations. I thank Diana Hoernemann and Hannah Pichman who worked with me as undergrads on modeling and fabricating LSCs. I thank Michael Hamann, Elizabeth Myers, and Anca Moisei who I mentored at visiting teachers conducting research in our

group during the summer. I would like to give a big thanks to all other Ferry group members who I have had the privilege to know during my time at graduate school: Dana Dement, Matthew Quan, Pavlos Pachidis, Ian Slauch, Eleanor Mayes, Maya Ramamurthy, Rohan Chakraborty, Kristine Loh, Emily McGuinness, Teslim Fasasi, Yidnek Donie, Jay Chung, and Clare Froehlich. I am grateful for the support I received and friendships I formed in the Ferry group. It made my graduate school experience exceptional. I would also like to thank the undergraduate students who have worked in the group including Chris Stallard, Adriana Chapa, Jessica Chui, Jackson Muehlbauer, and Renuka Bhatt.

I have had the privilege to collaborate with industry sponsors on multiple projects who provided expertise and support. I would like to thank Daniel Kroupa and Jared Silvia from who provided industry perspective and expertise on quantum-cutting perovskite materials. I am grateful I had the opportunity to work with them on the downconversion project and help meet some of their technical goals. I thank Adrei Los, Vinodh Chandrasekaran, Dirk Weiss, and Yongjie Zou from First Solar. Our collaboration on the CdTe/Si tandem project helped make the research successful and impactful. A special thanks to Andrei and Vinodh for their feedback on the manuscript.

I would like to thank my friends and family. I am very grateful for the amazing friendships I formed during my time as a graduate student. They helped keep me grounded and positive during more difficult periods of graduate school. I will always remember the support they gave and all the fun experiences we had together in Minneapolis. I thank my family for the unconditional love and support they provided toward my academic endeavors. They are always willing to listen and help me any way they can.

Lastly, I would like to thank my boyfriend and partner, Zach Moser. He has been with me every step of the way throughout my graduate school career and has endless love and compassion. He encouraged me to take care of myself and always believed in me. The work presented here would not have been possible without him.

Abstract

The efficiency of single-junction Si photovoltaic cells has continually increased over the past several decades, but is approaching fundamental thermodynamic limits. Holding over 95% of the solar module market share, Si modules will continue to be an integral part of the rapidly expanding photovoltaic industry, so different device technologies that increase Si cell efficiencies beyond thermodynamic limits, or that expand the available installation sites for solar cells, are needed.

In this thesis, three types of technologies are discussed that use optical design to more efficiently use the high energy solar spectrum for Si PV: downshifting, downconversion, and tandem solar cells. We first discuss the design of downshifting and concentrating devices called luminescent solar concentrators (LSCs). Tandem LSC architectures, which combine multiple luminophores to broaden the absorption spectrum, are one potential route to increase the efficiency of these devices. We first describe an analytical model to develop luminophore selection criteria for tandem LSCs. We find that luminophores with high photoluminescent quantum yield, minimal overlap between the absorption and photoluminescence spectrum, and an absorption onset closely matched to the band gap of the chosen photovoltaic cell yield the best LSC performance. We then create bilayer LSCs, which combine CdSe/CdS and Si nanocrystals in a monolithic waveguide. Through a combination of transmission measurements, position-dependent photoluminescence measurements, and ray-tracing simulations, the bilayer LSC was found to sensitize Si nanocrystal absorption and enhance the optical efficiency by 30% relative to a single layer LSC. We discuss the use of the bilayer device in agrivoltaic applications, and then explore this use further using a thin-film stack optimization methods to direct emission out one LSC side toward the plant species. The LSC extraction efficiency is increased from 13.9% to 15.1%.

We next consider optical designs for downconversion, a process by which one high energy photon is converted into two lower energy photons. We consider the coupling efficiency from the downconverter to a realistic Si solar module in several different configurations, finding an optical coupling efficiency of 95.25% by placing the downconverting film directly on the Si cell. This enhances the power conversion efficiency by 2% absolute.

Lastly, CdTe/Si four-terminal tandem solar cells are studied to improve the sub-band gap transparency of CdTe solar cells. We find that the surface texture of the CdTe significantly impacts light transmission into the Si bottom cell, and that the losses are dominated by the transparent conductive oxide absorption. An optical design solution is proposed that mitigates transparency loss and enhances the short circuit current density of the Si cell by 2.5 mA/cm^2, which enhances the tandem efficiency by a relative increase of 5.6%.

Contents

List of Figures

List of Tables

List of Publications

Portions of this thesis are drawn with permission from:

J. Keil, Y. Liu, U. Kortshagen, and V. E. Ferry, “Evaluating Tandem Luminescent Solar Concentrator Performance Based on Luminophore Selection,” in “2021 IEEE 48th Photovoltaic Specialist Conference (PVSC),” (2021), pp. 1680-1684.

J. Keil, Y. Liu, U, Kortshagen, and V. E. Ferry, “Bilayer Luminescent Solar Concentrators with Enhanced Absorption and Efficiency for Agrivoltaic Applications,” ACS Applied Energy Materials 4, 14102-14110 (2021).

J. Keil, B. M. Cote, V. Chandrasekaran, A. Los, and V. E. Ferry, “Minimizing Roughness Induced Optical Losses for a Four-Terminal CdTe/Si Tandem Solar Cell,” PRX Energy 2, 023004 (2023).

Chapter 1

Introduction

1.1 Motivation for Light Management in Si Solar Cells

The past several decades have seen an impressive rise in single junction silicon (Si) photovoltaic (PV) cell efficiency, along with decreased levelized cost of energy (LCOE). Utility scale PV plants are now often less expensive than fossil fuel generators [1]. The increased efficiency arises from the maturity of both technology and manufacturing that has resulted in low-cost, large-volume fabrication of high efficiency devices like the passivated emitted and rear contact (PERC) cell [1]. Crystalline Si (c-Si) modules hold over 95% market share, and will continue to lead PV installations during the energy transition [2, 3]. However, the efficiency of Si solar cells is approaching fundamental thermodynamic limits that cannot be surpassed without fundamentally different device technologies (Figure 1.1) [4].

In addition to increases in efficiency, rapidly expanding PV installations in a variety of sites require different form factors and aesthetics. The global PV capacity additions grew from 17 GW direct current (GWdc) to 172 GWdc from 2010 to 2021, and exponential growth is expected to continue through the next decade [2]. Utility scale, commercial and industrial, and residential PV represents 64%, 12%, and 24% of U.S. cumulative PV capacity at the end of 2022 according to the U.S. Energy Information Administration reports [5], and residential PV includes the vast majority of individual installations. The

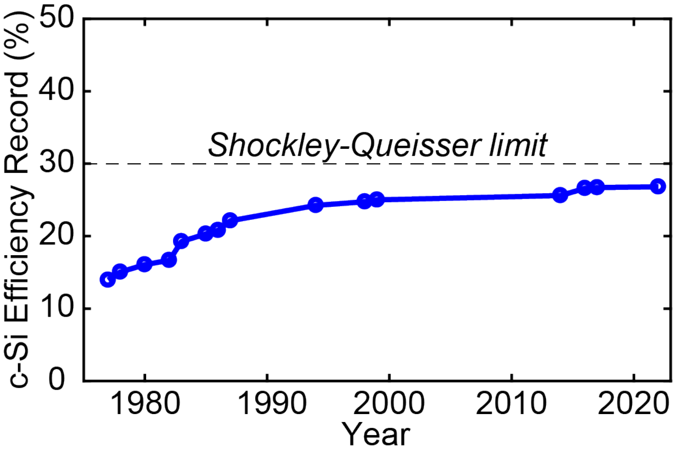

Figure 1.1: Single junction c-Si efficiency record since 1976 with the Shockley-Queisser limit as the reference line. Efficiency data is courtesy of National Renewable Energy Laboratory, Golden, CO.

available installation sites are greatly expanded for transparent PV technologies [1].

A key limitation in single junction Si PV is poor utilization of blue and ultraviolet (UV) light, because most of the energy from blue and UV photons are lost to thermalization and not converted to electricity [6]. Potential strategies to overcome this limitation include downconversion, downshifting, and tandem solar cells [1, 7, 8]. Energy diagrams demonstrating each of these concepts are depicted in Figure 1.2. Downconversion is a process by which a single high-energy blue or UV photon is converted to two lower-energy photons. The benefits to solar cell efficiency arise from both the shift in the spectrum and photon multiplication. Photons with energy greater than the semiconductor band gap that would normally be lost to thermalization or in some cases absorbed by encapsulants, are converted into photons with energies that are spectrally matched to the band gap of the solar cell and, therefore, more efficiently converted to electricity. If designed correctly, the photon multiplication could generate a higher photocurrent and increase the maximum conversion efficiency to exceed the Shockley-Queisser limit [9–13].

Downshifting is another concept, which does not break the Shockley-Queisser limit, but can be useful when applied to PV technologies. Here, the inefficiently used, high-energy photons are shifted to lower energy photons that are matched to the solar cell band gap in a 1:1, absorption and photoluminescence (PL) process. This concept is often implemented in

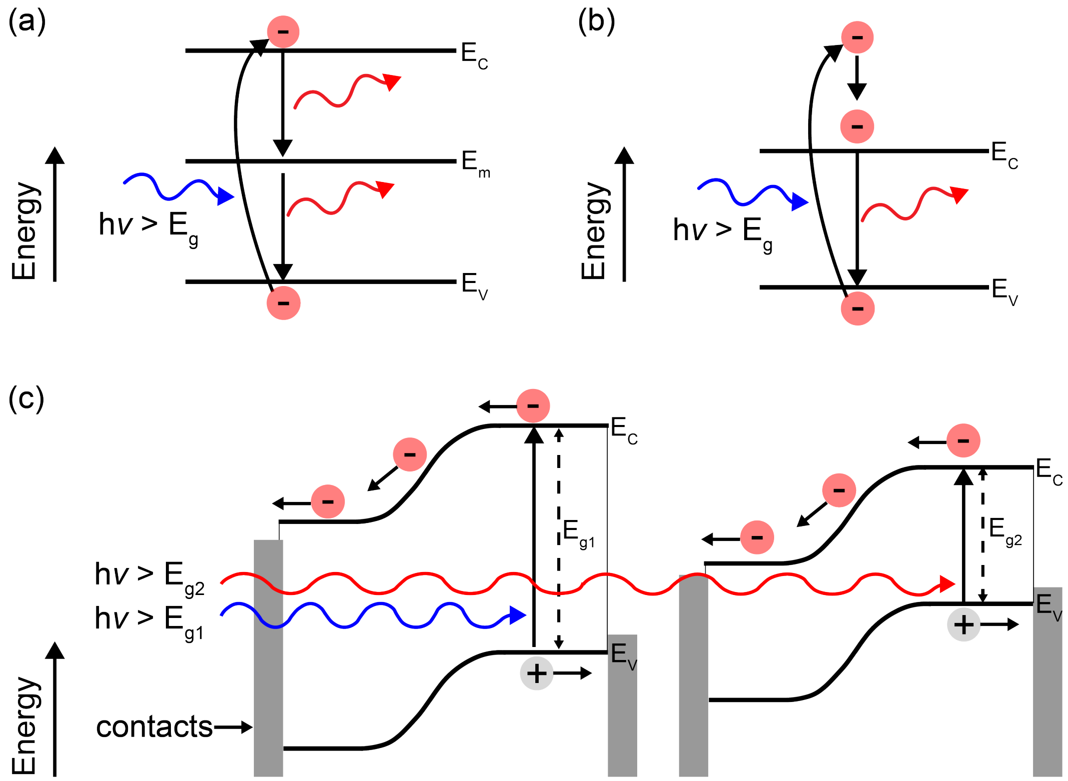

Figure 1.2: Energy diagrams depicting (a) downconversion, (b) downshifting, and (c) a tandem solar cell. The red minuses represent electrons, the gray pluses represent holes, and the colored arrows represent photons. E_C, E_V, *and* E_m *represent the conduction band, valence band, and midgap state.*

a device called a luminescent solar concentrator (LSC), which is designed to absorb direct and diffuse higher energy sunlight, shift the sunlight to a more ideal, narrow spectral range, and concentrate that light onto small area PV cells [14]. An LSC consists of luminophores embedded inside an optically transparent waveguide, with PV cells typically mounted on the sides. Since LSCs are semitransparent, they can be installed in building integrated or agrivoltaic applications [15].

Tandem solar cells split the spectrum by combining two solar cells of different band gaps to utilize the higher energy light more efficiently. The wider band gap sub-cell absorbs higher energy photons and transmits lower energy photons to the narrow band gap sub-cell, which reduces thermalization and more efficiently utilizes the solar spectrum. The efficiency can be further enhanced because each sub-cell can be optimized to a narrower spectrum. This technology can yield impressively high efficiencies with the current efficiency record of 33.2% achieved with a perovskite/Si tandem cell [16, 17].

All three of these cases, which use optical effects to improve on the efficiency of single junction Si solar cells through more efficient utilization of the blue and UV portions of the spectrum, require detailed understanding of the optical processes in realistic configurations, as discussed throughout this thesis.

1.2 Solar Cell Operation Principles and Efficiency

Before we begin, it is important to understand the working principles of PV cells. In the most basic form, a solar cell is a device that converts sunlight to electricity via the photovoltaic effect [6, 18], which can be broken down into three parts: optical absorption, charge carrier separation, and charge carrier collection. A schematic of the photovoltaic process is seen in figure 1.3. When incident sunlight with energy greater than the semiconductor band gap is incident on the solar cell, it can be absorbed, which excites a negatively charged electron from the valence band to the conduction band, leaving behind a positively charged hole. In a typical semiconductor, after the generation of the electron-hole pair from optical

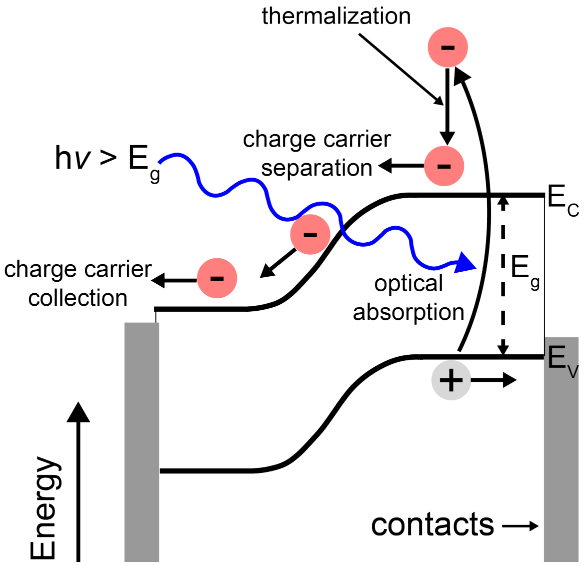

Figure 1.3: Energy diagram depicting a single junction solar cell and the photovoltaic effect.

absorption, the charge carriers will usually recombine. In a solar cell, however, the electron and hole flow in opposite directions toward the contacts, where they can be extracted and perform work in an external circuit [6, 18]. If the absorbed energy is significantly in excess of the bandgap, as seen in Figure 1.3, then the carriers relax to the band edge, a process known as thermalization.

The power conversion efficiency (η_{PV}) of a solar cell is defined as the ratio between the maximum generated power and the incident power, and can be described by Equation 1.1.

$$\eta_{PV} = \frac{J_{SC}\,FF\,V_{OC}}{I_{in}} \tag{1.1}$$

J_{SC} is the short circuit current density, FF is the fill factor, V_{OC} is the open circuit voltage, and I_{in} is the incident power. The upper theoretical limit for solar cell efficiency was determined in 1961 by Shockley and Queisser [4]. Assuming illumination from a blackbody source at 6000 K, the Si band gap of 1.1 eV, and a single junction device configuration, the upper efficiency limit is 30% [4]. Under the AM1.5G standard solar spectrum, the efficiency limit is 32.2% [19].

1.3 Downshifting and Luminescent Solar Concentrators

1.3.1 Downshifting for Improved Spectral Response

We begin by considering the downshifting process. Downshifting is achieved with photoluminescent luminophores such as semiconducting nanocrystals, organic dyes, and phosphors. Semiconductor nanocrystals are particles with dimensions between 1 and 100 nm that bridge the gap between molecules and bulk materials [20]. Due to their nanoscale size, semiconductor nanocrystals exhibit quantum confinement effects that lead to discrete energy transitions and a size-dependent band gap [20–22]. Organic dyes are small molecules that have electronic transitions that allow for the absorption and emission of downshifted light [23–25]. They typically have a narrower absorption band than nanocrystals, but can exhibit high absorption coefficients and can be easily dispersed in polymers [25]. Fluorescent phosphors are typically inorganic materials intentionally doped with impurities. Absorption can take place in the host or the impurities, but the radiative energy transition usually originates from the impurities [25, 26]. All these downshifting materials have been studied extensively for uses in photovoltaic applications to improve the blue and UV spectral response or create semitransparent light harvesting devices [21, 27–40].

Downshifting has a maximum photoluminescence quantum yield (η_{PLQY}) of 100%, but can have a broader absorption spectrum than downconversion (Section 1.4) while still emitting light useful for photovoltaic conversion. η_{PLQY} is defined by Equation 1.2, where Γ is the radiative decay rate of the luminophore, and k_{nr} is the non-radiative decay rate [41].

$$\eta_{PLQY} = \frac{\Gamma}{\Gamma + k_{nr}} \tag{1.2}$$

An example absorption and PL spectrum for Si nanocrystals (NC) is given Figure 1.4 along with a c-Si PV spectral response [42, 43]. Si NCs have a broad absorption spectrum and a large Stokes shift, with a PL peak in the NIR. The Stokes shift is the energy difference between the absorption band and PL band maxima. The spectral response of Si PV is higher in the NIR due to reduced thermalization losses for wavelengths close to the semiconductor band gap. Red-shifting some of the incident solar spectrum before light reaches the PV cells can result in improved spectral response [39, 40].

Downshifting materials can be deployed directly on the solar cell face, or used for concentrating photovoltaics. The former downshifts higher energy photons and transmits lower energy photons to the solar cell. Shifting the wavelength of light to improve the high energy spectral response of solar cells was first demonstrated in 1979 by Hovel *et al.*, who applied fluorescent plastic sheets to Si, GaAlAs, and GaAs solar cells. Lopez-Delgado *et al.* applied CdSe/CdS core/shell nanocrystals on c-Si solar cells and saw an increase in power conversion efficiency from 12.0% to 13.5% [39]. More recently, He *et al.* deposited graded thin-films of europium-doped yttrium orthovanadate (YVO_4:Eu) and hollow silica

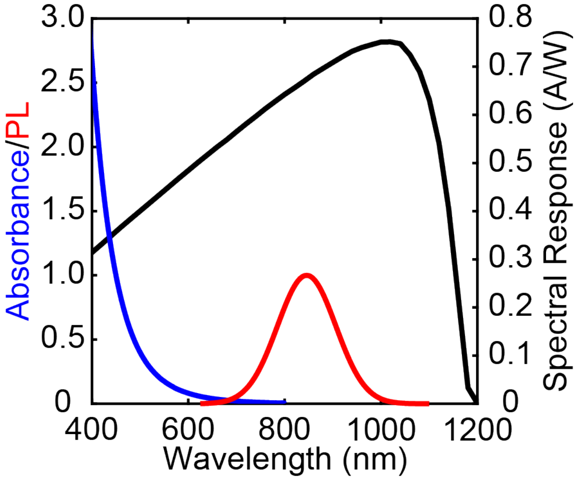

Figure 1.4: Normalized absorbance and PL spectrum of Si nanocrystals, and the spectral response of a c-Si photovoltaic cell [44].

nanoparticles on c-Si solar cells to create downshifting and antireflection films. The devices had an increase in efficiency from 14.39% to 14.98% [40].

1.3.2 Luminescent Solar Concentrator Efficiency Metrics

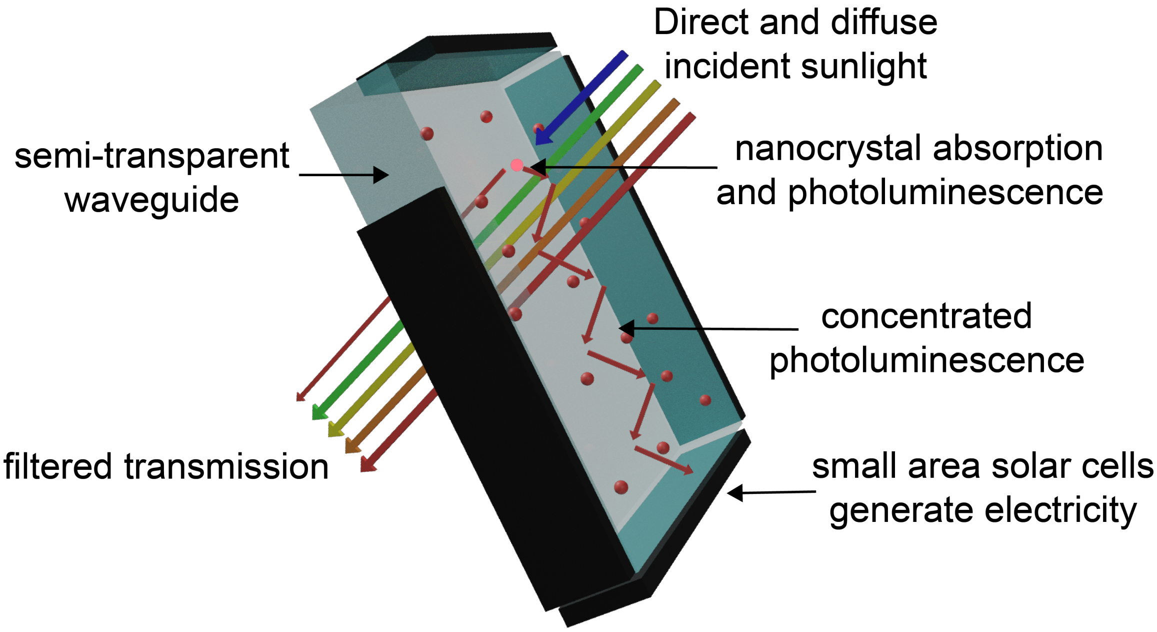

Figure 1.5: Illustration of the light harvesting process of a luminescent solar concentrator.

As introduced earlier, downshifting luminophores can also be applied to concentrating PV as LSCs. A schematic demonstrating the light harvesting mechanism of LSCs is given in Figure 1.5. A common metric to characterize the efficiency of an LSC is the optical efficiency, defined as:

$$\eta_{opt} = \Phi_1/\Phi_2 \tag{1.3}$$

where Φ_1 is the solar photon flux incident on the top surface of the waveguide and Φ_2 is the photon flux concentrated to the sides of the waveguide [45]. The optical efficiency is a meaningful metric because it is related to the power conversion efficiency of the PV cell mounted on the LSC via:

$$\eta_{LSC-PV} = \eta_{PV}\eta_{opt}q_{LSC} \tag{1.4}$$

η_{PV} is the power conversion efficiency of the PV cell, q_{LSC} is a spectral re-shaping factor, and η_{LSC-PV} is the power conversion efficiency of the LSC-PV system [46]. The spectral re-shaping factor accounts for the benefit from narrowing the spectrum incident on the PV cells to a more ideal spectrum for PV conversion. It is calculated using:

$$q_{LSC} = \langle Q_{PL}\rangle/\langle Q_s\rangle \tag{1.5}$$

where $\langle Q_{PL}\rangle$ and $\langle Q_s\rangle$ are the PV quantum efficiency averaged over the luminophore PL spectrum and the entire solar spectrum, respectively. $\langle Q_{PL}\rangle$ and $\langle Q_s\rangle$ are calculated using the following equations:

$$\langle Q_{PL}\rangle = \frac{\int_{250nm}^{2400nm} \eta_{EQE}(\lambda)PL(\lambda)\,d\lambda}{\int_{250nm}^{2400nm} PL(\lambda)\,d\lambda} \tag{1.6}$$

$$\langle Q_s\rangle = \frac{\int_{250nm}^{2400nm} \eta_{EQE}(\lambda)\Phi_s(\lambda)\,d\lambda}{\int_{250nm}^{2400nm} \Phi_s(\lambda)\,d\lambda} \tag{1.7}$$

1.3.3 Optical Loss Mechanisms

Another way to express the optical efficiency of LSCs is through the product of multiple efficiency terms that represent optical loss mechanisms.

$$\eta_{opt} = \eta_{PLQY}\eta_{abs}\eta_{wg}\eta_{trap} \tag{1.8}$$

In Equation 1.9, η_{abs} is the absorption efficiency, η_{wg} is the waveguide efficiency, and η_{trap} is the trapping efficiency. The absorption efficiency is described by the following equation:

$$\eta_{abs} = \frac{\int_{250nm}^{2400nm}(1 - R(\lambda) - e^{-\alpha_1(\lambda)*d})\Phi_s(\lambda)\,d\lambda}{\int_{250nm}^{2400nm}\Phi_s(\lambda)\,d\lambda} \tag{1.9}$$

α_1 is the absorption coefficient of the luminophores in the LSC, and *d* is the thickness of the LSC. After optical absorption, the electron/hole pairs undergo radiative recombination and emit downshifted light. The efficiency of the PL is described by η_{PLQY}. η_{trap} is the percentage of downshifted light that couples into total internal reflection modes in the waveguide. For luminophores that emit isotropically in a waveguide of index n=1.5, η_{trap} is 0.74. As photoluminescence propagates through the waveguide in total internal reflection modes, it can scatter, be absorbed by the matrix, or be reabsorbed by luminophores. These loss mechanisms decrease the η_{wg}, which is defined as how efficiently light coupled into total internal reflection modes reaches the solar cells.

1.3.4 Advantages and Research Challenges

The key advantage of using downshifting LSCs as light harvesting devices is their multifunctionality. Being semi-transparent, LSCs can be installed as windows or facades for building integrated photovoltaics [47]. For agrivoltaic applications like greenhouses, LSCs can generate electricity to offset energy demands while filtering the transmission to create an ideal spectrum for photosynthesis and crop production [48, 49]. Optimal design of LSCs for multifunctional optical performance, however, is challenging. Maintaining high

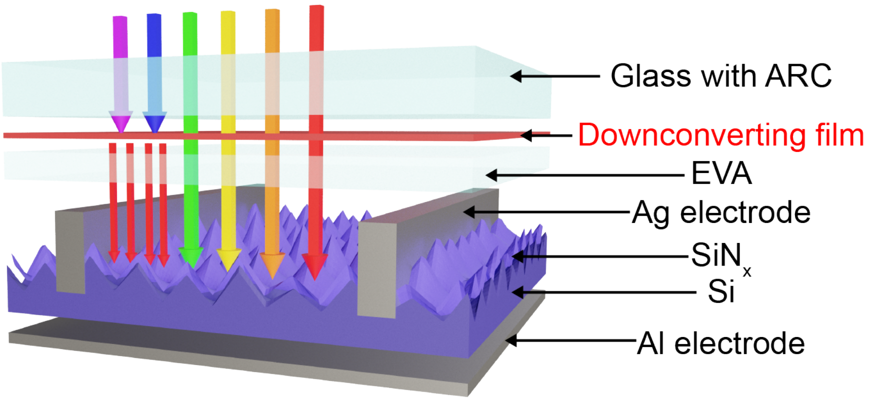

Figure 1.6: Schematic of a downconverting film on a Si PV cell. ARC is anti-reflection coating. EVA is ethylene-vinyl acetate.

waveguide efficiency and optical efficiency while designing tailored transmission properties requires extensive optical design and further research to be effectively implemented. Optical design of multifunctional LSCs is discussed in Chapters 2, 3, and 4 of this thesis.

1.4 Downconversion

The illustration in Figure 1.6 shows a simplified system of downconverting material on a solar cell. For every one high energy photon absorbed by the downconverting material, two low energy photons are emitted and can be absorbed by the solar cell. Previous theoretical studies demonstrated how downconversion applied to PV cells increase the maximum achievable conversion efficiencies. Trupke *et al.* presented limiting efficiency calculations using a detailed balance model of downconversion PV systems and determined the maximum conversion efficiency with the downconverter on the front surface of the solar cell was 38.6 % [7]. Badescu *et al.* built on Trupke's work by studying how various design parameters influenced the efficiency enhancement. It was determined the downconversion PV system was highly dependent on the solar cell and downconverter refractive index [8].

Experimentally, downconversion is achieved through doping or co-doping of trivalent lanthanide ions (Ln^{3+}) to activate host materials such as phosphors, glass, ceramics, and nanocrystals [50–52]. Ln^{3+} ions have ladder-like energy-level structures that achieve quantum cutting through resonant cross-relaxation processes or multistep cascade radiation transitions [51]. Recent work on Yb-doped CsPb($Cl_{1-x}Br_x$)$_3$, for example, had demonstrated high quantum yields of 195%, strong blue and UV absorption, and narrow PL around 1000 nm where the Si quantum efficiency is high [12, 13, 52–54]. The band edge is tunable from 400 to 500 nm by manipulating the chloride to bromide ratio, which provides more flexibility for optimization in photovoltaic systems [52, 55]. Previous detailed balance studies for this perovskite material predict that the downconversion can increase the power conversion efficiency for multicrystalline-Si, CIGS, and Si heterojunction solar cells by absolute percentages of 3.5%, 4.2% and 5.3% [55].

An important property controlling the photovoltaic efficiency enhancement from downconversion is the optical coupling efficiency ($\eta_{opt,DC}$), or how efficiently the downconverted light couples into the active layer of the solar cell to generate electricity [55]. In Figure 1.6, for example, the $\eta_{opt,DC}$ would be unity, but in a realistic system the downconverted light can escape the system before reaching the cell. The downconversion efficiency (η_{DC}) can then be described by equation 1.10. Detailed balance calculations estimated that increasing the downconversion efficiency from 100% to 200% enhances the PV device efficiency by a 7% absolute increase [55].

$$\eta_{DC} = \eta_{opt,DC}\eta_{PLQY} \tag{1.10}$$

Optical design of downconversion c-Si PV systems to achieve high optical coupling efficiency between the downconverting material and the Si cell remains an important challenge for this technology to reach its full potential. To be commercially competitive, downconverting materials should be integrated into state of the art high efficiency Si cells like PERC, Si heterojunction (SHJ), and tunnel oxide passivated contact (TOPCon) cells. Strategic integration into these optimized architectures to achieve enhanced efficiencies without inducing significant reflection or parasitic absorption requires careful optical design and is discussed in depth in Chapter 5.

1.5 Tandem Solar Cells

Tandems solar cells are another technology to enhance efficiency beyond single-junction limits through more efficient use of blue and UV sunlight. Figure 1.7 shows schematics of example tandem solar cells. In this case, the top band gap sub-cell absorbs visible light and transmits NIR light to the bottom sub-cell. The top sub-cell more efficiently utilizes the visible spectrum, which can increase the overall efficiency of the device.

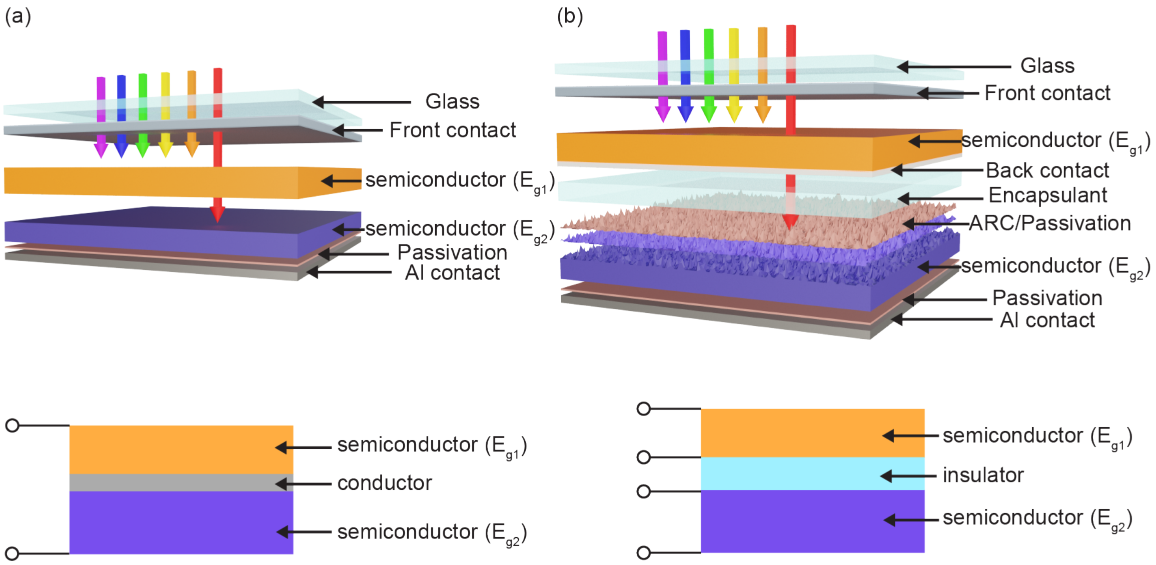

Figure 1.7: 3-dimensional and simplified 2-dimensional illustrations of a (a) two-terminal and a (b) four-terminal tandem solar cell. E_{g1} and E_{g1} represent wide and narrow band gaps.

The efficiency enhancement of tandem solar cells can be effectively described using the spectral efficiency ($\eta_{sp}(\lambda)$) as reported previously in literature [56–58]. η_{sp} for a single junction solar cell can be defined as:

$$\eta_{sp} = \frac{J_{SC}(\lambda)\, FF\, V_{OC}}{E_{e,\lambda}(\lambda)} \tag{1.11}$$

where $J_{SC}(\lambda)$ is the wavelength dependent short circuit current density and $E_{e,\lambda}(\lambda)$ is the solar spectral irradiance. $J_{SC}(\lambda)$ can be defined by Equation 1.12 [56].

$$J_{SC}(\lambda) = q\frac{\lambda}{hc}\eta_{EQE}E_{e,\lambda}(\lambda) \tag{1.12}$$

η_{EQE} is the external quantum efficiency, q is the elementary charge, h is Planck's constant, and c is the speed of light. To calculate the tandem efficiency η_T, the η_{sp} of two sub-cells can be integrated with respect to wavelength for each sub-cell [56]:

$$\eta_T = \frac{\int \eta_1(\lambda) f_1(\lambda) E_{e,\lambda}(\lambda)\, d\lambda}{\int E_{e,\lambda}(\lambda)\, d\lambda} + \frac{\int \eta_2(\lambda) f_2(\lambda) E_{e,\lambda}(\lambda)\, d\lambda}{\int E_{e,\lambda}(\lambda)\, d\lambda} \tag{1.13}$$

$f(\lambda)$ is the fraction of the incident photons that reach a sub-cell. At photon energies above their band gaps, if the top sub-cell has a higher $\eta_{sp}(\lambda)$ than the bottom sub-cell, then the η_T will be greater than the single-junction cells. The higher $\eta_{sp}(\lambda)$ for the top sub-cell can be achieved through greater η_{EQE} at high photon energies, or through a higher V_{OC}, which is typically true for wider band gap solar cells [6].

A key design consideration with tandem solar cells is the number of terminals. The two most common configurations are two-terminal and four-terminal tandems. Two-terminal tandems have two contacts on the top and bottom of the cell and require the junctions to integrated monothically and electrically connected (Figure 1.7 a). Having only two contacts requires current matching of the two junctions and is challenging to fabricate, but requires less material four-terminal cells [1, 59]. Four-terminal tandems have two contacts for each junction, and the junctions are isolated by an insulating layer (Figure 1.7 b). This configuration does not require current matching, but it requires complex stringing in the PV module and is optically challenging [1, 60]. Intermediate three-terminal tandems are also possible with and without an insulating layer in a many different configurations [61].

Si is an obvious choice for the bottom junction of tandem solar cells, because it is efficient, inexpensive, abundant, and has an ideal band gap for the bottom junction of a tandem solar cell [1, 56, 62]. To determine the best choices for top sub-cells, Yu *et al.* performed limiting efficiency calculations as a function of top sub-cell band gap for four-terminal and two-terminal tandem solar cells using Si as the bottom sub-cell. For both terminal configurations, a band gap of 1.7 eV yields the maximum tandem efficiency limit. Importantly, the four-terminal configuration efficiency has less dependence on the top sub-cell band gap and stays within 5% of the maximum efficiency from a band gap of 1.4 eV to 2.1 eV. GaAs, CdTe, GaInP, and perovskites are within this ideal band gap range [56].

Experimentally, several of these top-cells have been paired with Si cells to create high efficiency tandem devices. III-V semiconductors like GaAs have reached 32.8% efficiency in a mechanically stacked configuration [17]. Perovskite/Si tandems are exciting as they can be fabricated at a lower cost and have efficiencies that have surpassed state of the art GaAs tandems [16, 17]. With the rapid advancement of perovskite PV, the perovskite/Si tandem performance is expected to continue to improve [1].

CdTe/Si is another promising pairing. The current efficiency of CdTe/Si technology is not competitive, but Tamboli *et al.* predicted efficiencies as high as 30% are possible [60]. CdTe cells are economically advantageous to pair with silicon as they can be manufactured at scale for a low-cost and have proven long-term stability. If CdTe/Si tandem solar cells can reach the predicted efficiencies, they would provide a stable and low-cost option with efficiencies competitive with other state of the art tandem devices [60].

As discussed previously, the four-terminal configuration holds numerous advantages [60]. The additional interfaces and transparent contacts in four-terminal devices make this configuration optically challenging, as the CdTe sub-cell must transmit sub-band gap light efficiently to the Si sub-cell. A thorough understanding of sub-band-gap transparency losses and optical design methods to improve transmission is required to advance the CdTe/Si tandem technology. Chapter 6 addresses this research challenge further.

1.6 Thesis Outline

This thesis begins by investigating methods to enhance the efficiency and multifunctional properties of LSCs. In Chapter 2, we investigate how the luminophore selection in a tandem configuration influences the absorption, waveguide efficiency, and aesthetic quality of LSCs. Using an analytical model to estimate LSC efficiency, we make connections between the luminophore optical properties, device performance, and aesthetic quality, and develop luminophore selection criteria that can be applied to other LSC devices. Chapter 3 studies a bilayer LSC designed for agrivoltaic applications. We demonstrate how combining two luminophores in a monolithic structure enhances absorption, efficiency, and transmission tunability. In depth analysis of the light propagation through the waveguide reveals how overlap between the absorption and PL spectra of narrow and wide band gap luminophores can induce inter-luminophore absorption sensitization and ultimately enhance efficiency. In Chapter 4, we explore a method to control the emission direction of LSCs to optimize their multifunctionality. A needle-insertion thin-film optimization method is implemented to create photoluminescent thin-film stacks that have preferential emission out on LSC face. Benefits of the unidirectional emission is also put into context for agrivoltaic applications.

The thesis continues with other methods to enhance the efficiency of photovoltaic cells. In Chapter 5, we discuss how the placement and method of incorporation of downconverting materials in a Si photovoltaic cell influences the short circuit current density and power conversion efficiency. Light coupling between the downconverting material and a solar cell with realistic module architecture is calculated for three different configurations, and efficiency enhancements are estimated. The optical losses are described in detail and design suggestions are given for downconversion PV cells. Chapter 6 investigates roughness induced CdTe transparency losses in a CdTe/Si tandem solar cells . Analysis of the electric field and power absorption data gives insight into how the surface roughness creates a near-field focusing effect that dominates absorption in the transparent back contact. The roughness and index contrast is tuned to identify methods to mitigate the optical losses. Optical design recommendations are given to enhance CdTe transmission and increase efficiency.

Lastly, Chapter 7 gives a summary of the research findings and important conclusions in the thesis. Outlook and recommendations toward future studies on LSCs, downconversion PV, and tandem solar cells are provided.

Chapter 2

Evaluating Tandem Luminescent Solar Concentrator Performance Based on Luminophore Selection

2.1 Introduction

The efficiency of LSC-PV systems is limited by the luminophore band gap, reabsorption, and the chosen PV cells [45]. Wide band gap luminophores have reduced thermalization losses but cannot utilize the lower energy sunlight. Narrow band gap luminophores have broad absorption spectra but suffer from higher thermalization losses. However, the band gap tunability of luminophores provides an opportunity to implement tandem LSCs with multiple luminophores to overcome these limitations. Tandem LSCs have the potential to simultaneously increase absorption and broaden the luminophore absorption spectrum relative to single junction LSCs, while decreasing thermalization losses analogously to multijunction PV cells. The higher band gap luminophore in the top junction absorbs higher energy incident sunlight to convert to electricity, and the lower band gap luminophore in the

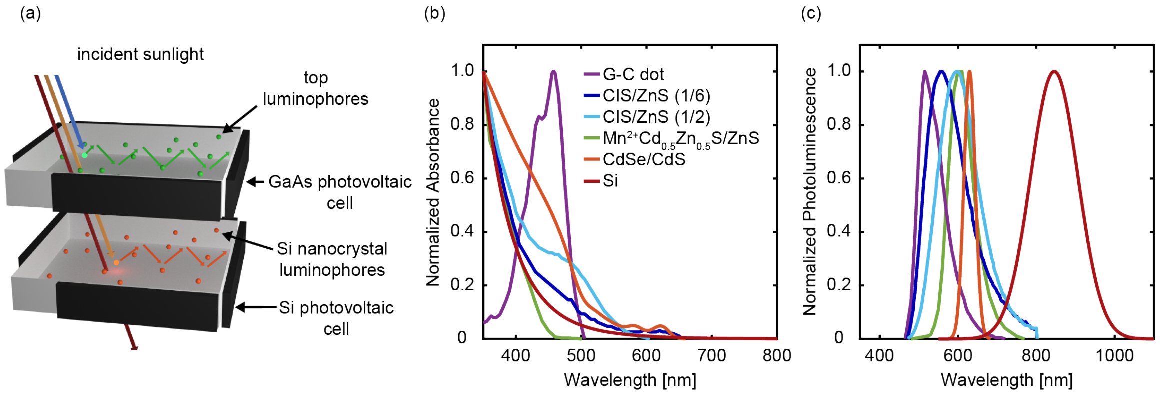

Figure 2.1: (a) Schematic of the tandem LSC with two different types of luminophores in separate waveguides coupled to GaAs and Si PV cells. Normalized (b) absorbance and (c) PL spectra of the different luminophores tested for the tandem LSC system. The absorption and PL spectra were sourced from literature [63, 67–70].

bottom junction absorbs and converts the lower energy light transmitted by the top junction (Figure 2.1a). In this way, each section of the solar spectrum is utilized more efficiently. Previous studies have demonstrated higher power conversion efficiency for tandem LSCs compared to their single junction counterparts [63–66].

In this chapter, we explore candidate materials for tandem LSCs using Si nanocrystals (NCs) as low band gap luminophores for the more broadly absorbing bottom junction. Si NCs (assumed η_{PLQY}=0.5 in this chapter) are non-toxic, earth abundant, and exhibit exceptionally low overlap between their absorption and PL spectra, a necessary property for high efficiency LSCs. These NCs have been successfully embedded into polymer matrices with reduced scattering for implementation as scalable LSC waveguides [42, 71]. With a PL spectrum in the NIR, the downshifted light from Si NCs is well suited for photovoltaic conversion by a Si PV cell coupled to the LSC waveguide.

There are multiple higher band gap luminophores that could be a suitable choice for the top junction namely CdSe/CdS NCs, $Mn^{2+}Cd_{0.5}Zn_{0.5}S/ZnS$ NCs, Carbon dots (C-dots), and $CuInS_2$ (CIS/ZnS) NCs [63, 67–70]. All these luminophores have been used previously to create high efficiency LSCs with high η_{PLQY} and exhibit low overlap between the absorption and PL spectra. The purpose of this study is to determine if Si NCs can be used in a tandem LSC system, and which higher band gap luminophores would be most suitable for the top junction. More broadly, this study aims to connect luminophore optical properties with both photovoltaic efficiency and aesthetic quality to develop luminophore selection criteria for tandem LSC systems.

2.2 Methods

2.2.1 Analytical Modeling

The system of interest is illustrated in Figure 2.1a with the top luminophores and Si NCs incorporated in two separate, stacked waveguides as nanocomposite films on glass. Thin-film GaAs PV cells are used for the top junction, and multicrystalline Si (mc-Si) PV cells were used for the bottom. The properties for these were sourced from literature [72, 73]. The absorbance and PL spectra for $Mn^{2+}Cd_{0.5}Zn_{0.5}S/ZnS$ (η_{PLQY}=0.78) [63], CIS/ZnS (1/6) (η_{PLQY}=0.44) [67], CIS/ZnS (η_{PLQY}=0.81) [67], green C-dots (G-C dots)(η_{PLQY}=0.5) [68], and 7.5 monolayer (ML) shell CdSe/CdS (η_{PLQY}=0.75) [70] are shown in Figure 2.1b and c. The notation (1/6) and (1/2) represent the stoichiometric ratios of Cu to In.

The optical efficiencies of the LSCs were modeled analytically using a model previously shown to accurately predict LSC efficiency [45]. Briefly, the optical efficiency (η_{opt}) is assumed to be the product of the absorption efficiency (η_{abs}) and the collection efficiency (η_{col}). η_{abs} is calculated by integrating the wavelength dependent absorption weighted by the AM1.5G spectrum, and accounting for a 4% loss from reflection off the waveguide at normal incidence. The filtered transmission from the top junction is also taken into account when calculating η_{abs} for the bottom junction. We calculate η_{col} using:

$$\eta_{col} = \eta_{wg}\eta_{PLQY}\eta_{trap}[1 - \eta_{PLQY}\eta_{trap}(1 - \eta_{wg})]^{-1} \tag{2.1}$$

The waveguide efficiency in the absence of reemission was adapted from previous models, such that

$$\eta_{wg} = \gamma_2 + \gamma_1/(1 + \beta\alpha_2 L) \tag{2.2}$$

where α_2 is the reabsorption coefficient, β is a fitting parameter, *L* is the waveguide side length (which for this study was held constant at 0.5 m), and γ_2, γ_1 are correction factors to account for wavelength dependent reabsorption defined as

$$\gamma_1 = \int_{350nm}^{\lambda*} PL(\lambda)\, d\lambda / \int_{350nm}^{1100nm} PL(\lambda)\, d\lambda \tag{2.3}$$

and

$$\gamma_1 = \int_{\lambda*}^{1100nm} PL(\lambda)\, d\lambda / \int_{350nm}^{1100nm} PL(\lambda)\, d\lambda \tag{2.4}$$

.

γ* is the wavelength where the absorbance approximately drops to zero.

2.2.2 Monte Carlo Ray-Tracing Simulations

The accuracy of the analytical model was checked by comparing to Monte Carlo ray tracing results, as seen in Figure 2.2a. In both the analytical and Monte Carlo ray tracing models, the power conversion efficiency of the LSC-PV system was calculated using Equation 1.4. Monte Carlo ray-tracing simulations are an accurate and versatile way to model the efficiency of luminescent solar concentrators [70, 74]. The ray-tracing simulations injected millions of photons across the solar spectrum into a 3-dimensional LSC waveguide and tracked the photon position, photon wavelength, and refractive index of the material. All photon interactions like absorption, emission and reflection were determined randomly, weighted by a probability distribution. The luminophore absorption probability for each move step was determined using:

$$P_{abs} = 1 - 10^{-OD(\lambda) l_{step}/d} \tag{2.5}$$

where OD(λ) is the optical density of the LSC, and l_{step} is the optical path length. All reflections and refraction properties were determined by using Snell's law and Fresnel equations. Photons were considered collected if they are incident on one of the four sides of the waveguide, which is where the PV cells would be mounted to the waveguide. To calculate the optical efficiency from the ray-tracing simulations the following equation was used:

$$\eta_{opt} = \frac{\int \phi(\lambda)\Phi_s \, d\lambda}{\int \Phi_s \, d\lambda} \tag{2.6}$$

where $\phi(\lambda)$ is the fraction of photons collected calculated directly from the ray-tracing simulation results. The collection efficiency was calculated according to:

2.3 Results and Discussion

2.3.1 LSC-PV Efficiency at Constant Absorption Efficiency

The first goal of this study was to determine which top luminophores result in the largest efficiency enhancement relative to the single junction Si NC based LSC, while maintaining the aesthetic quality. These calculations also attempt to identify if the top luminophore increases the waveguide efficiency of the tandem LSC system when splitting the incident spectrum, or if the only effect is broadening absorption. Understanding the origin of the efficiency enhancement for tandem LSCs is important is establishing luminophore selection criteria. Using the analytical model described above, the power conversion efficiency and light utilization efficiency were estimated at constant luminophore absorption efficiency (η_{abs}) by changing the fraction that the top and bottom junction luminophores absorb. The absorption fraction was controlled by scaling the luminophore absorbance in the top and bottom junctions simultaneously to change the contribution each luminophore makes to the absorption. The results are shown in Figure 2.2 for absorption efficiencies of 10% and 16% when integrated from 350 nm to 800 nm, where each color represents a different top luminophore. In this case, changing the absorption fraction is not changing the overall absorption efficiency of the system, just the amount absorbed by each luminophore.

Every top junction luminophore except for the CIS/ZnS (1/6) increased the power converion efficiency compared to the case with all Si (decreasing Si absorption fraction) for both absorption efficiencies tested. The increase in power conversion efficiency indicates that for those luminophores there is an efficiency benefit from splitting the spectrum, and that light absorption by the top junction would be converted to electricity more efficiently than the bottom junction. As expected, the 16% absorption efficiency results had higher power conversion efficiency and light utilization efficiency than the 10% absorption efficiency. The differences in absorption efficiencies did not change which luminophores had higher or lower efficiencies. It is important to emphasize that these results do not imply that the highest efficiency is realized with a Si absorption fraction of 0. Including the Si NCs in the bottom junction is necessary because it increases overall absorption and broadens the

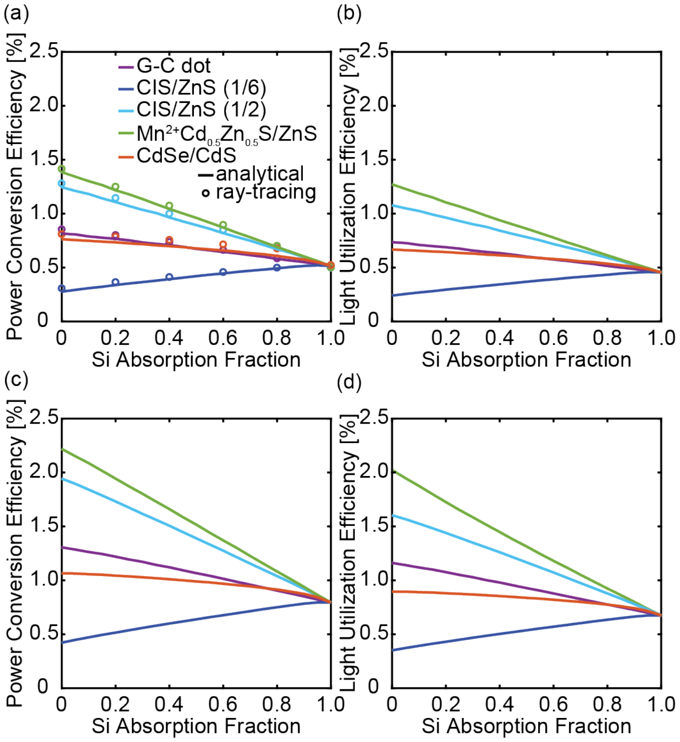

Figure 2.2: Estimated power conversion efficiency and light utilization efficiency for the tandem LSC for constant overall absorption efficiency of (a),(b) 10% and (c),(d) 16%. Si absorption fraction refers to the fraction of light absorbed by the Si nanocrystals out of all light absorbed by the luminophores. The markers in (a) are from Monte Carlo ray tracing simulations.

spectral coverage of the system. Since these calculations intentionally held the absorption efficiency constant, that benefit is not included in this figure.

The luminophores with the highest power conversion efficiency, $Mn^{2+}Cd_{0.5}Zn_{0.5}S/ZnS$ and CIS/ZnS (1/2), performed the best because of their high η_{PLQY} and low overlap between the absorption and PL spectra, resulting in high collection efficiencies. It is notable that the $Mn^{2+}Cd_{0.5}Zn_{0.5}S/ZnS$ and CIS/ZnS (1/2) NCs have comparatively high and low band gaps, respectively, and for these calculations there was no discernible trend between luminophore band gap and the efficiency. The efficiency for the LSC with the G C-dots was not as high because the η_{PLQY} was lower at 0.5, and the CdSe/CdS NCs had more significant reabsorption losses than the $Mn^{2+}Cd_{0.5}Zn_{0.5}S/ZnS$ and CIS/ZnS (1/2) NCs. The LSC with CIS/ZnS (1/6) NCs was the only system tested that had a decrease in the power conversion efficiency with decreasing Si absorption fraction. In this case, the light that is absorbed would be converted to electricity less efficiently than a single junction LSC of Si NCs, and the overall collection efficiency for the tandem LSC is lower.

2.3.2 LSC Aesthetic Quality

The light utilization efficiency is the product of the power conversion efficiency and the visible transmittance (*VT*), and it is useful parameter for semi-transparent solar harvesting devices to evaluate photovoltaic efficiency and aesthetic quality simultaneously [75]. In this case, LSCs with good aesthetic quality have minimal color shift and high visible transmittance. To have a high light utilization efficiency, the device must balance high efficiency with high transmission of visible light. The visible transmittance is calculated using:

$$VT = \frac{\int T(\lambda) * E_{e,\lambda}(\lambda) * V(\lambda)\, d\lambda}{\int E_{e,\lambda}(\lambda) * V(\lambda)\, d\lambda} \tag{2.7}$$

Equation 2.7 is integrated across the visible where *T* is the LSC transmission, $E_{e,\lambda}$ is the solar spectral irradiance, and *V* is the photopic response of the human eye. The light utilization efficiency followed similar trends to the power conversion efficiency (Figure 2.2b and d), but decreased slightly as the visible transmittance was not unity for any LSC and did not change significantly when adjusting the Si absorption fraction. $Mn^{2+}Cd_{0.5}Zn_{0.5}S/ZnS$ and the G C-dots have higher band gaps and their absorption spectra do not span as much of the visible spectrum as the other luminophores, therefore the resulting visible transmittance was higher than the other luminophores at lower Si absorption fraction. The differences in power conversion efficiency played a more dominant role, however, so the higher visible transmittance for these luminophores did not influence the overall trends significantly.

To further evaluate the aesthetic quality, the chromaticity coordinates of the light transmitted through the LSC were calculated and plotted in Figure 2.3 using the same absorption parameters that were used in Figure 2.2c-d. The chromaticity coordinates characterize the color of the transmitted light through the LSC. A significant change in the chromaticity coordinates corresponds to a distortion in color of the transmitted light. A black dot is included that represents the color of the incident light before interacting with the LSC. The point where the data converges on the same point on the chromaticity plot represents a Si absorption fraction of 1, and no light is being absorbed by the top luminophores. As the Si absorption fraction decreases to 0, the chromaticity coordinates of the transmitted light shift, as well. The majority of the luminophores tested did not significantly shift the color

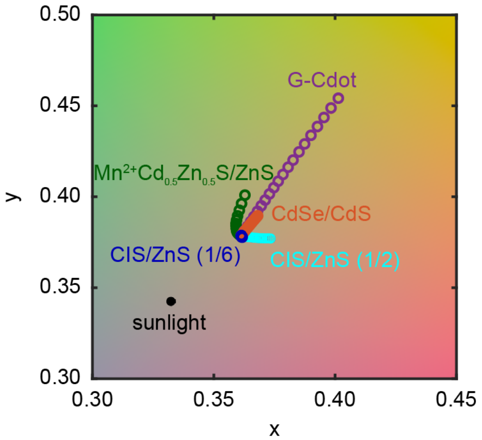

Figure 2.3: Chromaticity coordinates of the light transmitted through the tandem LSC for different top luminophores while changing the Si absorption fraction.

compared to a single junction Si NC LSC, but the G C-dots shifted the color dramatically. As the absorption fraction of the G-C dots increased, the chromaticity coordinates shifted away from the blue corner of the chromaticity diagram. The stronger color shift can be attributed to the absorption spectrum of the G-C dots, which begin strongly absorbing at approximately 500 nm. This demonstrates the aesthetic benefit of luminophores that either absorb completely outside the visible spectrum or absorb relatively uniformly across most of the visible spectrum. It should also be noted that none of the top luminophores shifted the color to be more similar to sunlight, so none of the top luminophores improved the color of the transmitted light.

2.3.3 Influence of LSC Top Luminophore Band Gap

Another set of calculations were performed to further understand the influence that the top luminophore band gap has on the efficiency of the tandem LSC system. In Figure 2.4 the power conversion efficiency and light utilization efficiency are shown as the optical density of each candidate top luminophore increases. The optical density of the Si NCs at 350 nm was held constant at 0.8. As the optical density of the top luminophore increases, the overall absorption efficiency of the LSC also increases, therefore this does not have constant absorption efficiency like the data in Figure 2.2.

The power conversion efficiency increased for every luminophore as the optical density increased, with the most dramatic increase observed for CIS/ZnS (1/2). The high efficiency when using the CIS/ZnS (1/2) NCs arises from a combination of high η_{PLQY}, low overlap between the absorption and PL spectra, and a luminophore band gap closer to the GaAs PV cell band gap. When the band gap of the luminophore is matched to the band gap of the PV cell, an increase in the peak optical density leads to a stronger increase in overall absorption efficiency. This explains why $Mn^{2+}Cd_{0.5}Zn_{0.5}S/ZnS$, which resulted in one of the higher efficiencies for the constant absorption calculations, did not result in the most efficient system in this case. Since the higher luminophore band gap is further away from the band gap of the GaAs PV cell, $Mn^{2+}Cd_{0.5}Zn_{0.5}S/ZnS$ exhibits a reduced increase in absorption efficiency with increasing peak optical density. There are exceptions to this: the CdSe/CdS NCs had a similar band gap to the CIS/ZnS (1/2) NCs, but resulted in lower power conversion efficiency. This exception arose from the slightly higher overlap between the absorption and PL spectra of the CdSe/CdS luminophores.

The CIS/ZnS (1/6) case is interesting, as Figure 2.2 showed as the Si absorption fraction decreased, the power conversion efficiency decreased, but Figure 2.4 showed that the efficiency increased with increasing top optical density. This is a case where the increase in efficiency from the introduction of the top junction to the system arises only from the increase in absorption, and not from either enhanced collection efficiency or a reduction in

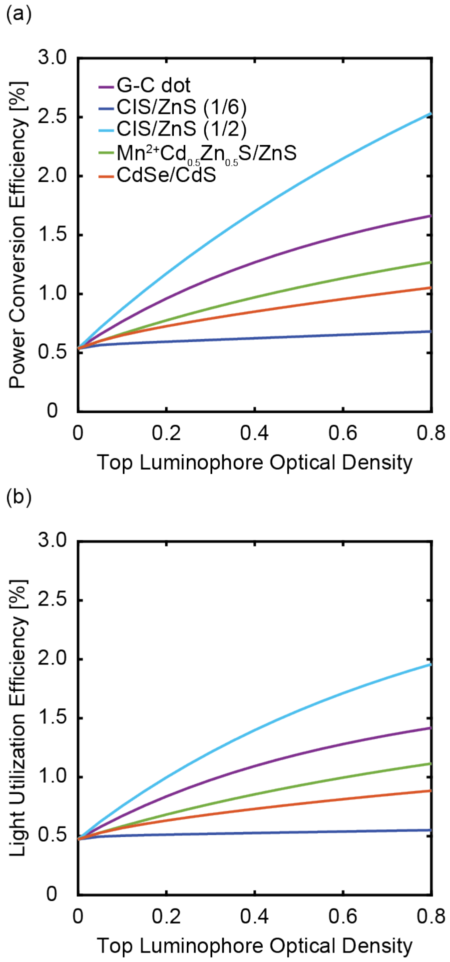

Figure 2.4: (a) Power conversion efficiency and (b) light utilization efficiency for the tandem LSC while increasing the peak optical density of the top luminophore.

thermalization losses from splitting the spectrum and concentrating some of the light on the higher band gap PV cell. These NCs can still be used to increase the efficiency of the tandem LSC system, but it is important to understand that benefit arises only from enhanced absorption.

The light utilization efficiency exhibited a similar trend to the power conversion efficiency, with all the efficiencies reduced slightly from the non-unity visible transmittance. It should be noted that the luminophores with lower band gaps and more spectral coverage across the visible spectrum, such as the CIS/ZnS and CdSe/CdS NCs, had proportionally lower light utilization when compared to the power conversion efficiency results. In this case, however, this effect was not dominant enough to significantly shift the overall trend in the data.

2.4 Conclusions

This study analytically modeled combinations of luminophores for tandem LSCs, with Si NCs on the bottom junction. These results confirm that Si NCs can be used in tandem LSC configurations to increase the system efficiency while maintaining good aesthetic quality. This study also highlights the importance of luminophore selection, as the CIS/ZnS (1/6) NCs led to reduced collection efficiencies. In this system, $Mn^{2+}Cd_{0.5}Zn_{0.5}S/ZnS$ and CIS/ZnS (1/2) are the best candidates for the top junction due to their high η_{PLQY}, spectral compatibility with the GaAs solar cell, and aesthetic characteristics.

Understanding how luminophore selection influences the efficiency and aesthetics of tandem LSC systems assists in the strategic design of LSCs as effective light harvesting devices. The aim of this chapter is not only to determine which luminophores perform best when paired with the Si NCs, but to work toward developing broader criteria for luminophore selection in tandem LSC systems based on how the luminophores interact with each other and the chosen PV cells. The results highlight the importance of identifying whether the top luminophore enhances the collection efficiency, absorption efficiency, or reduces the thermalization losses. Matching the luminophore band gap to just above the PV cell band gap can lead to a greater efficiency enhancement. Aesthetically, the color shifting can be reduced by choosing luminophores that either absorb uniformly across the visible spectrum, or completely outside of the visible spectrum.

Chapter 3

Bilayer Luminescent Solar Concentrators with Enhanced Absorption and Efficiency for Agrivoltaic Applications

3.1 Introduction

In the previous chapter, different luminophores were tested as top junctions in a tandem LSC to determine luminophore selection criteria that optimizes both photovoltaic efficiency and aesthetic quality. In this chapter, we investigate an LSC system tailored for agrivoltaic applications, a bilayer LSC. We created bilayer LSCs consisting of two different luminophores to tune the transmission while also improving light collection for electricity generation. The first layer is based on Si nanocrystal (NC) quantum dots, which have received attention recently for use as LSC luminophores due to their desirable optical properties [42, 71, 76]. To achieve high absorption efficiency with an LSC composed of Si NCs, however, the NC-polymer nanocomposite films must be relatively thick and contain a high concentration of NCs. There is an upper limit to the NC concentration before significant nanocrystal agglomeration occurs, which dramatically increases scattering and reduces LSC optical efficiency [42, 71].

An alternative strategy is to make a bilayer system of two different luminophores. This second luminophore could either act as the LSC luminophore on its own, broadening the absorption spectrum and emitting over a different spectral range, or, if the second luminophore emits across a spectral range that Si NCs absorb, it can sensitize Si absorption. This type of device is fundamentally different from both tandem LSCs and dual band LSCs [63, 65, 68], as the luminophores are not separated by a low index layer, and the PL from each luminophore is coupled into the same waveguide and directed onto the same PV cell. The low index air gap between waveguides in tandem architectures induces more reflection from the additional air-glass interfaces, which reduces absorption efficiency of the second junction and reduces overall LSC transmission. For the agrivoltaic applications, the bilayer system is advantageous as it allows for the concentrations and thicknesses of each luminophore to be tuned individually, enabling greater tunability over the transmission spectrum. By putting the nanocrystals in different polymer layers, the concentration and chemical functionality can be optimized for each luminophore rather than compromising to make a blended system. Furthermore, the bilayer system simplifies the manufacturing and installation process significantly, as a single coating with one PV cell would be less expensive to install onto glass than multiple waveguides each with their own solar cell.

Here we use CdSe/CdS core/shell quantum dots as the second luminophore, since the band gap of these luminophores can be tuned across the visible spectrum, and these nanocrystals exhibit high photoluminescence quantum yields (η_{PLQY}) due to the passivating CdS shell [77]. We have previously shown that CdSe/CdS NCs can be dispersed well into a matrix of poly(cyclohexylethylene) (PCHE), creating high quality nanocomposite thin films for LSCs [70]. This combination of material systems allows for facile fabrication of bilayers, since PCHE and PMMA are dispersed in orthogonal solvents. This chapter uses a combination of experimental and computational methods to evaluate the absorption, light propagation, and efficiency of these bilayer devices. We also evaluate how tuning the optical density of each film influences the chlorophyll band transmission for potential use in agrivoltaic applications.

3.2 Advantages of LSCs for Agrivoltaics

The commercial greenhouse market is expected to expand over the next several years, offering high-yield agriculture and reduced water consumption for expanding populations. However, commercial greenhouses also have significant power needs for precision climate control, lighting, sensing, and other control mechanisms, highlighting the need for onsite power generation under a variety of weather conditions [78–80]. The LSC is an ideal greenhouse window architecture. The semitransparent nature of LSC-PV systems enables integration in a variety of environments where partial transparency provides either additional functionality or aesthetic benefits. For agrivoltaic applications specifically, the LSC additionally filters light transmission for enhanced crop growth [48, 49].

Several studies have demonstrated plant sensitivity to different illumination conditions and have obtained beneficial results from manipulating the relative intensity from different wavelength ranges incident on the crops [49, 81–84]. For example, one study grew red romaine lettuce under different combinations of LED light sources and found a combination of a RGB (R = 635 nm, G = 520 nm, B = 460 nm) light, and a far red (745 nm) light yielded the best leaf expansion and shoot biomass [82]. Other studies have shown that at higher blue light percentages of the total incident spectrum there is a decrease in growth and dry mass for various plant species [83, 84]. Recently, $CuInS_2/ZnS$ quantum dot films were used to modify the spectral quality of transmitted light incident on red romaine lettuce, and the plants had increased edible dry and fresh mass [49]. These studies indicate that electricity generation solutions that decrease the transmission of blue light and increase transmission of red light, as in the LSC which absorbs blue sunlight and shifts emission to longer wavelengths, are particularly promising routes to cogenerating electricity and crop production. However, to deeply understand the effects of the filtered spectrum on the germination and development of different crop species, LSCs with tailored and tunable transmission spectra are needed.

3.3 Methods

3.3.1 Photoluminescence Quantum Yield Measurements

Photoluminescence quantum yield measurements were preformed by using a 2 in. integrating sphere coupled to an OceanOptics USB2000 spectrometer calibrated by using an OceanOptics HL-3 Plus lamp. A 395 nm LED emitted radiation into an integrating sphere where the radiation became isotropic via diffuse reflection at the sphere walls. The emission spectra of QDs were then integrated and divided by the integrated change in excitation signal to calculate the η_{PLQY}.

3.3.2 CdSe/CdS-PCHE Film Fabrication

CdSe/CdS NCs were synthesized according to the literature procedures [77, 85] and described previously elsewhere [70, 86]. The nanocrystals were imaged by using transmission electron microscopy (Figure 3.1a). The particle size distribution is seen in Figure 3.1b, and the average diameter after shelling is 8.2 nm. The CdSe/CdS-PCHE nanocomposite film fabrication followed previous methods [70]. Briefly, a 200 mg/mL solution of poly(cyclohexylethylene)/octane was created and stirred for 2 h. The polymer solution was filtered through alumina to remove reaction byproducts. 0.6 mL of the PCHE/octane solution, 260 µL of CdS/CdSe dispersed in octane, and 1.14 mL of octane were mixed.

This solution was spun on 2 in. x 2 in. borosilicate glass to create the single layer of CdSe/CdS-PCHE and on the Si-PMMA film to create the bilayer device by using a Laurell WS-650Mz-23NPPB spin coater. The solutions were spun with a spin speed of 2000 rpm for 20 s with 500 rpm/s acceleration and then 500 rpm for 40 s with -500 rpm/s acceleration.

3.3.3 Si-PMMA Film Fabrication

Yaling Liu synthesized the Si nanocrystals and embedded them in PMMA to fabricate the Si-PMMA films, so the methods are not discussed here. More information on the Si-PMMA fabrication is reported in previous literature [43].

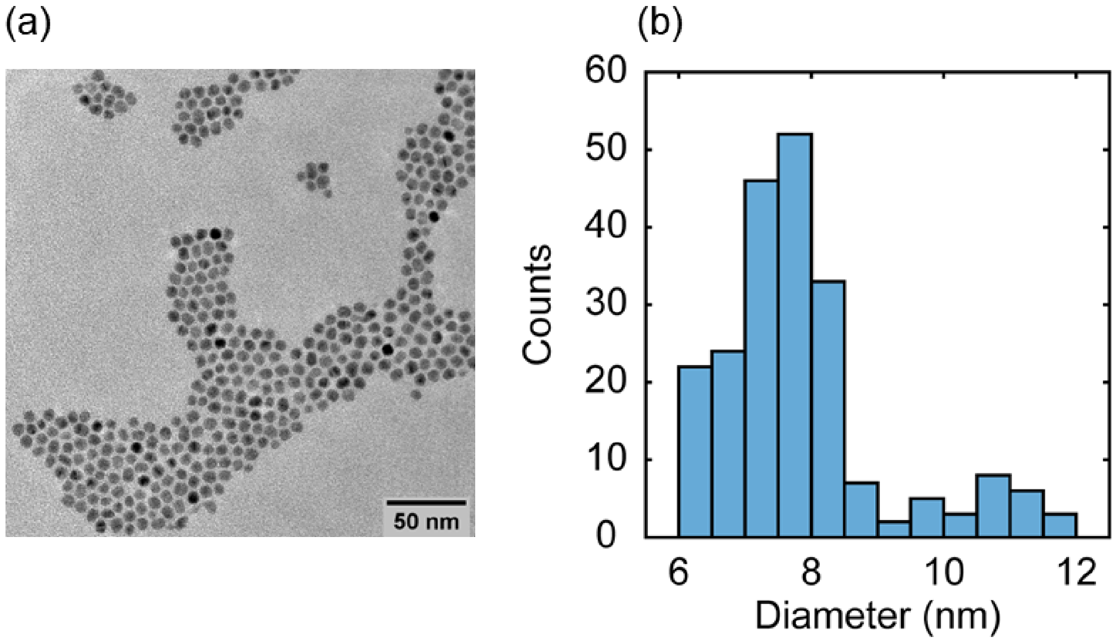

Figure 3.1: (a) Transmission electron micrograph of the CdSe/CdS nanocrystals. (b) Sizing histogram of CdSe/CdS nanocrystals measured using ImageJ from the transmission electron micrograph.

3.3.4 UV/Vis Spectrophotometry

Transmission measurements of the polymer-nanocrystal composite films were performed by using a Cary 7000 UV/vis spectrophotometer with a diffuse reflectance accessory. The total transmission measurement was performed by mounting the sample to the integrating sphere transmission port and blocking the back port with a PTFE standard. The PTFE standard was removed for the diffuse transmission measurements. Haze calculations were done according to ASTM D1003-00 [87]. For the total reflection, the sample is rotated by 3°20’ to couple all reflected light into the integrating sphere, and for diffuse reflection the sample is fixed.

3.3.5 Photoluminescence Attenuation Measurements

The composite films were mounted with the edge coupled to an integrating sphere input port. A 400 nm LED light source with a 0.5 mm spot size was positioned at normal incidence to the film’s top surface and scanned across the centerline of the sample directly

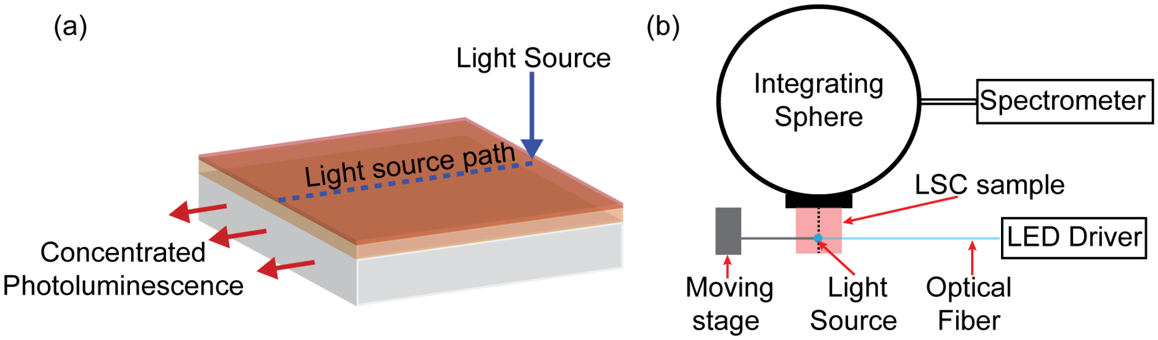

Figure 3.2: (a) Schematic of the (a) LSC samples and (b) optical setup during the photoluminescence attenuation measurements.

toward and away from the integrating sphere input port. An Ocean Insight Flame vis-NIR spectrometer was coupled to the integrating sphere to collect the concentrated PL that coupled into the integrating sphere at each excitation position. The spectrometer was calibrated to absolute irradiance by using an Ocean Optics HL-3 plus light source. A schematic of the optical setup is shown in Figure 3.2.

3.4 Results and Discussion

3.4.1 Optical Properties of Nanocomposite Films

The overall structure of the LSC studied here is depicted schematically in Figure 3.3a and consists of a glass substrate, followed by a Si NC-PMMA film and then by a film of CdSe/CdS-PCHE deposited on top of the Si-PMMA film. Details of the synthesis of CdSe/CdS nanocrystals are provided in Section 3.3, and details of the Si nanocrystal synthesis are provided elsewhere [43]. To form this structure, we deposited a Si NC-PMMA composite film with 1.5 Si wt % and a thickness of 83 µm on a 2 in. x 2 in. borosilicate glass slide using doctor blade deposition, following a procedure described elsewhere [42]. A film of 7.5 monolayer shell CdSe/CdS NCs dispersed in PCHE was spin-coated directly on the Si-PMMA. To measure the thickness, a separate control film of CdSe/CdS-PCHE was spin-coated on a Si substrate by using the same solution and parameters. The thickness of this control sample was measured at 324 nm by using spectroscopic ellipsometry. Additionally, the thickness of the bilayer reference film of PCHE on PMMA without nanocrystals was measured at 308 nm by using spectroscopic ellipsometry after roughening the backside of the glass substrate. The η_{PLQY} of both nanocrystal systems was measured both in solution and embedded in polymer. The as synthesized Si NCs in chloroform had a η_{PLQY} of 0.4 and a η_{PLQY} of 0.2 when embedded in PMMA in air. According to the previous study [71], the η_{PLQY} of Si NCs embedded in PMMA is approximately the same as in chloroform under oxygen-free conditions, while the η_{PLQY} of Si NCs decreases when exposed to air. Therefore, the decrease of Si NCs η_{PLQY} here can be avoided by fabricating the device in a nitrogen purged glovebox and deploying an encapsulant to isolate oxygen during use. The η_{PLQY} of the CdSe/CdS in octane was 0.73 and 0.58 when embedded in PCHE. An encapsulant could benefit the η_{PLQY} CdSe/CdS film as well, but the CdS shell passivates the surface of the CdSe and prevents significant decrease in the η_{PLQY} from exposure to oxygen. The decrease in measured η_{PLQY} from embedding the CdSe/CdS in PCHE could be from increased agglomeration and phase separation or from increased CdSe/CdS reabsorption when increasing the concentration compared to the NCs dispersed in octane [31, 88–92].

The two photographs in Figure3.3b visually indicate the PL from the bilayer device. The absorbance and PL spectra of the NCs are shown in Figure3.3c along with the molar extinction coefficients of chlorophyll *a* and *b* taken from the literature [93]. We note that the Soret bands of both chlorophyll *a* and *b* overlap significantly with the absorption bands of the nanocrystals, and the Q bands do not. However, the Q bands overlap (by different amounts) with the PL maximum of the CdSe/CdS NCs. Because some of the luminescent light absorbed and emitted by the CdSe/CdS will escape from the concentrator, this outcoupled light could be absorbed by crop species underneath the concentrator. The intensity of PL that would be outcoupled to the plants is lower than the intensity of the PL coupled into waveguide modes, but the additional light across the photosynthetic action spectrum of certain plant species could still promote plant growth, as observed in previous studies [49].

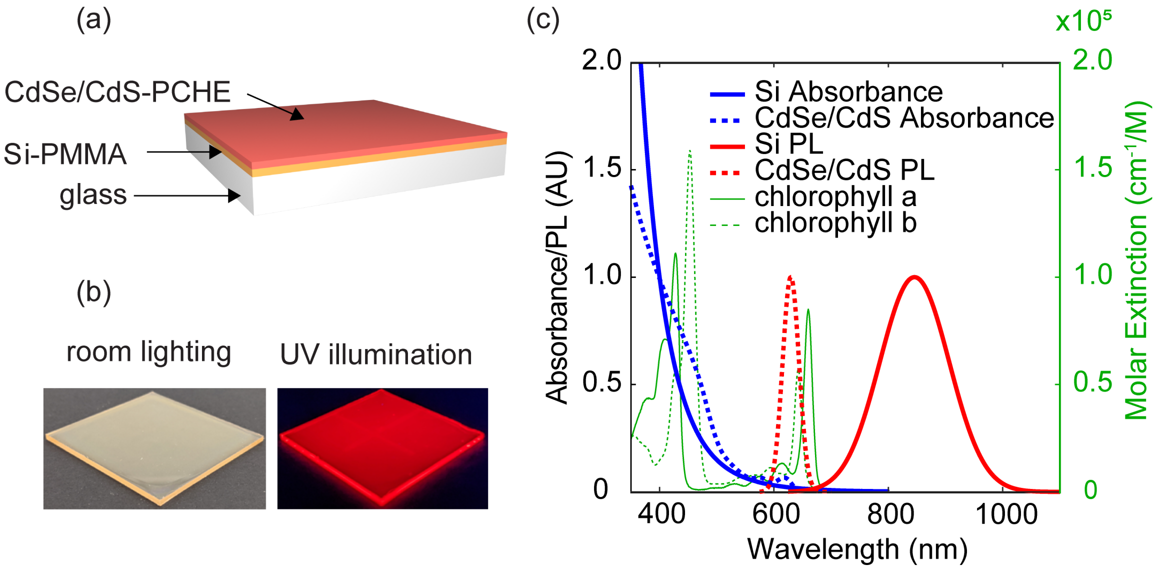

Figure 3.3: (a) Schematic of the bilayer device along with (b) two photographs of the bilayer device under room light and UV illumination. (c) Normalized absorbance and PL spectra of the Si and CdSe/CdS NCs and the molar extinction coefficient for chlorophyll a and b.

Tuning the exact size of the CdSe/CdS nanocrystals could allow for greater overlap with the Q bands of either chlorophyll *a* or *b*.

3.4.2 Spectral and Angular Properties of Bilayer LSC

To characterize the spectral and angular properties of the bilayer LSCs, we measured the total and diffuse transmission and reflection (Figure 3.4). Measurements were also performed on single layer CdSe/CdS-PCHE and Si-PMMA LSCs, the latter before CdSe/CdS-PCHE deposition, at the same concentrations and thicknesses as the bilayer LSC. Both the single layer CdSe/CdS-PCHE film and the single layer SiPMMA films showed decreases in total transmission (Figure 3.4a) compared to their respective undoped references, corresponding to an increase in absorption from the NC incorporation. When the CdSe/CdS-PCHE film was added to the Si-PMMA film to create the bilayer device, the total transmission decreased slightly. The total transmission results confirm that the nanocomposite films are absorbing as expected, with the CdSe/CdS-PCHE layer increasing the absorption slightly compared to the single layer of Si-PMMA. The total reflection (Figure 3.4b) for all samples containing a PCHE film or a film of CdSe/CdS-PCHE exhibit oscillations due

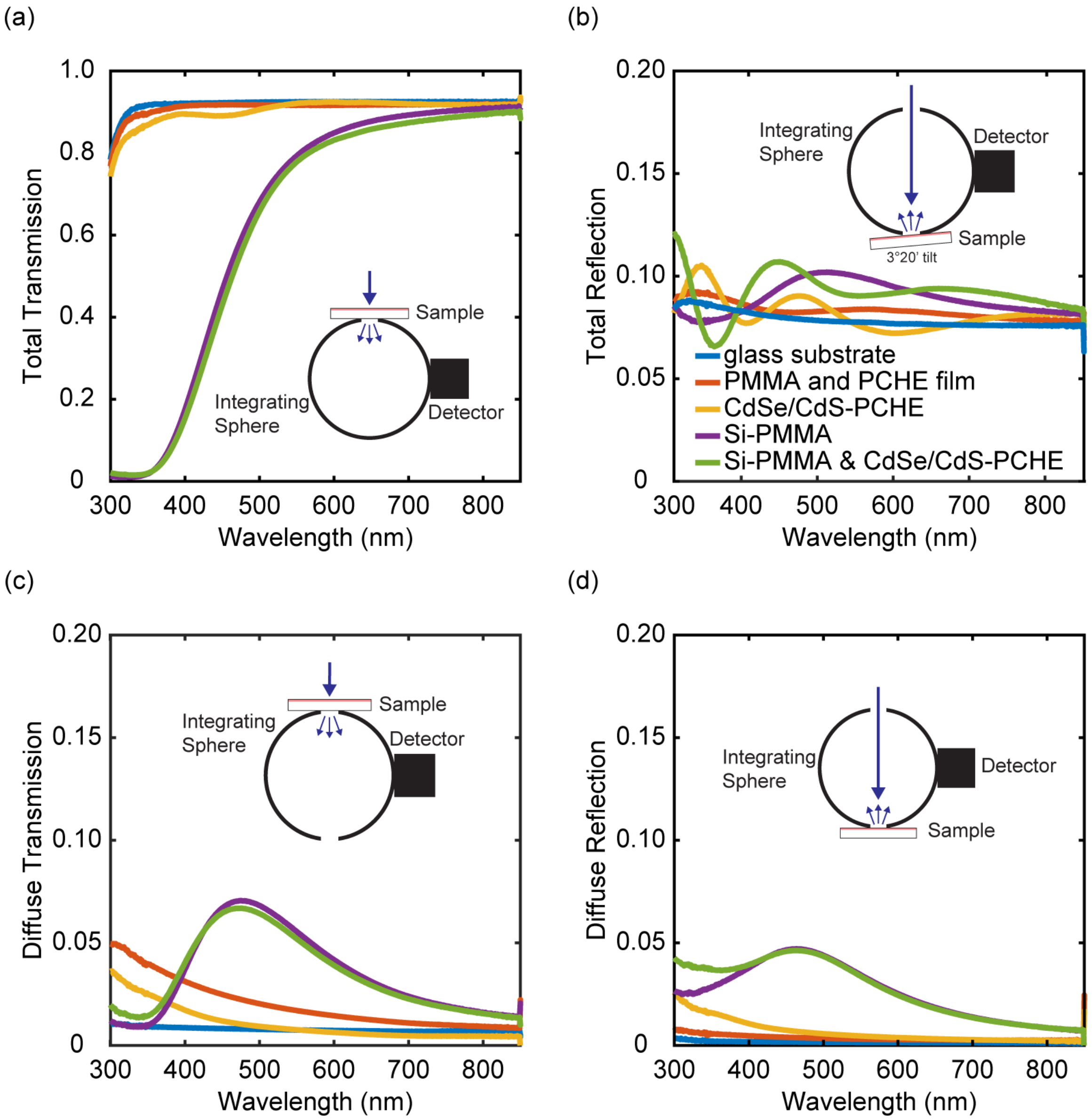

Figure 3.4: (a) Total transmission, (b) total reflection, (c) diffuse transmission, and (d) diffuse reflection for the CdSe/CdS-PCHE single layer film, Si-PMMA single layer film, and bilayer film. Measurements from an uncoated glass substrate and undoped PMMA and PCHE bilayer films are included for reference.

to thin film interference effects. The oscillations from CdSe/CdS-PCHE films have higher amplitudes due to the higher refractive index of the composite, which is consistent with previous results [70] and with the expected reflection from transfer matrix calculations for a PCHE film with and without embedded CdSe/CdS NCs. The increased total reflection seen for the single layer Si-PMMA film is from backscattered light.

The diffuse transmission (Figure 3.4c) remained relatively low upon addition of the NCs, which indicates minimal scattering in the nanocomposite films. The highest diffuse transmission occurred in the Si-PMMA film and the bilayer system, with a maximum at 480 nm. The diffuse transmission decreases at shorter wavelengths because of the strong increase in absorption, which prevents the transmission of scattered light. A similar trend is observed in the diffuse reflection measurements (Figure 3.4d). The measured haze for the bilayer film was 5.7%. On the basis of previous results where 83 μm thick Si-PMMA films had a haze exceeding 40% from nanocrystal agglomeration [42], we assume that the attenuation of light propagating through these films is dominated by absorption rather than scattering.

Films with high optical quality and low scattering are essential to achieve efficient electricity generation. Scattering from matrix defects or nanocrystal agglomeration will disrupt light propagation in total internal reflection modes and decrease waveguide efficiency. For agricultural applications, however, diffuse transmission penetrates deeper into a plant canopy, and applying diffusing materials in greenhouses has demonstrated increased plant production [94]. Balancing the nanocomposite optical quality for electricity generation and crop production is a key component for agrivoltaic LSCs.

3.4.3 Light Propagation and Waveguide Efficiency

To investigate the light propagation and waveguide efficiency of the LSCs, the PL at the edge of the concentrator was measured as a function of the position of the excitation light source. A 405 nm LED light source with a 0.5 mm spot size directed downward on top of the films was scanned across the samples in 1 mm steps, and an integrating sphere was coupled to one side of the waveguide to collect the concentrated PL at each excitation position. The collected intensity spectra for each distance were calibrated to absolute irradiance, and then the PL spectra at each position were fit to a Gaussian distribution. Further details are shown in Figure 3.2. The spectra with respect to the horizontal distance from the edge of

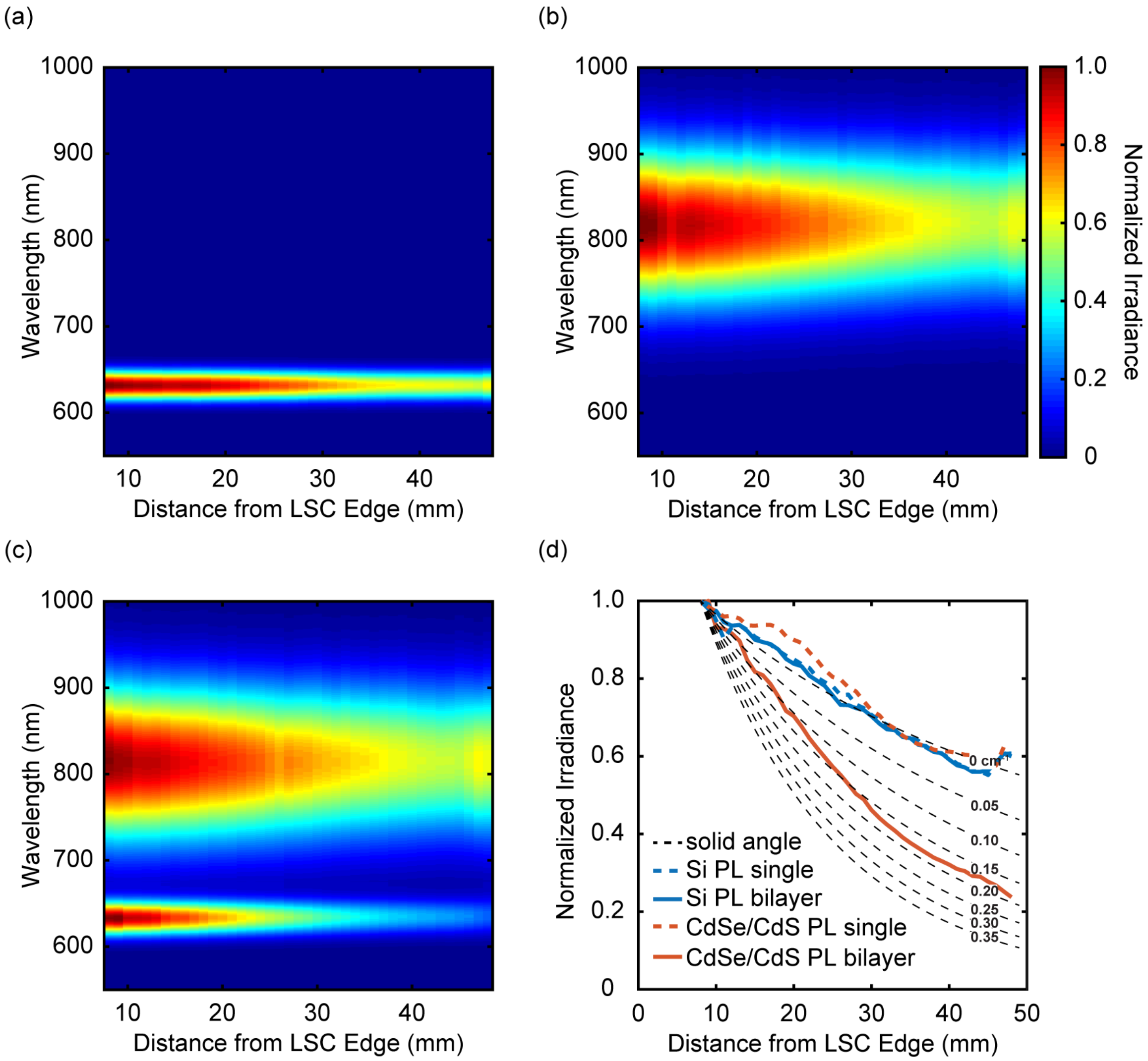

Figure 3.5: Wavelength and distance resolved normalized irradiance for the (a) CdSe/CdS-PCHE single layer, (b) Si-PMMA single layer, and (c) bilayer film. (d) Peak normalized irradiance for the different devices with analytically derived solid angle estimates for different attenuation coefficients. The normalization was performanced with respect to the PL spectrum of each luminophore.

the LSC to the light source are displayed in Figures 3.5a-c. In Figure 3.5c, normalization was performed with respect to each NC's own PL spectrum.

The CdSe/CdS nanocrystals emit in the visible, and the Si nanocrystals emit in the near-infrared (NIR), as is clearly seen in the single layer samples (Figures 3.5a,b). The normalized irradiance in these single layer samples decreases with increasing excitation distance to about 60% of the peak for both cases. The slight increase in irradiance at the end

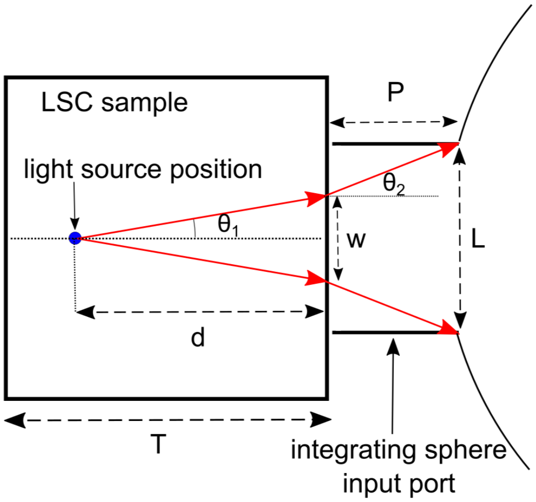

Figure 3.6: Geometry of the attenuation measurement for the solid angle calculation.

is real and due to reflection and scattering off the back edge of the LSC. When compared to the bilayer sample (Figure 3.5c), the Si PL looks nearly identical with the single layer case, but there is a noticeable increase in the CdSe/CdS attenuation in the bilayer sample.

The attenuation observed in these measurements is a combination of waveguide losses and the changing solid angle between the light source and the detector. To unravel these effects, Figure 3.5d shows the peak normalized irradiance as a function of light source distance from the LSC edge.

The reference lines are the analytically derived decrease in irradiance for different attenuation coefficients. The geometry of the sample and input port to the integrating sphere is described in Figure 3.6. The integrating sphere input port had a width (L) and depth (P) of 30 mm and 23 mm, and the sample length (T) was 50.8 inches. From the geometry, the following system of equations was solved for θ_1, θ_2, and w:

$$w = 2dtan(\theta_1) \tag{3.1}$$

$$w = -2Ptan(\theta_2) + L \tag{3.2}$$

$$\frac{sin(\theta_1)}{sin(\theta_2} = \frac{1}{n} \tag{3.3}$$

for *d* from 8 mm to 50.8 mm where *n* is the refractive index of the waveguide. The decrease in irradiance *I* was then calculated with the following equation and then normalized:

$$I = \frac{1}{2\pi} * 2\theta_1 * \gamma \tag{3.4}$$

Beer's law was applied to estimate the attenuation factor (γ) for each value of *d* as follows:

$$\gamma = exp(-1.144\alpha l) \tag{3.5}$$

where α is the attenuation coefficient and l*1.144 is the optical path length inside the LSC, and l is the average direct distance between the light source position and the edge of the waveguide. A factor of 1.144 was applied to account for the increased optical path length of light coupled in total internal reflection modes in a 3-dimensional waveguide slab [76].

By using the reference lines, we can graphically estimate the attenuation coefficient of the PL propagating through the waveguide. The Si NCs in both the single layer and the bilayer systems closely matched the solid angle reference line with an attenuation coefficient of 0 cm^{-1} . This means the Si NC PL coupled into total internal reflection modes did not significantly attenuate from reabsorption or scattering, and the waveguide efficiency is exceptionally high. The PL from the single layer of CdSe/CdS also corresponded to a near zero attenuation coefficient. However, the CdSe/CdS PL in the bilayer film showed increased attenuation, with an estimated attenuation coefficient of $\sim$0.17 cm^{-1}. The increased attenuation was expected and is due to the absorption of the CdSe/CdS NC PL by the Si NCs. Although the Si absorption is lower across the CdSe/CdS PL spectrum than it is at shorter wavelengths, the optical density of the Si-PMMA layer is $\sim$0.025 at normal incidence across the CdSe/CdS PL spectrum. The reabsorption of luminescence from the CdSe/CdS NCs by the Si NCs is greater than reabsorption by the CdSe/CdS NCs.

The results were also compared to Monte Carlo ray-tracing simulations for a system of similar LSC size and luminophore optical densities. The attenuation experiment was

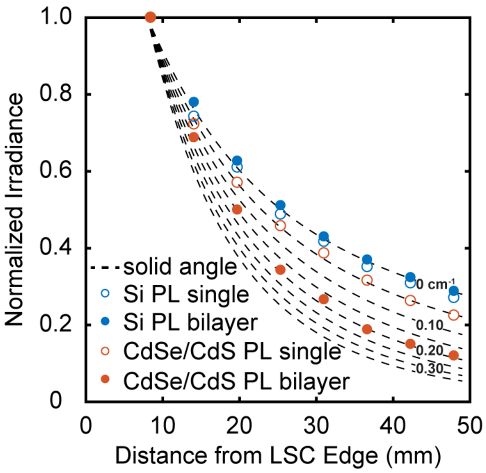

Figure 3.7: Simulated attenuation experiment using Monte Carlo ray-tracing for single layers of Si-PMMA and CdSe/CdS-PCHE and the bilayer. The solid angle estimates were done using θ_1*=arctan(L/2d).*

simulated by using ray-tracing on 2 in. × 2 in. waveguides for a Si-PMMA single layer, CdSe/CdS-PCHE single layer, and a bilayer device. The PLQY of the Si and CdSe/CdS NCs were set at 0.4 and 0.73, respectively, which is close to the experimental PLQY values of the NCs in solution. The resulting attenuation coefficients estimated from the ray-tracing for both single layers and the Si PL in the bilayer device were close to zero (Figure 3.7). The simulations on the CdSe/CdS PL predicted an increase in attenuation in the bilayer device similar to the experimental results, corresponding to an attenuation coefficient of $\sim$0.19 cm^{-1}. The higher attenuation coefficient is close to the estimated attenuation coefficient from the experimental results, $\sim$0.17 cm^{-1} , and is also due to the absorption of the CdSe/CdS NC PL by the Si NCs.

3.4.4 Efficiency Estimates for Scaled Devices

Given the agreement between experiment and simulation at the smaller scale, we used Monte Carlo simulations to determine whether the addition of the CdSe/CdS layer enhances the performance of the Si-PMMA LSCs for larger area (60 cm × 60 cm) devices (Figure 3.8). To simulate a strongly absorbing Si-PMMA film with a weaker absorbing CdSe/CdS-PCHE film, the optical density at 350 nm wavelength of incident radiation for the 40 μm

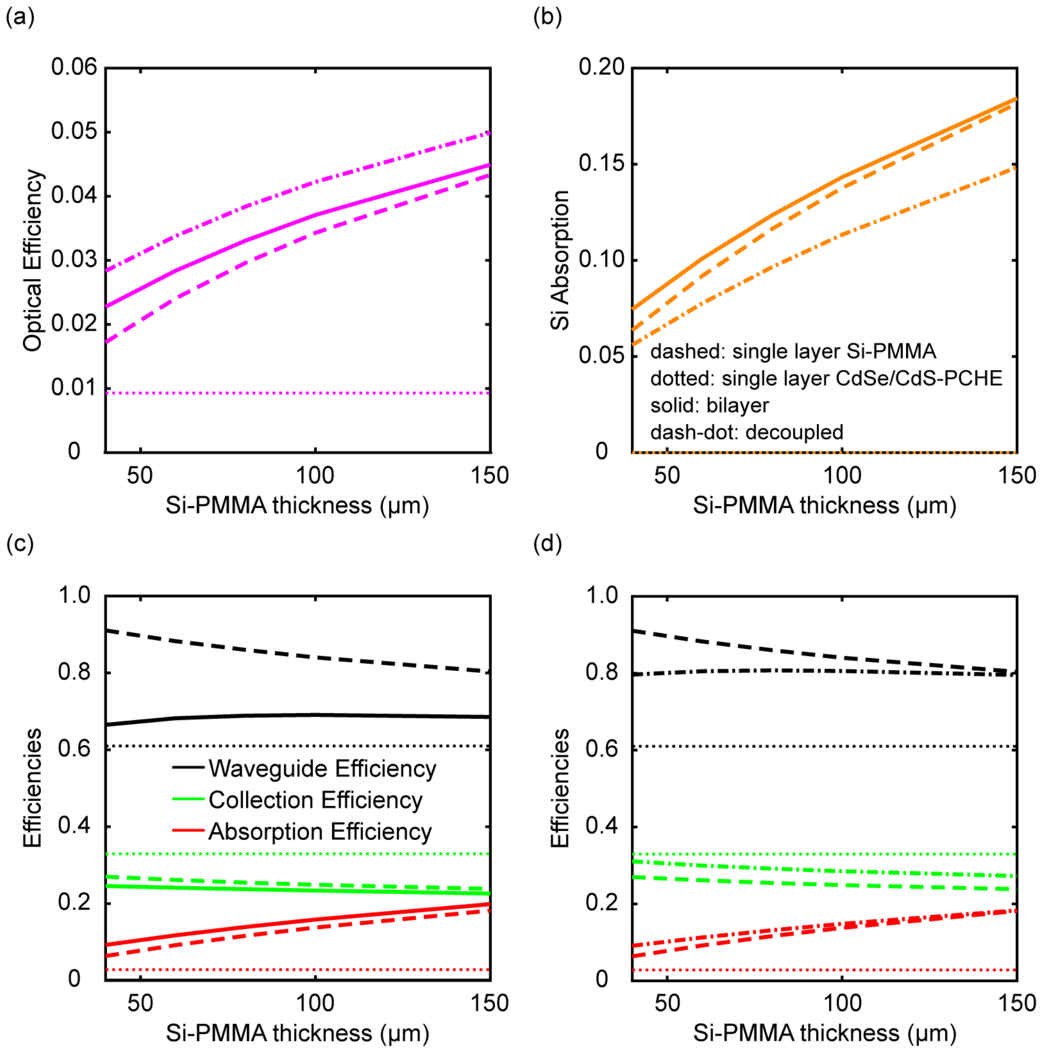

Figure 3.8: (a) Optical efficiency for a coupled bilayer device and decoupled device composed of Si-PMMA film and a CdSe/CdS-PCHE film while increasing the Si-PMMA thickness. (b) Total Si absorption efficiency while increasing Si-PMMA thickness. Waveguide efficiency, collection efficiency, and absorption efficiency for the (c) coupled bilayer device and the (d) decoupled device. Reference dashed and dotted lines are included for single layer Si-PMMA and CdSe/CdS-PCHE.

Si-PMMA film was set to ∼0.5 and scaled proportionately with Si-PMMA thickness. The thickness and optical density at 350 nm for the CdSe/CdS-PCHE film were held constant at 10 μm and 0.08, respectively. A thickness of 10 μm was used to stay within the ray optics regime for the ray-tracing simulations. Simulations were also performed for the films on separate, decoupled waveguides with an air gap in between, as this configuration is a common approach for tandem LSCs composed of multiple luminophores. Reference lines are included for single layer Si-PMMA and CdSe/CdS-PCHE efficiencies.

The optical efficiency (η_{opt}) of both the coupled and decoupled configurations increased when the CdSe/CdS-PCHE layer was added to the system, with the decoupled configuration showing slightly greater enhancement compared to the single layer Si-PMMA LSC (Figure 3.8a). The optical efficiency is defined as η_{opt} = Θ_2/Θ_1 where Θ_2 is the photon flux concentrated to the sides of the waveguide and Θ_1 is the photon flux incident on the LSC [45]. We can also express the optical efficiency as as $\eta_{opt} = \eta_{abs}\eta_{col}$, where η_{abs} is defined as

$$\eta_{abs} = \frac{\int (1 - T - R) E_{e,\lambda}\, d\lambda}{\int E_{e,\lambda}\, d\lambda} \tag{3.6}$$

where *T* and *R* are the LSC transmission and reflection, $E_{e,\lambda}$ is the solar spectral irradiance, and η_{col} is the fraction of absorbed photons that are successfully concentrated toward the edges of the concentrator. The waveguide efficiency (η_{wg}) which is the fraction of emitted photons coupled into total internal reflection modes that are concentrated to edges, is directly proportional to the collection efficiency and is also useful for characterizing how efficiently light propagates through the waveguide.

To understand the origin of the enhanced optical efficiency for both device configurations, we calculated the different efficiency terms (Figures 3.8b-d), as detailed in the Section 2.2.2. We first consider the Si absorption, which includes both light that is absorbed by the Si NCs directly and light that was initially absorbed by the CdSe/CdS NCs, emitted, and then absorbed by the Si NCs. Figure3.8b shows that the addition of the CdSe/CdS layer increased absorption in the Si in the bilayer configuration, consistent with the experimental measurements that showed that this layer sensitizes the Si absorption. In the decoupled configuration, adding the CdSe/CdS layer decreases the amount of light absorbed by the Si NCs, since a significant fraction of the incident sunlight is absorbed in the CdSe/CdS layer first. As expected, both devices exhibited an increase in absorption compared to the single junction Si-PMMA LSC because the addition of the CdSe/CdS-PCHE layer added more absorbing material. The absorption efficiency increase for the bilayer device was slightly higher than the decoupled device because of the increased reflection from the additional glass-air interfaces in the latter case.

The waveguide efficiency η_{wg} for both systems (Figures 3.8c,d) decreased with the addition of the CdSe/CdS-PCHE film compared to the single layer Si-PMMA, with a more dramatic decrease for the bilayer LSC. This occurs because the reabsorption losses increase when the two luminophores are coupled together. As the Si-PMMA thickness increased, there was a slight increase in the waveguide efficiency in both cases, since a slightly higher percentage of light is directly absorbed by the Si NCs in thicker films. With such minimal reabsorption for the Si NC PL, this results in an increase in waveguide efficiency. The CdSe/CdS-PCHE single layer film had a lower waveguide efficiency compared to all other LSCs tested due to higher reabsorption losses. The experimentally estimated attenuation coefficient for the single layer CdSe/CdS-PCHE film was near zero (Figure 3.5), which would correspond to a very high waveguide efficiency. We attribute this inconsistency to the larger LSC size for the ray-tracing simulation. For large area LSCs, the larger overlap between the absorbance and PL spectra for the CdSe/CdS NCs compared to the Si NCs decreases the waveguide efficiency, as the PL coupled into total internal reflection modes has to propagate further to reach the LSC edge. The bilayer device is in a regime, however, where the overall waveguide efficiency is higher compared to the single junction CdSe/CdS-PCHE. This is in part due to the energy transfer from the CdSe/CdS NCs to the Si NCs. Si PL successfully emitted into total internal reflection modes has a very high waveguide efficiency, regardless of whether the absorption was from incident sunlight or from reabsorbed CdSe/CdS PL.

The η_{col} shows different trends than η_{wg}, with the bilayer exhibiting a decreased η_{col} and the decoupled device exhibiting an increased η_{col} compared to the single layer Si-PMMA. Similar to η_{wg}, η_{col} for the bilayer device decreased because of the increase in reabsorption associated with having the two luminophores in close proximity. For the decoupled device, η_{col} was higher when compared to the single layer Si-PMMA because the effective PLQY

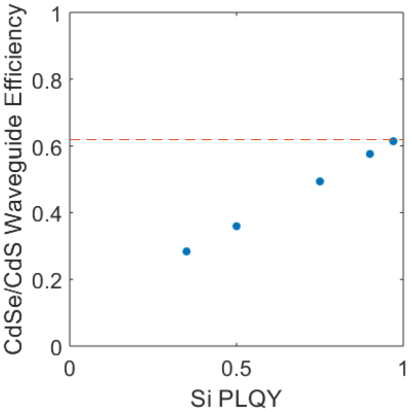

Figure 3.9: Waveguide efficiency of light directly absorbed by the CdSe/CdS NCs in the bilayer LSC while increasing the PLQY of the Si NCs. The red reference line is the waveguide efficiency of the CdSe/CdS-PCHE single layer LSC.

of the device has a strong effect. The higher PLQY of the CdSe/CdS in these simulations enhanced η_{col} despite the increase in reabsorption after the introduction of CdSe/CdS.

Therefore, we see that the addition of the CdSe/CdS layer has different effects for the two geometries. For the decoupled device, the CdSe/CdS-PCHE layer increased both η_{abs} and η_{col}; thus, more sunlight is absorbed, and the absorbed light is utilized more efficiently. Adding the CdSe/CdS-PCHE layer to the bilayer device only increases η_{abs}, but in this case the increase in absorption was more dominant than the decrease in η_{col} which led to the overall increase in η_{opt}. In principle, it would be possible for sensitization in the bilayer case to enhance collection efficiency; if the top layer luminophore had significant reabsorption or a low quantum yield, then transferring these photons to the low reabsorption Si would be beneficial. To better understand this regime, for our luminophore, we calculated the waveguide efficiency for the light that is directly absorbed by the CdSe/CdS NCs in the bilayer LSC as a function of the η_{PLQY} of the Si NCs (Figure 3.9). This is different from the overall waveguide efficiency from Figure 3.8 because it excludes photons that are directly absorbed by the Si NCs and do not interact with the CdSe/CdS NCs, but it does include photons emitted from CdSe/CdS NCs and reabsorbed by Si NCs. The red dashed line denotes the waveguide efficiency of the CdSe/CdS-PCHE single layer LSC.

When the η_{PLQY} of the Si NCs is too low, then this waveguide efficiency will decrease compared to the single layer case, as there is a high probability of absorption of the CdSe/CdS PL by the Si NCs, as shown in the figure. With increasing Si NC PLQY, the waveguide efficiency increases; however, for a CdSe/CdS PLQY of 0.75 the Si PLQY would have to be near unity to match or exceed the waveguide efficiency of the CdSe/CdS-PCHE single layer. It is important to note that the *overall* waveguide efficiency for the bilayer device is higher than the CdSe/CdS-PCHE single layer LSC, and this figure only studies light that was initially absorbed by the CdSe/CdS NCs.

3.4.5 Tunable Transmission for Agrivoltaics

Another advantage of an LSC design with two different luminophores is that the optical density of the luminophores can be adjusted independently to tune the transmission across different spectral regions. This feature may make the bilayer LSC design advantageous for agrivoltaic applications such as greenhouse panels where controlling the spectral quality can influence plant growth and morphology. To demonstrate this tunable transmission for our system, the transmission of the Soret band and the Q-band was calculated for both chlorophyll *a* and chlorophyll *b* while adjusting the optical density of Si and CdSe/CdS NCs. We define the chlorophyll band transmission as

$$T_{Chl} = \frac{\int T_{LSC}(\lambda)\epsilon_{Chl}(\lambda)\,d\lambda}{\int \epsilon_{Chl}(\lambda)\,d\lambda} \tag{3.7}$$

with the Soret band integrated from 350 to 550 nm and the Q-band integrated from 550 to 700 nm, shown in Figure 3.10. Changing the optical density for both luminophores tunes the Soret and Q-band transmission for both chlorophyll *a* and *b*. The Soret band transmission spans a larger range than the Q-band transmission because the absorbance of the luminophores increases with decreasing wavelength, which is potentially advantageous for cases where higher blue light percentage decreases plant mass [83, 84].

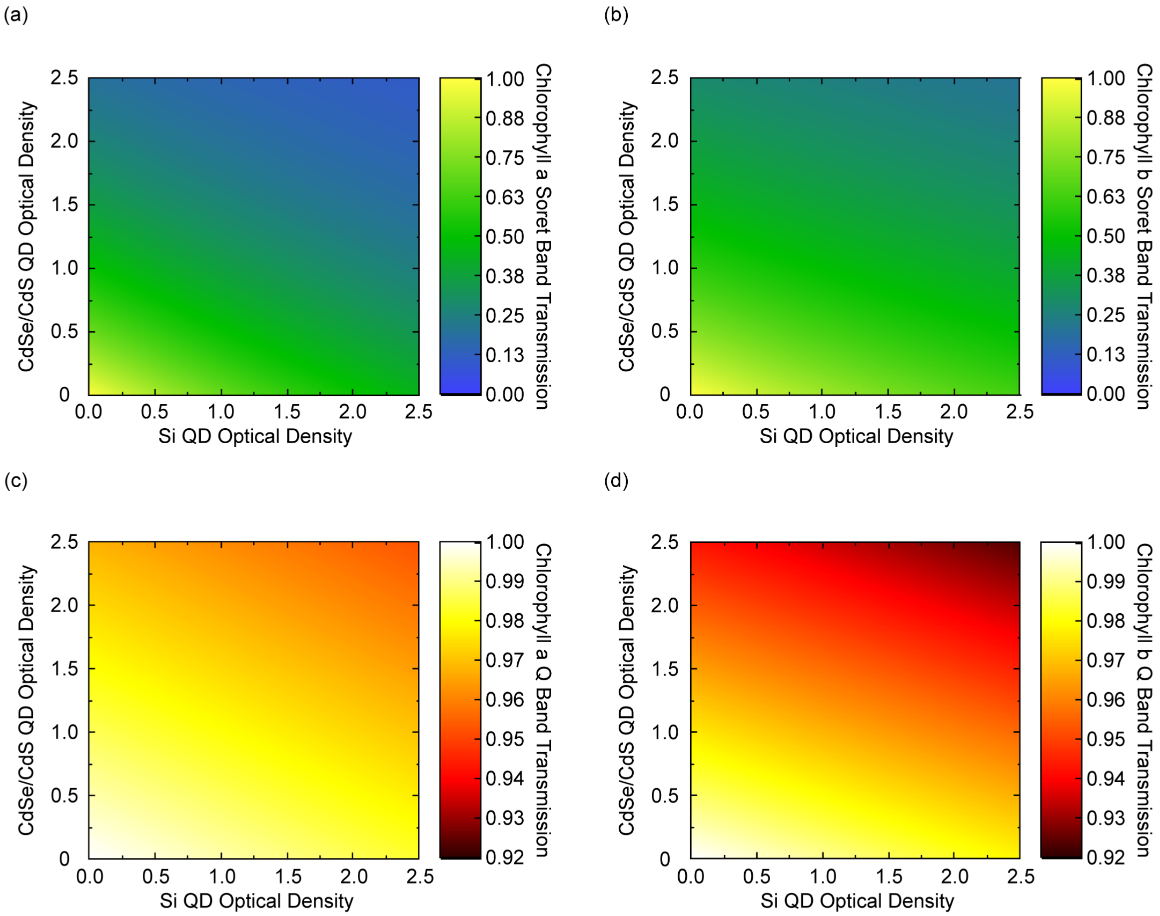

Figure 3.10: Colormaps of the (a) chlorophyll a *Soret band, (b) chlorophyll* b *Soret band, (c) chlorophyll* a *Q-band, and (d) chlorophyll* b *Q-band transmission while adjusting the optical density of the Si and CdSe/CdS NCs. The optical density is defined at 350 nm wavelength of incident radiation.*

3.5 Conclusion

This chapter on bilayer LSCs demonstrates that the addition of a CdSe/CdS composite layer to the top of a Si LSC enhances the optical efficiency by increasing the absorption and sensitizing the low-loss Si absorption, while tuning the transmission for modified spectral quality. Concentrated photoluminescence from both luminophores was detected by using attenuation measurements, with increased CdSe/CdS PL attenuation from absorption by the Si NCs. This luminophore interaction decreases the overall collection efficiency of the device but boosts the absorption efficiency, which results in higher optical efficiency. The CdSe/CdS NC to Si NC energy transfer is advantageous as the Si PL has exceptionally high waveguide efficiency with minimal reabsorption. Although the simulations for the decoupled configuration predicted higher optical efficiency than the bilayer, the bilayer device offers numerous advantages, including overall simplicity. This system also allows for control of the transmission across the spectral range of the chlorophyll absorption bands, which makes this type of device promising for agrivoltaic LSC applications.

Chapter 4

Directional Control of Photoluminescence for Improved Spectral Quality of Filtered Transmisison

4.1 Introduction

The previous chapter describes a method to improve the tunability of LSCs for agrivoltaic applications by introducing multiple luminophores into the same waveguide. This chapter investigates the benefits of controlling the PL outcoupling direction in LSC waveguides and develops an optimization scheme to design thin-film stacks to improve the spectral quality of the transmitted light. Controlling the outcoupling of light has multiple benefits, including tailoring the transmission spectrum for daylighting or crop production, and directing PL toward either crop species or the PV cells.

Creating a multilayer thin-film stack with varying refractive indices and thicknesses on the order on the wavelengths of light can manipulate the photon density of states. A common example of this is a 1-dimensional photonic crystal or Bragg mirror. Embedding luminophores in photonic crystals has been demonstrated to increase the trapping efficiency of LSCs to greater than 90% [95, 96]. In this case, the goal is to embed films of TiO_2-PVP into a CdSe/CdS-PCHE to create a multilayer stack that will create preferential emission out one LSC face (toward the plants) while still concentrated some of the

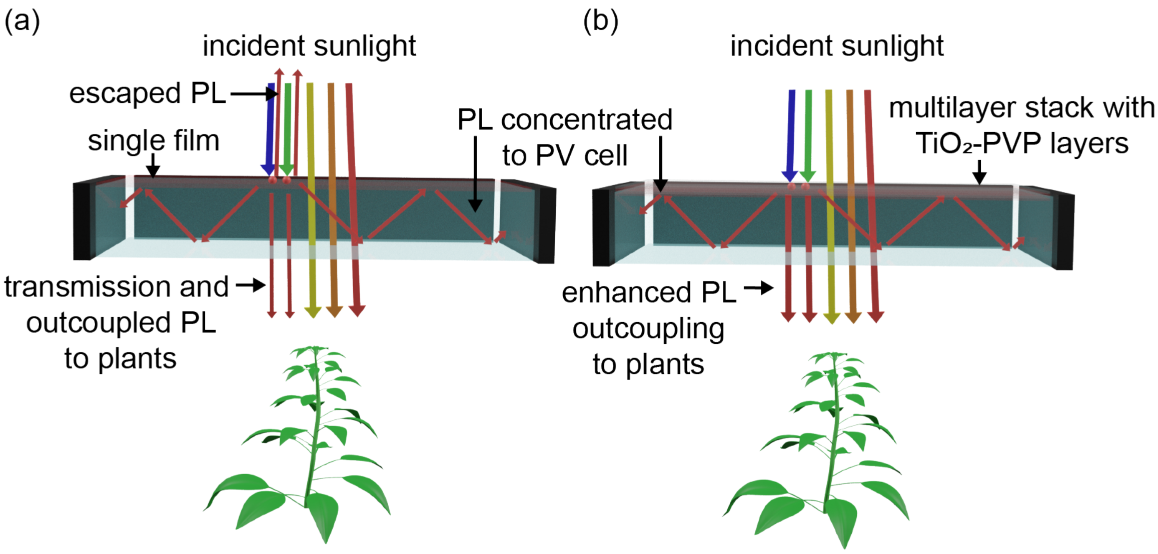

Figure 4.1: Schematic of an agrivoltaic LSC (a) without the inserted TiO_2*-PVP films and (b) with the inserted* TiO_2*-PVP to create the multilayer stack. PL is photoluminescence.*

PL toward PV cells. Unlike Bragg mirrors, the stack does not need to be periodic, and likely will not. Figure 4.1 shows a schematic of an LSC without any inserted film (Figure 4.1a) and the desired effect after designing the multilayer stack (Figure 4.1b). To design the stack, a needle insertion method is used where TiO_2-poly(vinyl pyrrolidone) (TiO_2-PVP) nanocomposites with varying refractive indices are inserted into photoluminescent CdSe/CdS-poly(cyclohexylethylene) (CdSe/CdS-PCHE) films on a glass waveguide to create an LSC design that has both high transmission and directs PL toward plant species.

4.1.1 Spectral Quality Metrics for Agrivoltaics

The photon flux density and spectrum of light incident on plants has a profound effect on plant growth and crop production [81–84, 97, 98]. Increasing the photosynthetic photon flux densities (PPFD) improves the net photosynthetic rate of plants which will yield faster plant growth [98]. The PPFD is defined by the following equation:

$$PPFD = \sum_{350nm}^{725nm} \phi_i \tag{4.1}$$

where ϕ_i is the total photon flux density incident on the plants. Equation 4.1 can also be expressed with reduced wavelength ranges like red photon flux from 550 nm to 725 nm. In addition to the photon flux density, the ratio of red to blue light, or the RB ratio influences plant yield. For example, Pennisi, *et al.* studied lettuce under varying RB ratios and found an RB ratio of three yielded the highest plant weight and mass [97]. The RB ratio is described by the following equation:

$$RBRatio = \sum_{550nm}^{725nm} \phi_i / \sum_{350nm}^{550nm} \phi_i \tag{4.2}$$

As discussed in Section 3.2, studies where plants are illuminated through fluorescent panels, which red shifts the filtered transmission, demonstrated enhanced plant growth [49, 99]. A significant component of the red shift is from the contribution of luminophores with red PL contributing to the filtered transmission. Increased control over the PL outcoupling enhances this effect and allow for more flexibility of the filtered spectrum.

In addition to spectral shifting, the angular distribution of the light incident on plants influences plant growth and crop production. Diffuse sunlight can penetrate deeper in the plant canopy and better illuminate inner leaf layers [100–102]. Photosynthesis saturates at higher light intensities, so photosynthetic rates are often higher if many leaves receive moderate light intensity than if only a few leaves receives high intensity [101]. Diffuse covers on greenhouses have been demonstrated to increase crop production [103, 104].

4.2 Methods

4.2.1 Merit Functions

Multiple merit function functions were tested for needle insertion algorithm. The first merit function tested included three terms: the absorption efficiency (η_{abs}), extraction efficiency ($\eta_{extraction}$), and red light transmission (T_{red}). The function is described by the following:

$$Merit\ Function\ A = \left[\frac{\int_{550nm}^{800nm} \left(\eta_{abs}\eta_{extraction} + T_{red} \right) \, d\lambda}{\int_{550nm}^{800nm} \phi_S \, d\lambda} \right]^{-1} \tag{4.3}$$

$\eta_{extraction}$ is defined as the fraction of dissipated dipole power that couples out of the thin-film, through the glass substrate into air, and toward the plant species [105]. The product of $\eta_{extraction}$ and η_{abs} in Equation 4.3 is defined as the outcoupling efficiency. ϕ_S is the incident solar photon flux. The merit function targets the red half of the solar spectrum by integrating only from 550 nm to 800 nm. The function is inverted, as merit functions for this optimization method must be minimized.

Variations of the merit function were tested by first narrowing the wavelength range to 575 nm to 675 nm to target the PL spectrum of the CdSe/CdS nanocrystals. This is described by the following:

$$Merit\ Function\ B = \left[\frac{\int_{575nm}^{675nm} \left(\eta_{abs}\eta_{extraction} + T_{red} \right) \, d\lambda}{\int_{575nm}^{675nm} \phi_S \, d\lambda} \right]^{-1} \tag{4.4}$$

In the next variation, the transmission component was removed to only optimize the luminophore outcoupling described by the following:

$$Merit\ Function\ C = \left[\frac{\int_{575nm}^{675nm} \left(\eta_{abs}\eta_{extraction} \right) \, d\lambda}{\int_{575nm}^{675nm} \phi_S \, d\lambda} \right]^{-1} \tag{4.5}$$

Lastly, the merit function was reduced to just the extraction efficiency described by the following:

$$Merit\ Function\ D = \left[\frac{\int_{575nm}^{675nm} \left(\eta_{extraction} \right) \, d\lambda}{\int_{575nm}^{675nm} \phi_S \, d\lambda} \right]^{-1} \tag{4.6}$$

4.2.2 Nanocomposite Films

The photoluminescent nanocomposite assumed for the optimization was CdSe/CdS-PCHE. This nanocomposite has been tested previously and shown to disperse the nanocrystals well up to about 9 vol%. The complex refractive index for the CdSe/CdS-PCHE nanocomposites can be described by the Maxwell-Garnett effective medium approximation [70].

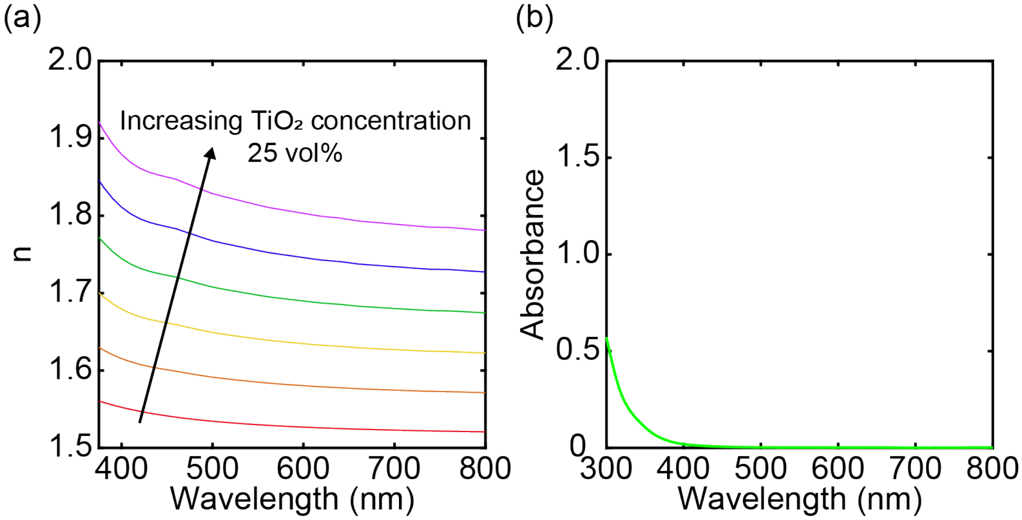

Figure 4.2: (a) Refractive index of the TiO_2-PVP nanocomposite with increasing concentration. (b) PVP absorbance measured with UV/vis spectrophotometry.

The needle insertion algorithm also requires the insertion of a films with various refractive indices. For this, a nanocomposite of TiO_2-PVP was assumed, and the refractive index was modeled with a Maxwell-Garnett effective medium approximation. The refractive index of the TiO_2-PVP nanocomposite is reported in Figure 4.2 along with the absorption spectrum of PVP measured by doing UV-vis spectrophotometry on PVP dissolved in butanol. The refractive index of the TiO_2-PVP nanocomposite can be tuned from 1.55 to 1.8 by varying the TiO_2 concentration which provides variability for the needle insertion algorithm to test and optimize. There is PVP absorption in the UV which could interfere with CdSe/CdS absorption, but importantly there is minimal absorption near the CdSe/CdS PL spectrum.

Experimentally, nanocrystalline TiO_2-polymer hybrids have been achieved with high titania content up to 90 wt% and a nanocrystalline TiO_2 domains of 3-4 nm as reported in literature [106]. TiO_2-epoxy nanocomposites have also been realized using a sol-gel method with a titania concentration of 90 wt% and average particle size of 10 nm [107].

These synthesis methods could be adapted for the TiO_2-PVP composites. This chapter does not discuss the experimental realization of these films, as the focus was on the optical design of the multilayer thin-film stacks.

4.2.3 Needle Insertion Algorithm

A needle insertion algorithm is a thin-film stack optimization method that inserts a thin-film into an initial stack while systematically changing the position and refractive index to see which configuration reduced the merit function most significantly. In our case, the inserted film was a TiO_2-PVP nanocomposite and the initial film was a 4 vol% CdSe/CdS-PCHE film with a thickness of 800 nm on a glass substrate with a thickness of 1.6 mm. Once a film and position was chosen, thicknesses of every layer were adjusted until the merit function reached a minimum for the new stack. If the thickness was adjusted to zero, that film was removed from the stack. Figure 4.3 describes the optimization process flow in more detail.

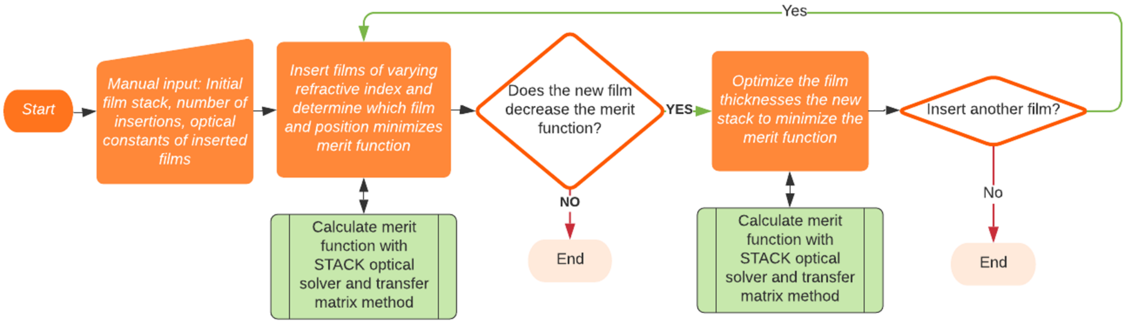

Figure 4.3: Flow chart describing the needle insertion optimization process.

The outcoupling efficiency for the merit function was determined using an analytical multilayer optical solver, Lumerical STACK, that calculates the fraction of dissipated dipole power from the photoluminescent CdSe/CdS-PCHE films downward through the glass into air. The dipole was treated as unpolarized by averaging the three dipole orientations together, and results were averaged over the PL spectrum for the CdSe/CdS nanocrystals reported previously in Figure 3.3. The transmission through the thin-film stack and absorption was calculated with transfer-matrix method assuming normally incident AM1.5G solar spectrum, and the reflection off the bottom surface of the substrate was accounted using Fresnel coefficients. The needle insertion algorithm was run with a maximum of two film insertions.

4.3 Results and Discussion

4.3.1 LSC with Ideal Directional Photoluminescence

Before the optimization algorithm was tested, the theoretical advantage of controlling the PL outcoupling was explored to understand the effect on the RB ratio and outcoupled photon flux density. The transmitted and outcoupled spectra for LSCs with one type of luminophore is controlled and limited by the luminophore type, optical density, and refractive index of the waveguide. For a refractive index of 1.5, the escape cone of the PL from one LSC face is 12.5%. If this extraction efficiency can be controlled, metrics like the RB ratio can be manipulated. To demonstrate this advantage, an analytical calculation was done assuming an LSC with CdSe/CdS nanocrystals to estimate the RB ratio and red photon flux density while adjusting the absorption efficiency. The absorption and transmission was estimated with Beer's law and the outcoupled flux was added directly to the transmission assuming unity PLQY. The results are shown in Figure 4.4.

The 50% extraction efficiency indicates 50% of the PL from the luminophores escaped out of the shadow-side of the LSC, creating preferential PL outcoupling toward plant species. When the extraction efficiency is increased to 50%, the RB ratio range when adjusting the absorption efficiency is increased by 13%. The increase is because a higher flux of red PL is added to the transmitted flux which increases the ratio of the blue to red light that is filtered through the LSC. For the red photon flux, there are only small changes with absorption efficiency when the extraction efficiency is 12.5%, but the available red photon flux range extends dramatically with an outcoupling of 50%. This theoretical example in Figure 4.4 demonstrates further motivation for designing an LSC that can achieve

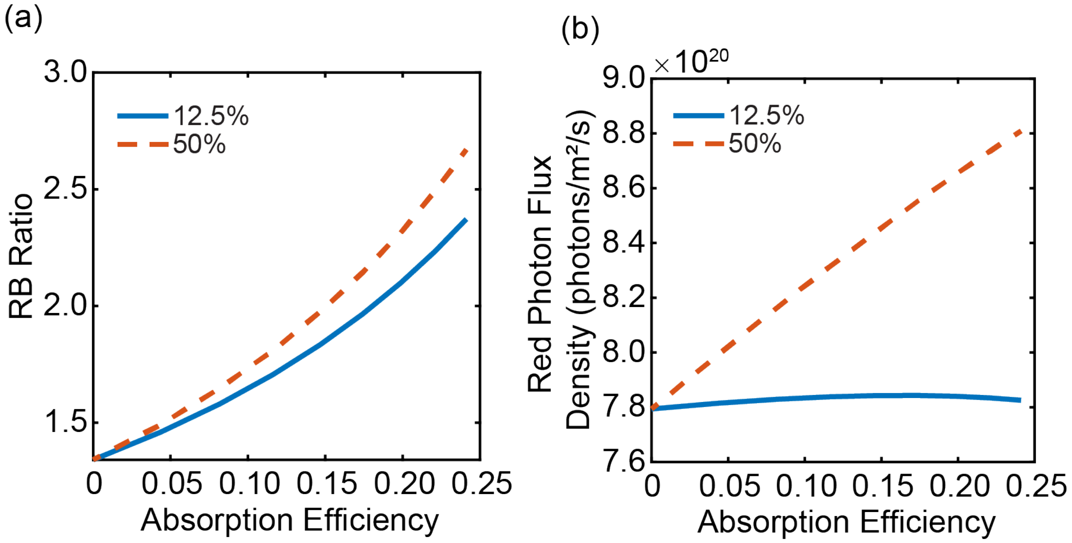

Figure 4.4: (a) RB Ratio and (b) red photon flux density with increasing CdSe/CdS absorption efficiency for an extraction efficiency of 12.5% and 50%.

preferential outcoupling out one LSC face.

4.3.2 Thin-Film Stack Optimized Results

The resulting optimized thin-film stacks from the needle insertion algorithm for the 4 merit functions tested are given in Figure 4.5 along with the absorption efficiency, extraction efficiency, outcoupling efficiency, and the transmitted and outcoupled photon flux. The merit functions tested include the transmission term (A and B) converge to a solution with two films inserted, a 25 vol% TiO_2-PVP film and a non-doped PVP film. The optimized structures mainly increase transmission within the integrated spectral range. The extraction efficiency was reduced in both cases, which is the opposite of what was desired. The transmission optimization does, however, make a noticeable difference in the transmitted and outcoupled photon flux after optimization compared to the original film.

Experimental realization of a transparent 25 vol% TiO_2-PVP nanocomposites would be challenging when considering particle size, interparticle spacing, and aggregation. The theoretical ratio between the estimated particle spacing (S) and particle diameter (d) for a specific volume fraction (f) can be estimated using the following equation [71]:

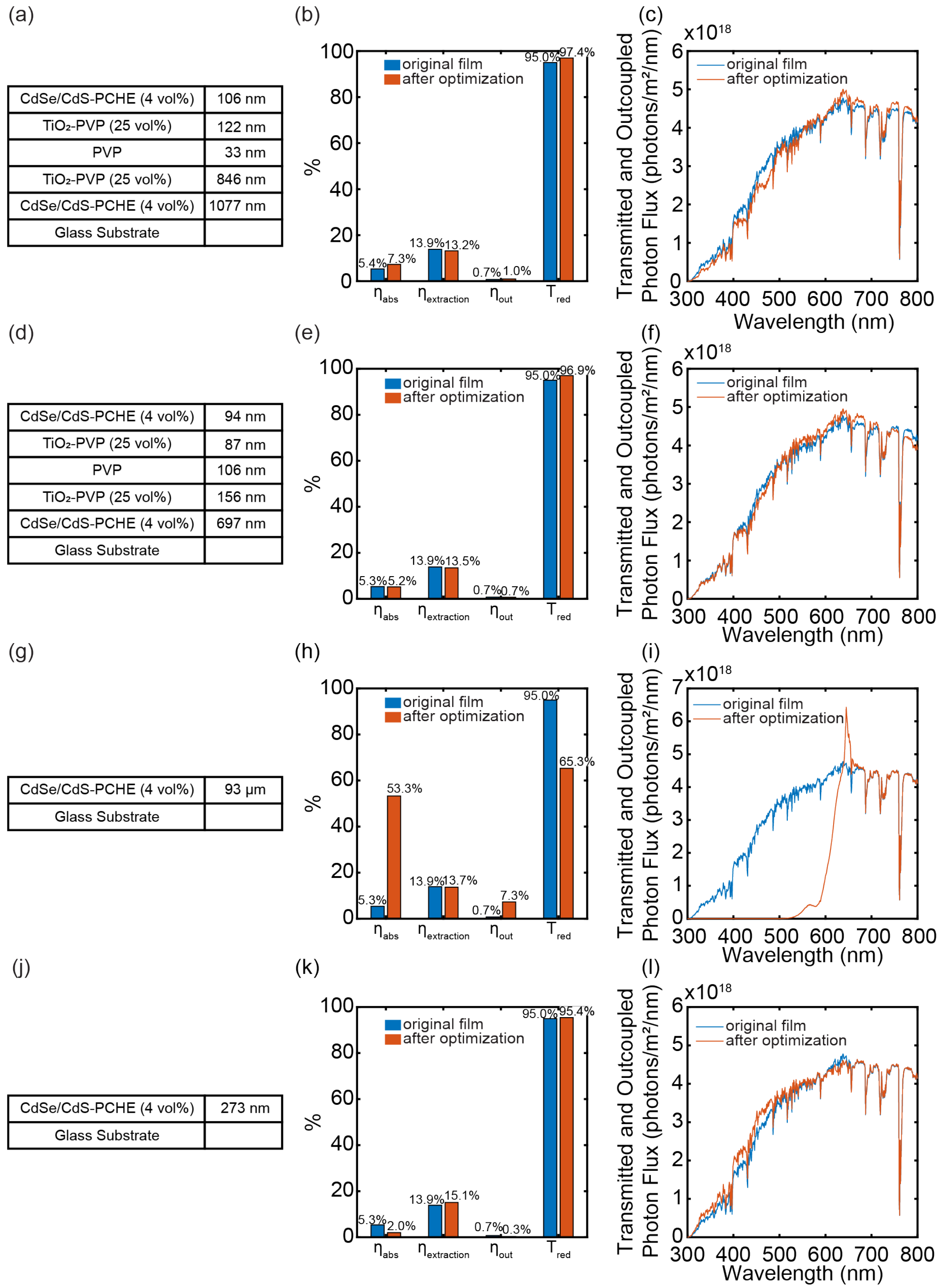

(a)

CdSe/CdS-PCHE (4 vol%)	106 nm
TiO_2-PVP (25 vol%)	122 nm
PVP	33 nm
TiO_2-PVP (25 vol%)	846 nm
CdSe/CdS-PCHE (4 vol%)	1077 nm
Glass Substrate	

(d)

CdSe/CdS-PCHE (4 vol%)	94 nm
TiO_2-PVP (25 vol%)	87 nm
PVP	106 nm
TiO_2-PVP (25 vol%)	156 nm
CdSe/CdS-PCHE (4 vol%)	697 nm
Glass Substrate	

(g)

CdSe/CdS-PCHE (4 vol%)	93 μm
Glass Substrate	

(j)

CdSe/CdS-PCHE (4 vol%)	273 nm
Glass Substrate	

Figure 4.5: Results of the needle insertion algorithm for Merit function (a-c) A, (d-f) B, (g-i) C, and (j-l) D. The first column (a,d,g,j) shows the resulting thin-film stack after two film insertions. The second column (b,e,h,k) gives the absorption efficiency, extraction efficiency, outcoupling efficiency, and red transmission (550 nm-800 nm) of the LSC before and after optimization. The third column (c,f,i,l) is the transmitted and outcoupled photon flux from the LSC before and after optimization.

$$S/d = \sqrt[3]{\frac{\pi}{6f}} \tag{4.7}$$

For a volume fraction of 0.25, S/d is 1.28, which means the distance between particles is only slightly larger than particle diameter. It is theoretically possible to achieve good particle dispersion at this concentration with sufficient nanoparticle-polymer interaction [108], but the small particle size ($<$ 10 nm) required to avoid significant Rayleigh scattering means the interparticle spacing would be only a few nanometers [109, 110]. Such close spacing leaves little space for ligands and the organic matrix and could limit the achievable concentration for this nanocomposite.

The high concentration TiO_2-PVP composite could also have significant particle aggregation which induces scattering. Scattering diminishes the waveguide and optical efficiency of the device which would lead to lower photovoltaic efficiency of the LSC [42, 71]. As discussed in section 4.1.1, diffuse sunlight often results in higher photosynthetic rates for plant species. Scattering from particle agglomeration would assist in diffusing the transmitted sunlight not absorbed by the luminophores. Before implementation, the tradeoffs between the providing diffuse transmission and high photovoltaic efficiency requires further evaluation.

We adjusted the merit function to add more weight to the extraction efficiency by removing the transmission dependence (Figure 4.5g-i). The optimization scheme did not converge on a solution where inserting films reduced the merit function, rather the solution converged on a much thicker CdSe/CdS-PCHE film at 93 μm. In this case, the total outcoupled photon flux was maximized by increasing the absorption efficiency in the nanocomposite film, not by designing a thin-film stack with directional emission.

The last adjustment to the merit function was to remove the absorption efficiency dependence as described in Equation 4.6. The needle insertion algorithm did not converge to a solution that inserted any TiO_2-PVP films, but rather adjusted the thickness of the CdSe/CdS-PCHE film to 273 nm. This solution was the only solution that increased the extraction efficiency, but it only did so slightly from 13.9% to 15.1%. The reduction in thickness also diminished the absorption significantly such that the overall outcoupling efficiency was reduced.

4.4 Conclusion

This chapter described the agrivoltaic spectral quality benefits of developing an LSC with preferential photoluminscence outcoupling out one face, and proposed a needle insertion optimization algorithm to design a thin-film stack to increase outcoupling of one LSC face while maintaining high red-light transmission. Increasing the extraction efficiency to 50% as opposed to 12.5% enhanced the RB ratio and red photon flux density range while increasing the luminophore absorption efficiency. The merit functions tested that included the transmission term converged on a 5-layer stack design that increased the red-light transmission but had a negative effect on the extraction efficiency. The merit function described by Equation 4.5 that only considered outcoupling efficiency converged on a single film design that maximized luminophore absorption. The merit function that only considered extraction efficiency did increase the extraction efficiency but only incrementally.

Future work on designing thin-film stacks to achieve a controlled emission direction should consider more complex thin-film stacks to achieve greater increase in the extraction efficiency. Other approaches like textured surfaces to disrupt waveguide modes and preferentially scatter out one LSC face should also be explored as demonstrated by previous literature [105, 111]. Further consideration to how LSC designs influence the waveguide efficiency of the LSC is also necessary to ensure high photovoltaic efficiency.

Chapter 5

Optical Coupling Efficiency Efficiency Estimates for c-Si PERC Modules Enhanced with Downconverting Films and Nanocomposites

5.1 Introduction

The previous chapters focused on the multifunction properties of downshifting luminescent solar concentrators and methods to optimize their multifunctional properties. This chapter discusses applying downconversion to a Si PERC solar cell to enhance the photocurrent and efficiency. As introduced in chapter 1, a critical property controlling the photovoltaic efficiency enhancement from downconversion is the optical coupling efficiency ($\eta_{opt,DC}$), or how efficiently the downconverted light couples into the active layer of the solar cell to generate electricity. Analytical thermodynamic studies on downconversion for photovoltaics typically base the optical coupling efficiency on the etendue assuming the downconversion material and solar cell have the same refractive indices, or assuming that isotropic PL leads to a coupling efficiency downward into the Si cell of 0.5 [7, 8, 112, 113]. For simplified systems, these assumptions are valid, but with thin-film downconverting materials, and the anti-reflection coatings and pyramidal surface textures present in crystalline-Si (c-Si) solar cells, these assumptions for the optical coupling efficiency will not hold. More recently, a ray-tracing study on Yb-doped CsPb($Cl_{1-x}Br_x$)$_3$ perovskites applied to Si photovoltaic cells made improvements in the optical modeling of these devices, and demonstrated that the location of the downconverting material in the module stack influences the coupling efficiency and module performance [114].

In this chapter we combine wave and ray optics techniques to model the optical coupling efficiency, loss mechanisms, and efficiency metrics for downconverting films integrated into a c-Si module, accounting for realistic module architectures. We used these techniques to gain a deeper understanding of the impact of the location of the downconverting material within the module and the corresponding efficiency enhancement. These results guide the design of both materials and devices, allowing downconversion to reach its full potential in photovoltaics.

5.2 Methods

5.2.1 Downconverting Material Refractive Index Modeling

The downconverting film refractive indices were modeled using a Tauc-Lorentz oscillator model described by the following equation:

$$\begin{aligned}\epsilon_{TL}(E) = \epsilon_\infty + \frac{AC}{\pi\zeta^4} * \frac{a_{in}}{2\alpha E_0} ln(\frac{E_0^2 + E_g^2 + \alpha E_g}{E_0^2 + E_g^2 - \alpha E_g}) \\ -\frac{A}{\pi\zeta^4}\frac{a_{atan}}{E_0}[\pi - atan(\frac{2E_g + \alpha}{C}) + atan(\frac{-2E_g + \alpha}{C}] \\ +2\frac{AE_0}{\pi\zeta^4\alpha}E_g(E^2 - \gamma^2)[\pi + 2atan(2\frac{E^2 - \gamma^2}{\alpha C})] \\ -\frac{AE_0C}{\pi\zeta^4\alpha}\frac{E^2 + E_g^2}{E} ln(\frac{\mid E - E_g \mid}{E + E_g}) \\ +2\frac{AE_0C}{\pi\zeta^4}E_g ln(\frac{\mid E - E_g \mid (E + E_g)}{\sqrt{(E_0^2 - E_g^2)^2 + E_g^2 C^2}})\end{aligned} \tag{5.1}$$

The absorption peak strength (A) was 50 eV, the broadening term (C) was 1.2 eV, the optical band gap energy (Eg) was 2.25 eV, the energy of maximum transition (E0) was 4.5 eV, and the ϵ_∞ = 1.4 (Figure 5.1).

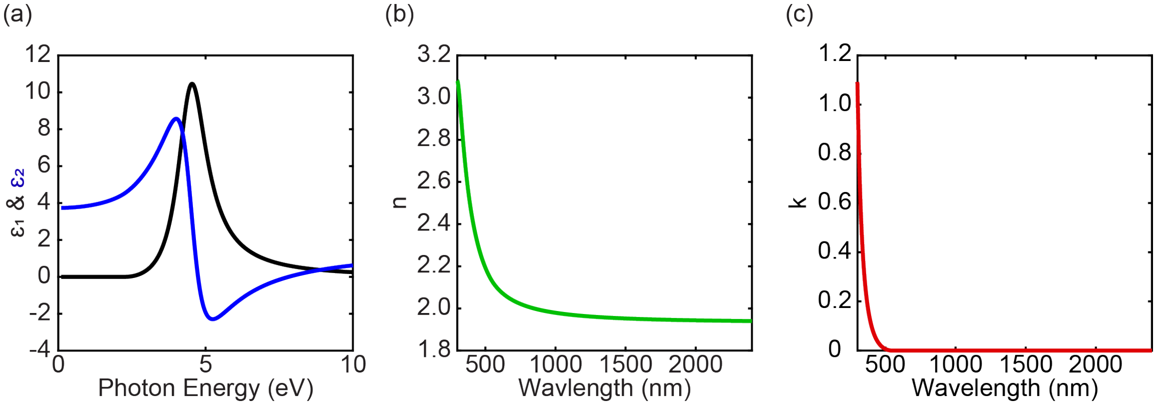

Figure 5.1: (a) Dielectric function, (b) refractive index, and (c) extinction coefficient of the downconverting film material calculated with the Tauc-Lorentz oscillator model.

A nanocomposite material of downconverting perovskite nanocrystals dispersed in EVA was modeled with a Maxwell-Garnett effective medium approximation using the Tauc-Lorentz dielectric function as the inclusion material and ethylene-vinyl acetate (EVA) dielectric function (ϵ_{EVA}) as the matrix (Figure 5.2). The Maxwell-Garnett effective medium approximation is described by [115]:

$$\epsilon_{NC-EVA} = \epsilon_{EVA} \frac{2\delta_i(\epsilon_{TL} - \epsilon_{EVA}) + \epsilon_{TL} + 2\epsilon_{EVA}}{2\epsilon_{EVA} + \epsilon_{TL} - \delta_i(\epsilon_{TL} - \epsilon_{EVA})} \tag{5.2}$$

δ_i is the volume from of the downconverting nanocrystals in the nanocomposite. The nanocomposite was assumed to have negligible scattering from matrix imperfections and nanocrystal agglomeration.

5.2.2 Finite-Difference Time-Domain Simulations

Finite-difference time-domain (FDTD) simulations were performed using Ansys Lumerical. The simulations were conducted in 3-dimensions by placing a dipole source at varying heights in the downconverting layer and averaged over 3 different dipole orientations. The simulation width and depth was 16 µm and the height was 4 µm. 2-dimensional monitors were placed above and below the downconverting film in either the EVA, glass, or Si far enough away from the downconverting film to avoid detecting evanescent fields. Other

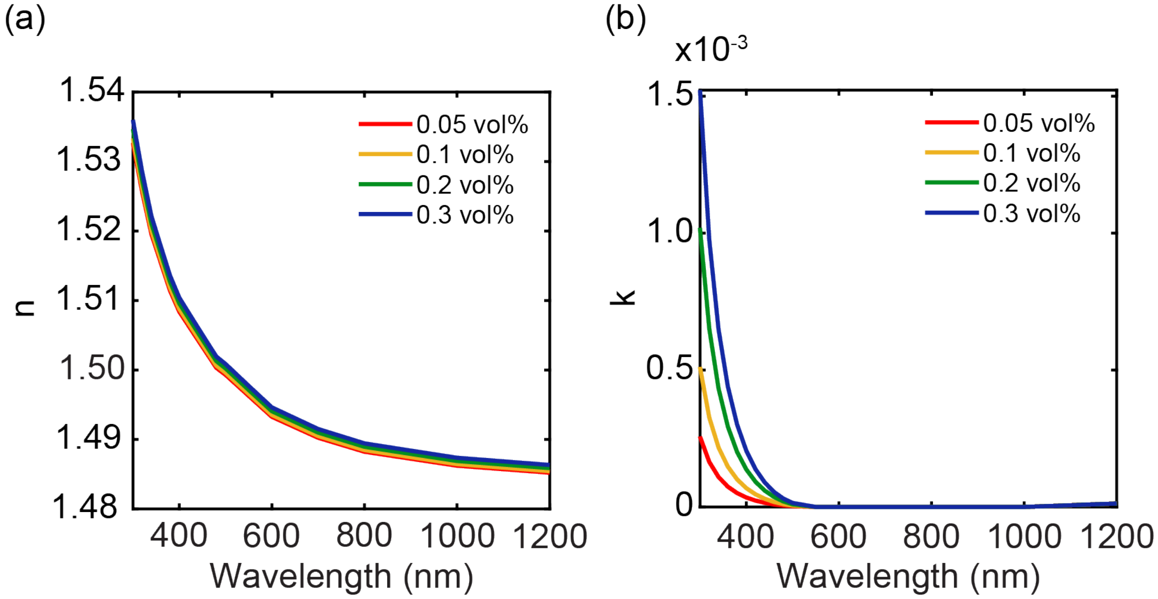

Figure 5.2: Real and imaginary component of the complex refractive indices for the downconverting nanocrystal-EVA nanocomposite.

2-dimensional monitors were placed in the downconverting film to detect trapped modes. All boundary conditions were perfectly matched layers.

5.2.3 Analytical Multilayer Optical Simulator

Analytical multilayer optical calculations were performance with Ansys Lumerical STACK. The same refractive index and wavelength inputs used for the FDTD simulations were used for the layers in the stack. The dipole was modeled as unpolarized, and the PL projected into the far-field was extracted as a function of emission angle. The main contribution of the FDTD simulations and analytical multilayer optical calculations to the efficiency estimates was the optical coupling efficiency described in Table 5.1.

5.2.4 SunSolve Simulations

SunSolve Power from PV Lighthouse was used to model the optical properties of the c-Si PERC module. The back contacts include an Al coating back electrode, a 1000 nm AlSi contact interface, and a 10 nm Al2O3 film followed by a 100 nm SiN$_x$ film for the non-contact interface. The contact interface is in a line pattern with a 200 µm width and

5000 μm pitch. The 170 μm thick crystalline Si layer has upright, random pyramidal texturing with a height and width of 5 μm and 7.813 μm. The cell anti-reflection coating (ARC) is a 75 nm thick SiN_x conformal film. The Ag front contact is in a grid pattern. Cell interconnection was modeled with 5 rectangular ribbons with a width of 1100 μm and height of 200 μm. There were 120 rounded rectangular fingers with 45 μm width and 15 μm height. The finger pitch and spacing were both 0.13 cm. 5 busbars were included with a width and height of 1100 μm and 15 μm. The encapsulation was assumed to be a 0.45 mm thick UV transmissive EVA [116], and the 3.2 mm thick front glass includes a 110 nm porous silica ARC. The interface with EVA was flat. The downconverting layer was either inserted between the glass and EVA layer or between the SiN_x and EVA, depending on the desired configuration. The EVA material optical constants were swapped with the nanocomposite optical constants to test the nanocomposite configuration device. Each cell is a pseudosquare with a length and diameter of 15.675 cm and 21 cm. The 72 cell module has 6 cells per row and 12 cells per column with a cell separation of 0.5 cm. Optical scattering from the pyramidal texturing was modeled using a Phong model with an exponent α of 25 [117]. Scattering from the electrodes was modeled with a Lambertian distribution. The AM1.5G standard spectrum illumination was assumed to be full area with normal incidence, and no rear side illumination was included.

5.3 Results and Discussion

5.3.1 Solar Module and Downconverting Material Optical Properties

For the reference device, a typical c-Si passivated emitter rear cell (PERC) module was assumed. The module consisted of a 170 μm thick crystalline Si layer with random pyramidal texturing, a 75 nm SiN_x anti-reflection coating (ARC), 0.45 mm UV transmissive EVA encapsulant [116], 3.2 mm thick cover glass, and a 110 nm thick glass ARC. The interface between EVA and glass was assumed to be planar. Ag front electrodes were used in a grid layout, and Al coatings were used for the back electrode. Three downcon-

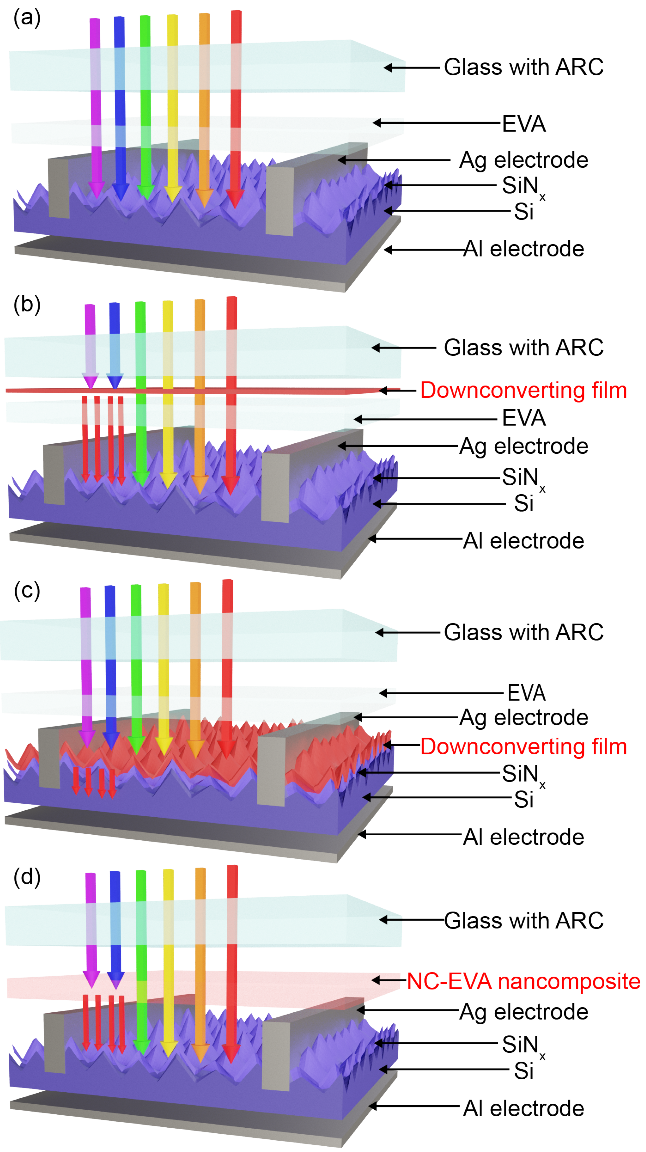

Figure 5.3: Illustrations of the (a) c-Si reference cell, (b) the downconverting film on glass configuration, (c) the downconverting film on cell configuration, and (d) the nanocrystal (NC)-EVA nanocomposite configuration.

verting configurations were tested by either adding or replacing layers within the reference stack (Figure 5.3). For the downconverting "film on glass" configuration, a downconverting film was added between the EVA and glass layers. For the downconverting "film on cell" configuration, a downconverting film was added between the SiN_x and EVA. Similar to the SiN_x coating, the downconverting film in the "film on cell" configuration conformally adopts the random pyramidal texturing of the Si surface, which has been demonstrated experimentally using vapor deposition methods [53]. A third configuration replaces the EVA encapsulation with a "nanocomposite" of downconverting nanocrystals embedded in EVA. We assume this is an idealized composite with no scattering, as can result from particle agglomeration or polymer inclusions [71].

The optical properties of the downconverting material were set to match the properties of Yb-doped CsPb($Cl_{1-x}Br_x$)$_3$ perovskites. The complex refractive index was modeled with a Tauc-Lorentz oscillator to create a strong absorption onset at 500 nm and a refractive index approaching n = 1.94 at longer wavelengths (Figure 5.1), as is expected from this type of perovskite [118,119]. The PL spectrum had a peak at 1000 nm and a full width half maximum of 43 nm [114]. The absorption and PL spectra are shown in Figure 5.4, along with the module external quantum efficiency of the reference PERC c-Si module and the AM1.5G solar spectral irradiance [120].

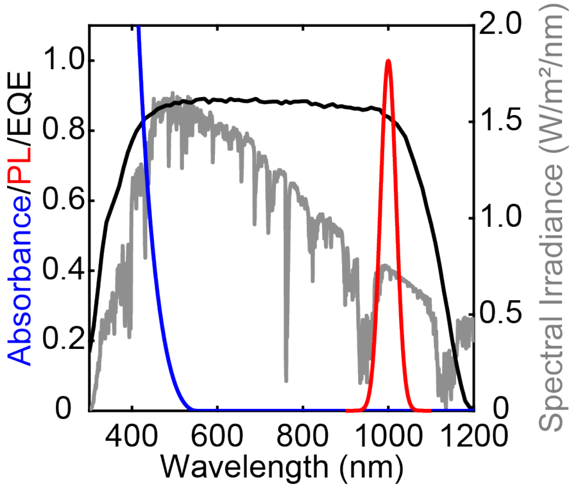

Figure 5.4: Simulated absorbance and PL spectra of the downconverting film along with external quantum efficiency (EQE) of the reference module. The AM 1.5G reference solar spectrum is also included [120].

5.3.2 Optical Coupling Efficiency

We first consider the angular dependence and coupling of the PL from the downconverting layer into the immediately adjacent layers using both FDTD simulations and an analytical multilayer optical simulator (Sections 5.2.2 and 5.2.3). The downconverting film thickness was initially set to 500 nm. The light source is a point dipole where we averaged across the three dipole orientations (Section 5.2.2), and the wavelength of the dipole PL ranged from 900 nm to 1100 nm with the results averaged over the PL spectrum. The downconverting film on glass configuration included glass immediately above the downconverting film and EVA below. The downconverting film on cell configuration consisted of EVA above the downconverting film and 75 nm of SiN_x on c-Si below. Both simulations were tested as planar systems, and initially the pyramidal texturing for the downconverting film on cell configuration was not incorporated.

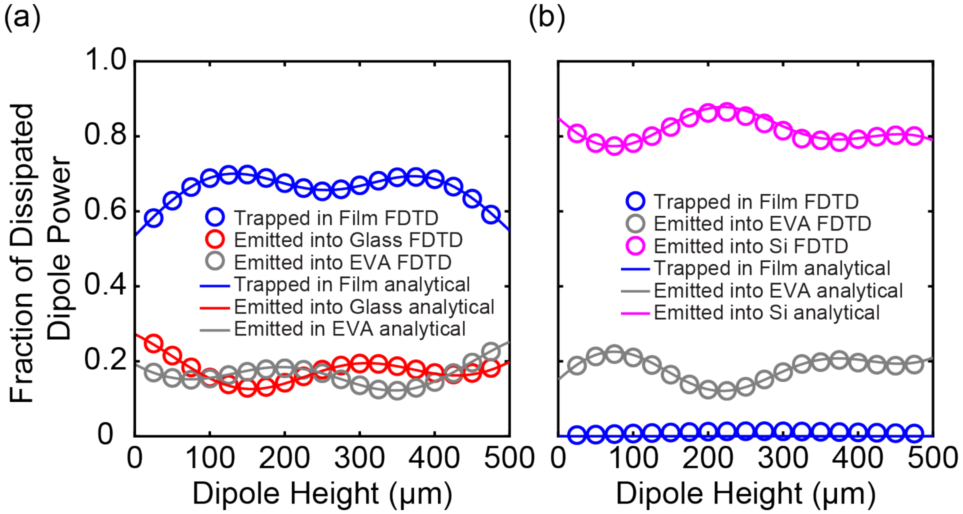

Figure 5.5: Fraction of emitted photons in the adjacent materials above and below the downconverting film for the (a) downconverting film on glass and (b) downconverting film on cell configurations. Simulated with FDTD simulations and analytical solver.

Figure 5.5 shows the fraction of dipole power that dissipates into each material as a function of changing dipole height within the downconverting film, for the film on glass and film on cell configurations. The FDTD simulations and analytical solver yielded nearly identical results, and the latter is more computationally efficient. As expected, the fraction of power dissipated into each material depends on the position of the dipole within the thickness of the film, with especially different coupling efficiency near the interfaces. The downconverting film on glass configuration shows significant light trapping within the downconverting film, which decreases light coupling into both the glass and EVA. This trapping is due to the higher refractive index of the downconverting film compared to both the glass and EVA. However, the downconverting film on cell configuration predicts high optical coupling into the SiN$_x$/Si, ranging between 0.78 and 0.9 depending on the dipole position. The high optical coupling derives from the high refractive indices of SiN$_x$ (n =. 1.98) and Si (n = 3.56) compared to the downconverting film (n = 1.97) at a wavelength of 1000 nm.

We then used the output of these calculations to estimate the optical coupling efficiency from the downconversion film to the Si absorber in the module, accounting for the pyramidal texturing, multiple reflections that occur within the module, and the PL bandwidth. For each dipole position (h), the angle-resolved power density per unit solid angle radiated into glass ($F_{rad}^{glass}(h, \theta_1, \lambda)$) and EVA ($F_{rad}^{EVA}(h, \theta_2, \lambda)$) from the simulations was used to analytically calculate the efficiency of different optical coupling modes in the system. A detailed description of the calculation method is provided in the Appendix. The coupling efficiency calculation for the downconverting film on glass and downconverting film on cell configuration was averaged over dipole height and weighted by the PL spectrum to give a single value.

Table 5.1 reports the coupling efficiency for the three configurations and four different conditions. The downconverting films were tested at four different thicknesses from 250 nm to 1000 nm, and the nanocomposite was analogously tested at four different nanocrystal loadings from 0.05 vol% to 0.3 vol%. The thicknesses and concentrations did not have a strong effect on the coupling efficiency, but the downconverting film location had a profound effect. The downconverting film on glass configuration had a coupling efficiency that ranged from 24.27% to 29.06%, whereas the downconverting film on cell configuration had a much higher coupling efficiency, between 93.37% and 95.25%. The downconverting nanocomposite had a high coupling efficiency of 81%. The lower index encapsulant layer (EVA) between the downconverter and the Si top interface was the main cause for the low coupling efficiency of the downconverting film on glass device, where the vast majority of downconverted light did not reach the Si absorber.

Table 5.1: Optical coupling efficiency for the downconverting film on glass and film on cell configurations with different downconverting film thicknesses, and for the nanocomposite configuration with different nanocrystal concentrations.

Coupling Efficiency (%)				
Film thickness	**t=250 nm**	**t=500 nm**	**t=750 nm**	**t=1000 nm**
Film on Glass	26.34%	24.27%	29.06%	25.65%
Film on Cell	93.65%	93.37%	93.47%	95.25%
NC concentration	**0.05 vol%**	**0.1 vol%**	**0.2 vol%**	**0.3 vol%**
nanocomposite	81.02%	81.03%	81.05%	81.06%

We note that the results in Table 5.1 contrast with coupling efficiency results previously reported by Kroupa, *et al.* in 2020 [114]. The most significant contrast is the downconverting film on glass coupling efficiency, which was previously reported at 72.0%. The discrepancies arise because in the previous studies, ray-tracing was used to model the angular distribution of dipole emission from the downconverting film, and the glass included texturing at the glass/EVA interface [114]. It is essential to model the angular distribution of the PL from the downconverting film using wave optics methods and not ray-tracing, as the downconverting film thickness is on the order of the wavelengths of light being considered. Modeling light interactions with structures of similar size to the wavelength of light using geometric optics principles can yield inaccurate and misleading results [121], which is why we believe the coupling efficiency estimates in Table 5.1 that combine nano- and macro-scale optics are an improvement on those estimated previously.

5.3.3 External Quantum Efficiency and Short Circuit Current Density

The full solar spectrum optical and electrical properties of the c-Si PERC cell were then evaluated using ray-tracing SunSolve simulations. The simulations were conducted for four different configurations: without any downconverting material in place, the downconverting film on glass configuration, the downconverting film on cell configuration, and the nanocomposite configuration. The simulations predict the module and cell absorption, reflection losses, and efficiency. The simulations do not include any enhancement in efficiency from the downconversion process, therefore the external quantum efficiency including the enhancement from downconversion PL was determined using the following equations:

$$\eta_{opt,DC,PL} = \frac{\int \eta_{opt,DC}(\lambda)\eta_{IQE}(\lambda)PL(\lambda)\,d\lambda}{\int PL(\lambda)\,d\lambda} \tag{5.3}$$

$$\eta_{EQE,DC} = A_{DC}(\lambda) * \eta_{PLQY} * \eta_{opt,DC,PL} + \eta_{EQE}(\lambda) \tag{5.4}$$

where $A_{DC}(\lambda)$ is the wavelength dependent downconverting material absorption probability, $\eta_{IQE}(\lambda)$ is the internal quantum efficiency of the Si cell, and $\eta_{EQE}(\lambda)$ is the external quantum efficiency extracted from the SunSolve simulations with the downconverting material included. $\eta_{opt,DC,PL}(\lambda)$ represents the probability that a photon emitted from the downconverting material will generate a charge carrier weighted by the PL spectrum. In equations 5.3 and 5.4, $\eta_{EQE}(\lambda)$, $\eta_{IQE}(\lambda)$, and $A_{DC}(\lambda)$ are from the SunSolve simulation results, and $\eta_{opt,DC}(\lambda)$ is from the optical coupling efficiency calculations. The $\eta_{EQE,DC}(\lambda)$ assuming a η_{PLQY} of 200% for each configuration is reported in Figure 5.6, and compared to a reference that does not contain any downconverting material.

The downconverting film on glass configuration reduced $\eta_{EQE,DC}(\lambda)$ across the entire spectrum compared to the reference cell. In the blue and UV portion of the spectrum, where we would expect enhanced efficiency from the downconversion process, this configuration instead reduces the $\eta_{EQE,DC}(\lambda)$, and changes in thickness do not improve these results. The oscillations seen in the $\eta_{EQE,DC}(\lambda)$ spectrum from 500 nm to 1000 nm in Figure 5.6a are from Fabry-Perot modes. The downconverting film on cell and nanocomposite configurations, however, exhibit significantly enhanced $\eta_{EQE,DC}(\lambda)$ across the absorption spectrum of the downconverting material that improved with increasing either the downconverting

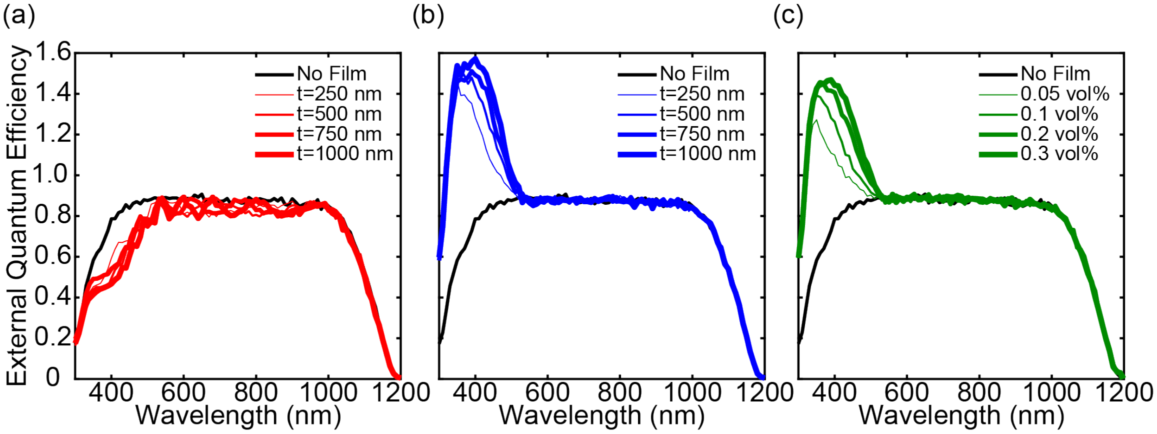

Figure 5.6: Estimated external quantum efficiency (EQE) of the PV modules with the downconverting materials for the (a) downconverting film on glass, (b) downconverting film on cell, and (c) nanocomposite configurations. The black trace represents the external quantum efficiency of the reference module without any downconverting materials.

film thickness or the concentration, which we attribute to increased absorption of incident sunlight. With a η_{PLQY} of 200% and high optical coupling efficiency, the $\eta_{EQE,DC}(\lambda)$ reached near 160% at its peak. Below the downconversion band gap, there was very little change in the $\eta_{EQE,DC}(\lambda)$ for 5.6b and c, indicating that the downconverting material did not significantly impact Si light absorption at longer wavelengths for the downconverting film on cell and nanocomposite configurations.

To understand the impact of the downconverting film position, thickness, and nanocrystal loading has on the J_{SC}, the change in J_{SC} was calculated using a similar approach as used by Kroupa, *et al.* [114]. The following equation was used:

$$\begin{aligned}\Delta J_{SC} = q\int_{300}^{1200} \phi_{AM1.5G}(\lambda)A_{DC}(\lambda)\eta_{PLQY}\eta_{opt,DC}\, d\lambda \\ -q\int_{300}^{1200} \phi_{AM1.5G}(\lambda)(A_{Cell}(\lambda) - A_{Cell,DC}(\lambda))\, d\lambda\end{aligned} \tag{5.5}$$

where $\phi_{AM1.5G}$ is the solar photon flux, q is the elementary charge, and $A_{Cell}(\lambda)$ and $A_{Cell,DC}(\lambda)$ are the absorption probabilities for the solar cell active layer without the downconverting material and with the downconverting material. The ΔJ_{SC} was added to the J_{SC}

extracted from the SunSolve simulations to yield an overall J_{SC} for the PV module containing downconverters.

The J_{SC} was calculated as a function of η_{PLQY} from 0 to 200% (Figure 5.7). The results are compared to the reference cell. As expected, at low η_{PLQY} no configuration resulted in enhanced J_{SC} as the increased parasitic absorption and internal reflection was not compensated by enhanced photocurrent. The downconverting film on glass configuration never achieved enhanced J_{SC} regardless of η_{PLQY}, and increasing the downconverting film thickness had a negative impact on the photocurrent. The other two configurations showed similar enhanced J_{SC} for values of η_{PLQY} above 100%. Below η_{PLQY}= 100%, a thicker downconverting film or higher nanocrystal concentration resulted in lower J_{SC} due to higher UV and blue light absorption that was not compensated by enhanced photocurrent, thus making the high energy absorption by the downconverting material parasitic. However, as the η_{PLQY} approached 200%, UV and blue light absorption was beneficial, with the downconverting film on cell device reaching 43 mA/cm^2 for the 1000 nm thick downconverting film.

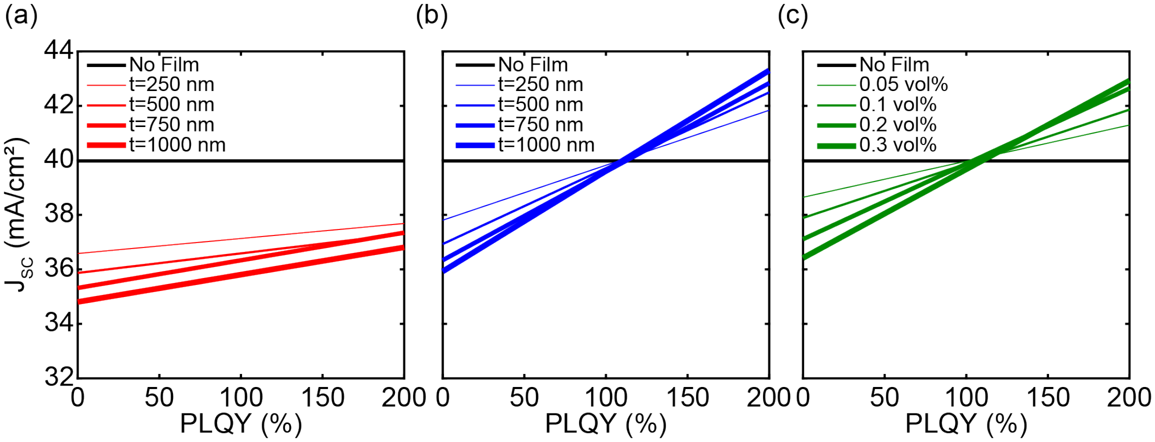

Figure 5.7: Short-circuit current density of the PV modules with the downconverting materials for the (a) downconverting film on glass, (b) downconverting film on cell, and (c) nanocomposite configurations. The horizontal black line represents the short-circuit current density of the reference module without any downconverting materials, which is 40 mA/cm^2.

The η_{PLQY} where the J_{SC} crosses the reference line has important implications for solar cell design. Both the downconverting film on cell and nanocomposite configuration require a η_{PLQY} greater than 100% to achieve the expected photocurrent enhancement. One might expect with high enough coupling efficiency and better spectral response at longer wavelengths there could be enhanced J_{SC} even at η_{PLQY} below 100%, but this is not the case. The photocurrent enhancement is primarily due to the photon multiplication from the downconversion and not spectral shifting to the NIR. The decrease in $\eta_{EQE}(\lambda)$ seen in the reference (Figure 5.6 a,b,c) as the wavelength approaches 300 nm is mostly due to parasitic glass and SiN_x absorption, not inefficiencies in photovoltaic conversion from high energy photons absorbed by the active layer. The downconversion material, therefore, will only enhance the efficiency through an overall increase in photon flux in the system, which is achieved with photon multiplication from η_{PLQY} greater than 100%.

The results in Figure 5.7 also suggest that high-efficiency c-Si PV systems that implement downshifting materials with 1:1 conversion will not be able to achieve increased J_{SC} and efficiency solely relying on improved spectral response. Even with high optical coupling efficiency, significant increases in J_{SC} were only achieved as the η_{PLQY} approached 200%. In the nanocomposite configuration, the downconverting composite refractive index is essentially the same as the encapsulant, and therefore has minimal change in internal reflection compared to the reference device. Since this case also requires a greater than 100% η_{PLQY} criteria to achieve enhanced photocurrent, this is not a result of index mismatch and increased reflection, and therefore would not change for lower refractive index films.

5.3.4 Optical Loss

The differences in optical performance between the three configurations can be further explained through wavelength dependent optical loss analysis (Figure 5.8). These results assumed a η_{PLQY} of 200%, downconverting film thickness of 500 nm, and a concentration of 0.1 vol% for the nanocomposite. The downconversion loss refers to photons absorbed by the downconverting material that did not result in photocurrent enhancement, and, since η_{PLQY} is 200%, high downconversion loss is a result of low coupling efficiencies. All light reflected off the top surface of the cell was accounted for in reflection loss, and escape losses refer to internal reflection and backscattering that ultimately escape the module. Other parasitic absorption includes other module and cell absorption losses.

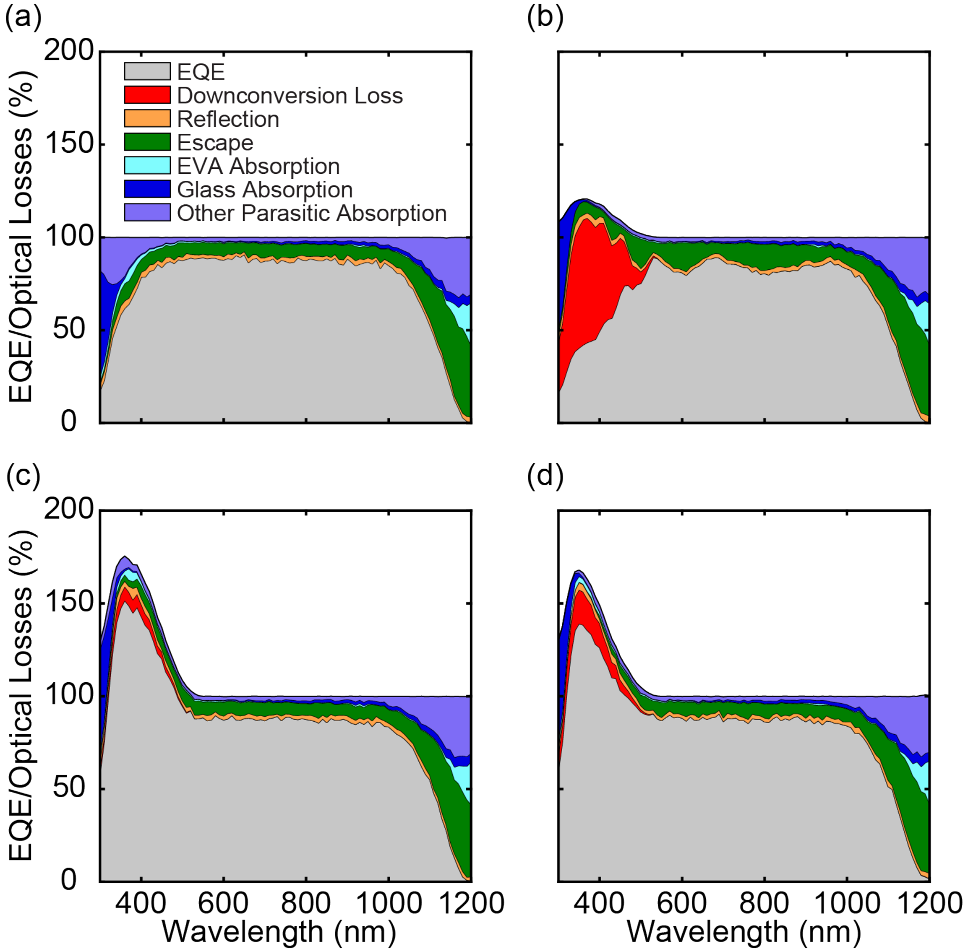

Figure 5.8: EQE and optical losses for the (a) reference cell, (b) the downconverting film on glass configuration, (c) the downconverting film on cell configuration, and (d) the nanocomposite configuration.

When analyzing the data for the downconverting film on glass case in Figure 5.8b, there were two loss mechanisms that prevented high $\eta_{EQE,DC}(\lambda)$: downconversion loss and escape. Most photons emitted from the downconverting material were lost to trapped modes or were lost out the top surface, which contributed to the downconversion loss. The internal reflection for this configuration was also higher and contributed to escape loss. The disruption of the index-matched glass/EVA interface increased internal reflection across the entire solar spectrum tested. The increased internal reflection combined with the high downconversion loss reduced the $\eta_{EQE,DC}(\lambda)$ and overpowered any photon multiplication or spectral shifting benefit from the downconverting material.

The downconverting film on cell and nanocomposite configurations showed minimal downconversion loss because of the high optical coupling efficiency, and the escape loss did not significantly increase when the downconverter was added. In the downconverting film on cell configuration, the downconverter is adjacent to a higher index material, SiN$_x$, and the pyramidal texturing helps reduce increased internal reflection. In the case of the composite, the nanocrystal loading does not increase the refractive index of the nanocomposite enough to significantly disrupt the index-matched glass/EVA interface and create internal reflection. We expect that if the composite exhibits significant scattering, escape losses would increase [71].

All configurations exhibited decreased $\eta_{EQE,DC}(\lambda)$ as the wavelength approached 300 nm due to the increase in parasitic glass absorption. The International Technology Roadmap for Photovoltaic (ITRPV) 2022 results show industry moving toward 2 mm glass thickness and predicts increased market share for glass thicknesses less than 2 mm over the next decade [62]. Decreased glass thicknesses will reduce the UV parasitic absorption and allow for greater downconverting absorption and photocurrent enhancement. The UV parasitic absorption from EVA is not as significant, as a UV transmissive EVA was chosen for this model [116]. We expect higher UV absorption from EVA would not affect the coupling efficiency estimates, but would decrease the downconversion absorption in the downconverting film on cell and nanocomposite configuration [114]. Polyolefin elastomer (POE) encapsulant materials are gaining popularity as an alternative to EVA [62], as they have improved UV transmission [122]. Improved encapsulant UV transmission would increase downconverting absorption and photocurrent enhancement, especially for the film on cell and nanocomposite configurations.

5.3.5 Downconversion Efficiency Enhancement

Finally, the solar cell power conversion efficiency (PCE) for each configuration was estimated based on the SunSolve simulation results and expected photocurrent enhancement from the downconversion process. The reference Si solar cell had a fill factor and open circuit voltage of 0.77 and 0.70 V. Neither of these terms changed significantly with the addition of the downconverting materials. The J_{SC} for the reference cell was 40.0 mA/cm^2, which made the estimated reference efficiency 20.6%. Using the enhanced J_{SC} reported in the Figure 5.6 for a η_{PLQY} of 200%, the power conversion efficiencies were calculated and reported in Table 5.2. Both the downconverting film on cell and nanocomposite configurations lead to enhanced efficiency, but none of the downconverting film on glass configurations exceed the reference efficiency. In general, higher absorption leads to increased efficiency enhancement, with the highest estimated efficiency at 22.4% for the 1000 nm thick downconverting film on cell device, which is a 2% absolute increase and 10% relative from the reference device. The 1000 nm thick downconverting film absorbs 62% of photons above the downconverting band gap, so this efficiency increase does not represent the upper limit. Thicker films were not explored, as we wanted to stay within a realistic range for perovskite conformal coatings on the pyramidal texturing using vapor deposition [53].

Table 5.2: Power conversion efficiency for the downconverting film on glass and film on cell configurations with different downconverting film thicknesses, and for the nanocomposite configuration with different nanocrystal concentrations.

	Efficiency (%)			
Film thickness	**t=250 nm**	**t=500 nm**	**t=750 nm**	**t=1000 nm**
Film on Glass	19.5%	19.3%	19.3%	19.1%
Film on Cell	21.7%	22.0%	22.2%	22.4%
NC concentration	**0.05 vol%**	**0.1 vol%**	**0.2 vol%**	**0.3 vol%**
nanocomposite	21.4%	21.7%	22.1%	22.2%

5.4 Conclusion

This study modeled three different configurations for downconverting materials applied to industry-relevant Si photovoltaic modules and estimated the optical coupling efficiency into the Si absorber, the optical losses, and efficiency metrics. Placing the downconverting film on the SiN_x with the pyramidal texturing resulted in the highest optical efficiency, ranging from 93-95$\%$, and the highest relative increase in PCE of 10$\%$ versus a module without a downconverting film. Putting the downconverting film in direct contact with the pyramidal texturing promoted high optical coupling from the downconverting film to the absorber and had minimal escape losses at longer wavelengths. Incorporating the downconverting film between the EVA and glass created a module that has very low optical coupling efficiency between the downconversion layer and cell due to trapped modes in the downconverting film and high escape losses from increased internal reflection. The downconverting film on glass configuration was not predicted to have enhanced photocurrent or efficiency compared to the reference device. Replacing the EVA with a downconverting nanocrystal-EVA nanocomposite yielded similar results to the downconverting film on cell configuration, where the optical coupling was sufficiently high and escape losses sufficiently low to exhibit enhanced power conversion efficiency.

The efficiency results in Table 5.2 are specific to PERC cells, but enhancing the efficiency with downconversion could also be applied to higher performance cells gaining market share such as Si heterojunctions (SHJ) and tunnel oxide passivated contact (TOPCon) solar cells [62]. Beyond Si, downconversion could be applied to CIGS solar cells to improve blue and UV response and increase J_{SC}, because CIGS has a similar band gap to Si [123].

The reduction in thermalization losses through the downconversion process may also help reduce operating temperatures. Thermalization of high energy photons and parasitic absorption increase module temperature, which reduces energy output and lifetime of solar cells [6,124]. Reducing waste heat generation through optical design is an effective method to reduce the operating temperature and increase energy yield [125–127]. In addition to the optical benefit discussed in the study, we believe the reduction of high energy photons incident on the active layer will reduce the waste heat generation, benefiting both energy yield and lifetime.

Based on the results of this paper, the optical design recommendation is to pursue either a nanocomposite downconverting material or deposit the downconverting film directly on the SiN_x. Importantly, this study predicts the enhancement is most effective when the η_{PLQY} is well above 100%, so high-quality downconverting materials are required given the performance level of industry standard c-Si solar cells. While this study is focused on quantum-cutting perovskite materials, the design recommendations and process for calculating the optical performance could be applied to other high-quality downconverting materials.

Chapter 6

Minimizing Roughness Induced Optical Losses for a Four-Terminal CdTe/Si Tandem Solar Cell

6.1 Introduction

The previous chapter focused on using spectral downconversion to improve the power conversion efficiency of solar cells, and how the placement of the downconverting material influences the optical coupling efficiency and efficiency metrics. This chapter discusses a different optical design method to enhance solar cell efficiency beyond single junction limits, tandem solar cells.

As single junction Si cells approach their performance limits, tandem architectures are becoming increasingly important in the drive for higher efficiencies [1, 128, 129]. Si is an advantageous choice for the bottom cell, given the technoeconomic benefits of the established Si photovoltaic industry [1, 130, 131]. Cadmium telluride (CdTe) is a promising candidate for the top subcell, as it is a proven material with high efficiency and long-term stability and can be mass produced for a low cost [60]. The band gaps of CdTe and Si are 1.5 and 1.12 eV, respectively, which allows near-infrared (NIR) light to transmit through the CdTe subcell and reach the Si subcell. To improve cell performance, CdTe is often alloyed with Se, which additionally makes the absorber band gap adjustable between approximately 1.38 eV (at approximately 40% Se) and 1.7 eV (pure CdSe). The combined benefits give CdTe/Si tandem cells advantages over other tandem systems like III-V/Si, which have high production costs [4], and perovskite/Si, which require improved stability and scalability [132]. For successful implementation, the tandem architecture must exceed the performance of the single junction device. Thus-far, CdTe solar cells epitaxially grown on Si cells have only yielded relatively low efficiencies of 17% [133]. On the other hand, high temperatures and aggressive chemistries involved in thin film CdTe device processing make direct deposition of these materials onto Si cells impractical [134–139].

Tamboli *et al.* predicted efficiencies in the range of 25%–30% if CdTe and silicon cells were electrically separated in the four-terminal mechanically stacked configuration schematically depicted in Figure 6.1 [60]. This configuration removes complexity from the tandem cell electrical design, as the direct series electrical connection of the cells, which is usually achieved through a tunneling junction, is not required. Electrically separating the subcells makes perfect current matching unnecessary, which is a major design constraint for the two-terminal monolithically integrated devices [140, 141]. In particular, Isah *et al.* [140] concluded that the maximum monolithic CdTe/Si tandem efficiency was obtained with a CdTe layer thinned down to 0.2 μm. Such thin absorbers tend to suffer from pinholes and shunting, more so when deposited on standard textured Si cells, making practical implementation of the design challenging [142]. Another disadvantage of the monolithic two-terminal tandem that is eliminated by the four-terminal mechanically stacked design is a strong sensitivity of the current generated by the bottom subcell to the incident solar spectrum. As a result, top and bottom subcell currents can be matched well for some climates and seasons, while the matching becomes suboptimal for other climates and seasons, resulting in energy yield losses [143].

The optical challenges introduced with four-terminal tandem devices, however, require strategic optical design and photon management to achieve high efficiencies. Photon management is essential in tandem devices to best utilize both semiconductor absorbers and achieve high efficiencies and is especially important in four-terminal tandem configurations. The strategic selection of conductive layer materials, surface texture for improved light coupling, and thickness optimization to control absorption and reflection become especially important with tandem devices to minimize reflection and parasitic absorption losses [140, 144, 145]. In the CdTe/Si four-terminal configuration, sub-band-gap light not absorbed by the CdTe cell must be transmitted through the transparent front and back contacts of the CdTe layer, the encapsulant, and the top of the Si cell before it can be converted into electricity by the Si cell.

Achieving high transmission values therefore requires the use of both transparent back electrodes and understanding of the impact of surface roughness on light transmission. Previous studies on CdTe devices with transparent back contacts were successful at improving the NIR transmittance to about 70% [137, 146, 147], using relatively flat CdTe topography. The CdTe film preparation technique impacts on the surface topography and microstructure. Common CdTe film deposition techniques for photovoltaics include vapor transport deposition (VTD), thermal evaporation, close-space sublimation (CSS), and magnetron sputtering [134–137, 147–154]. Among the techniques most suitable for industrial applications, VTD and CSS, VTD has key advantages, including high rates, low cost, smaller source areas, and decoupled substrate and source environments [134, 136, 148, 150, 151]. VTD produces high-quality polycrystalline CdTe films, and the grain size can be controlled by tuning the substrate temperature [151]. The impact of treatments such as $CdCl_2$ and heat on the electrical properties of CdTe cells is also well studied; these treatments lead to morphological changes, such as increased grain size and surface roughness, that affect NIR transparency [138, 139, 154–158].

However, the importance of surface roughness in the four-terminal device configuration, and the interaction between the surface texture and transparent electrodes, is not well characterized or understood. Here, we use a combination of simulations and experiments to understand and reduce roughness induced transparency losses in a CdTe/Si four-terminal device, with special attention paid to surface texture induced absorption enhancement in the transparent back contact. We also offer strategies to mitigate these losses through high index optical coatings and planarization.

6.2 Methods

6.2.1 Solar Cell Samples

The CdSe$_x$Te$_{1-x}$ solar cell samples were provided by First Solar.

6.2.2 Surface Roughness Characterization

Contact mode AFM measurements were performed with a Bruker Dimension ICON atomic force microscope on the back surface of a completed CdSe$_x$Te$_{1-x}$ solar cell without EVA encapsulation. The total scan area is 15 x 15 µm^2.

6.2.3 UV/vis Spectrophotometry

Total transmission measurements were performed using a Cary 7000 UV-vis spectrophotometer with a diffuse reflectance accessory. During the measurement, the CdSe$_x$Te$_{1-x}$ solar cell was mounted on the integrating sphere transmission port and polytetrafluoroethylene reflectance standards blocks the back port.

6.2.4 Finite-Difference Time-Domain Simulations

The simulated CdSe$_x$Te$_{1-x}$ solar cell consisted of a 330-nm-thick front TCO on a glass substrate, a 3.3-µm-thick CdSe$_x$Te$_{1-x}$ layer, and a 150-nm-thick back TCO. The front and back transparent TCO contacts were multilayer stacks with additional layer thicknesses between 10 and 40 nm thick. A 35-nm-thick ZnTe layer served as a p contact on top of the graded CdSe$_x$Te$_{1-x}$ absorber. Surface roughness data from the AFM measurements were applied to the CdSe$_x$Te$_{1-x}$ layer and all layers in the transparent back contact. A simulation area of 10 x 10 μm^2 with periodic boundary conditions was found to be sufficiently large to capture the surface roughness.

The optical simulations were conducted by injecting a plane wave into the CdSe$_x$Te$_{1-x}$ solar cell, starting with the glass layer. A monitor in the air gap or EVA interlayer was used to collect the transmittance through the device stack, and 3D electric field monitors placed around the entire device were used to calculate absorption. When comparing the simulated transmission to experimental measurements, reflection loss off the air-glass interface and absorption loss through the 2.65-mm-thick glass substrate were added to the simulation results in postprocessing. The reflection at normal incidence was estimated with Fresnel equations and is about 4%, and the glass absorption estimated with Beer's law is about 2%.

6.3 Results and Discussion

6.3.1 CdSe$_x$Te$_{1-x}$ Cell Structure and Properties

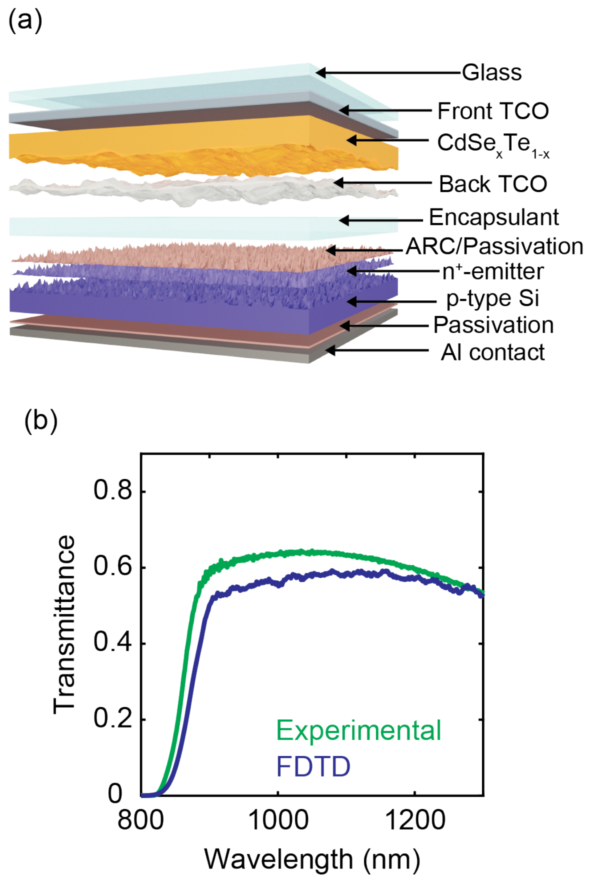

Figure 6.1: (a) Illustration of a CdTe/Si four-terminal tandem solar cell (ARC is anti-reflection coating). (b) CdTe solar cell experimental and simulated transmittance.

Figure 6.1a shows our assumed device configuration. The CdTe cell is assumed to have a planar front transparent conductive oxide (TCO); the absorber layer is comprised of VTD deposited $CdSe_xTe_{1-x}$, with surface roughness on the back interface; and a conformally grown back metal oxide based TCO is included as a rear conductive layer. In the full tandem configuration, this is followed by an encapsulant layer (EVA) and a typical Si cell underneath. The refractive index of each layer is shown in Figure 6.2.

$CdSe_xTe_{1-x}$ solar cell samples were received from First Solar Inc. without EVA encap-

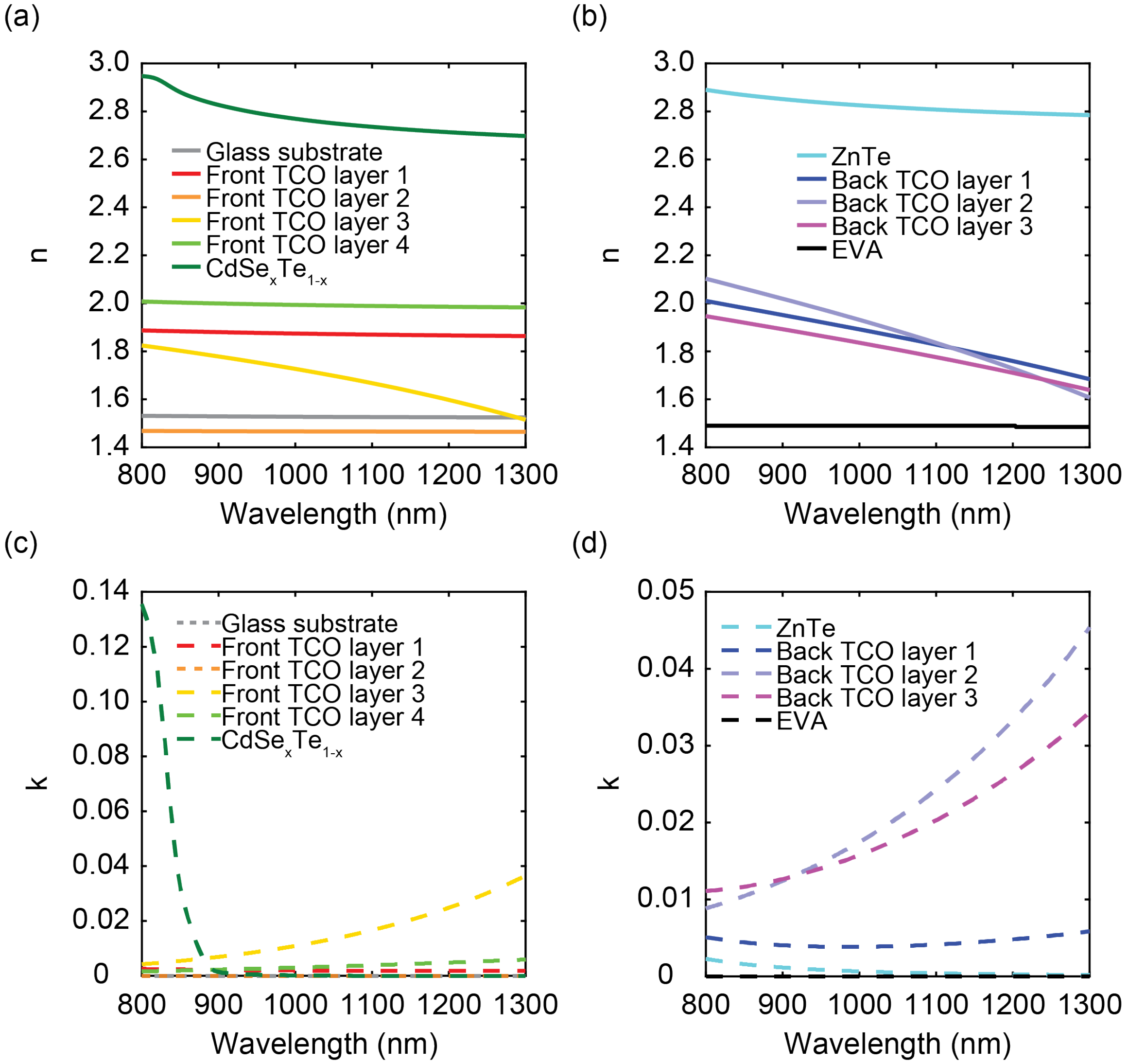

Figure 6.2: (a-b) Real and (c-d) imaginary refractive index of materials used in the $CdSe_xTe_{1-x}$ solar cell simulations

sulation. The total sub-bandgap transmittance was measured by UV-vis spectrophotometry and plotted in Figure 6.1b. Finite-difference time-domain (FDTD) simulations were used to analyze the sub-band-gap transmittance of the CdSe$_x$Te$_{1-x}$ top cell in the proposed CdSe$_x$Te$_{1-x}$/Si four-terminal tandem configuration. The surface roughness of the CdSe$_x$Te$_{1-x}$ layer was measured by atomic force microscopy (AFM) and imported directly into the FDTD simulations. Figure 6.1b compares the experimentally measured and modeled sub-band-gap transmittance through the top cell. The simulation and experiment show reasonable agreement, with the FDTD simulation underestimating the sub-band-gap transmittance. Some discrepancies are seen in the location of the transmission onset and shape of the transmittance. These are hypothesized to be due to a simplification of the refractive index of the CdSe$_x$Te$_{1-x}$ in the model, which does not account for the graded CdSe doping at the front interface of the CdSe$_x$Te$_{1-x}$ absorber layer.

We compare three different roughness cases: one with native texture, a planar surface, and an intermediate case obtained by scaling the surface height of the as deposited texture by 0.5. The transmittance from the simulations without the EVA interlayer is shown in Figure 6.3a. The transmittance spectrum of the planar device supports Fabry-Perot modes that closely match transfer-matrix method predictions. The rough surface has the least transmission, but reducing the roughness of the CdSe$_x$Te$_{1-x}$ surface results in significant increases to transmittance. However, the proposed four-terminal CdSe$_x$Te$_{1-x}$/Si tandem cell has an EVA encapsulant interlayer instead of an air gap, so we additionally performed calculations of transmittance into EVA (Figure 6.3b). The two rough samples now show significantly greater transmittance, and the differences in transmittance between the samples is less dramatic, indicating that the roughness driven transmission decreases are mitigated via the inclusion of the EVA layer.

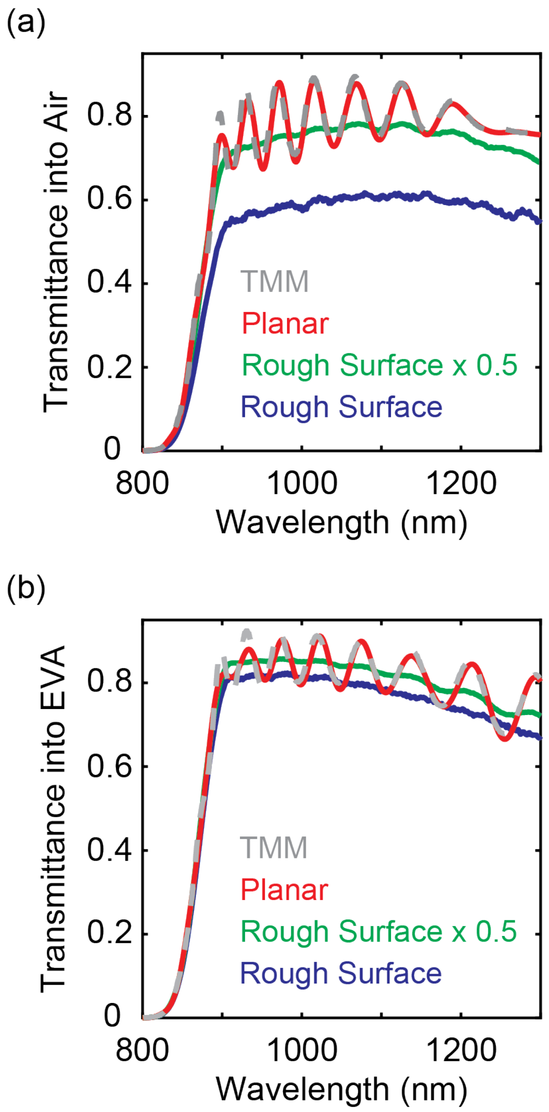

Figure 6.3: CdTe solar cell transmittance into (a) air and (b) EVA.

6.3.2 Transparency Losses

To understand the transparency losses, we calculated the wavelength dependent absorption and reflection for the three $\mathrm{CdSe}_x\mathrm{Te}_{1-x}$ devices with and without the EVA (Figure 6.4). The power absorbed was calculated according to Equation 6.1, where ϵ” is the imaginary part of the complex permittivity, and $|E|^2$ is the intensity of the electric field:

$$P_{abs} = -0.5\omega|E|^2\epsilon'' \tag{6.1}$$

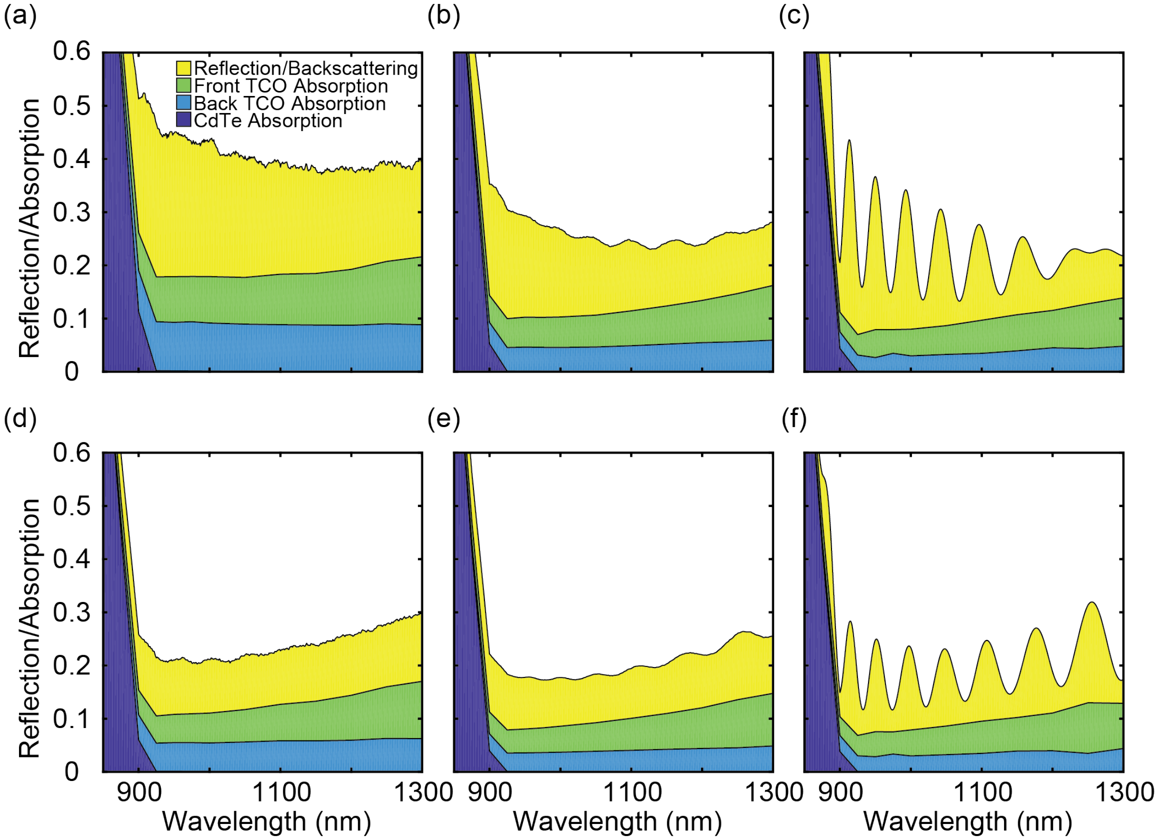

Figure 6.4: Dominant optical loss mechanisms preventing sub-band-gap CdSe$_x$Te$_{1-x}$ cell transmission into (a)-(c) air or (d)-(f) EVA for samples with (a),(d) a rough surface; (b),(e) a rough surface x 0.5; and (c),(f) a planar surface.

These calculations were performed for the entire three-dimensional (3D) simulation and the power absorbed in each material was isolated, as described in Section 6.2. The front contact of silicon was not included in these simulations, as the focus was on increasing transparency into EVA or air before the light reaches the silicon cell.

At wavelengths longer than the CdSe$_x$Te$_{1-x}$ band gap, the dominant loss mechanisms are reflection, scattering, and absorption from the front and back TCOs. For all samples, both the reflection and TCO absorption decrease with the inclusion of the EVA interlayer, and the decrease is most significant for the samples with higher roughness. The reduced index contrast between the back TCO and EVA compared to the TCO-air interface reduces both specular reflection and backscattering, and therefore, also front TCO absorption. Planarization of the surface texture decreases both reflection and TCO absorption. Decreasing the CdSe$_x$Te$_{1-x}$ surface roughness reduces the total reflection because there is less backscattering at the back TCO interface. The increased backscattering from the rough back TCO also leads to increased front TCO absorption, because more light is trapped in the CdSe$_x$Te$_{1-x}$ cell similar to the roughness induced light trapping utilized in silicon solar cells [159–161].

6.3.3 Light Localization and Absorption in the back TCO

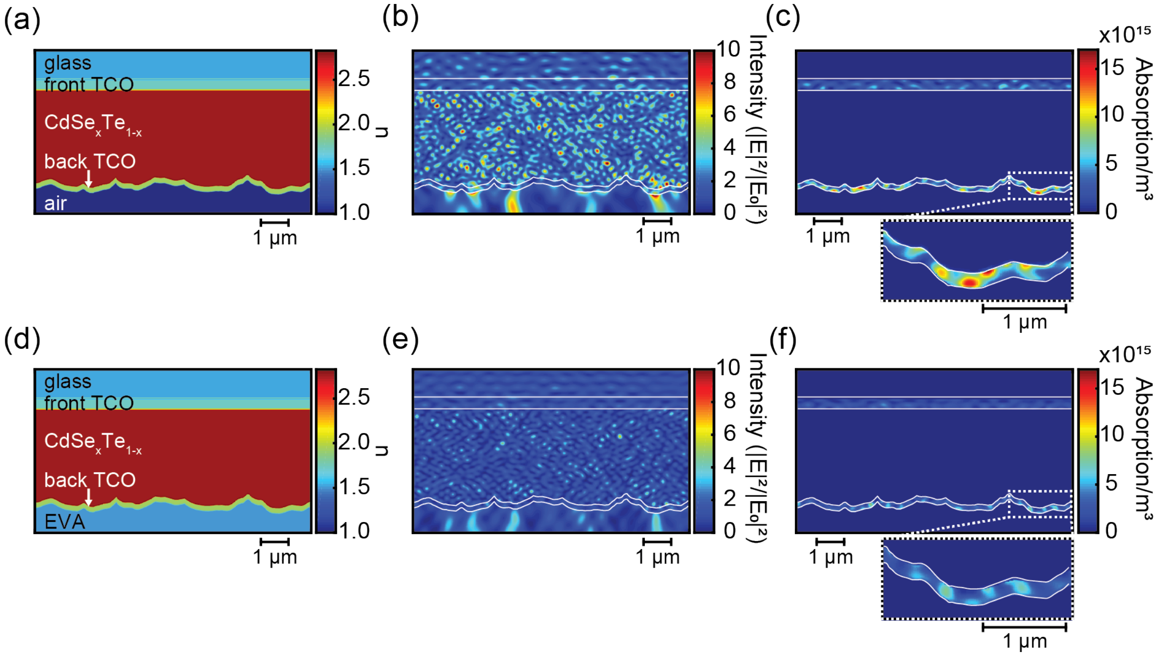

Figure 6.5: (a),(d) Cross section of the real component of the refractive index; (b),(e) electric field intensity enhancement; and power absorption in the CdTe solar cell with (a)-(c) air and (d)-(f) EVA. White lines are included in (b) (c),(e),(f) at material interfaces.

To understand the roughness induced absorption enhancement in the back TCO, Figure 6.5 shows a vertical cross section of the electric field intensity and absorption at a wavelength of 1 µm. As expected, absorption losses are confined to the front and back TCOs. However, the magnitude of the absorption losses varies significantly with surface texture and inclusion of the EVA interlayer. The electric field intensity figures show electric field intensity localization surrounding the peaks of mesoscale (1–3 µm) features on the rough CdSe$_x$Te$_{1-x}$ surface. These intense electric field concentrations are accompanied by pho-

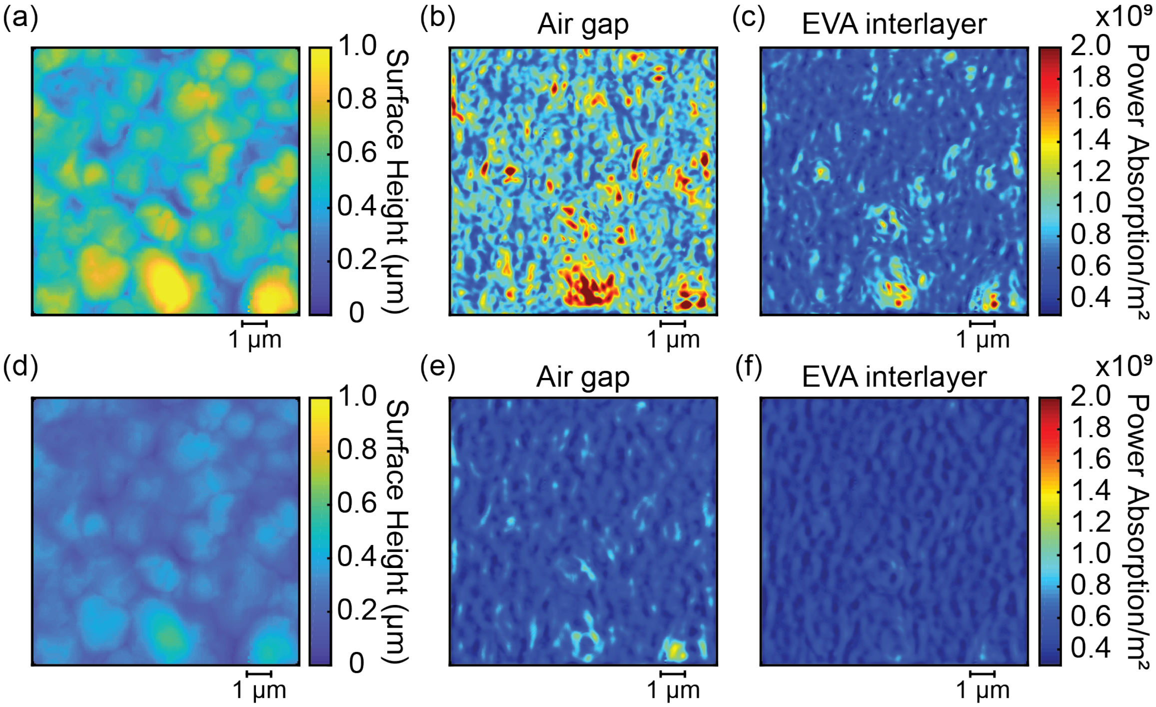

Figure 6.6: Surface height profiles and position resolved back TCO power absorption for $CdSe_xTe_{1-x}$ *solar cells with (a)-(c) the rough surface (d)-(f) and the rough surface x0.5. Back TCO power absorption is shown for cells with both (b),(e) air and (c),(f) EVA.*

ton jets that extend into the air-EVA interface. Significant interference patterns throughout the cell are due to the superposition of the incoming, reflected, and scattered plane waves.

To visualize the electric field localization and absorption enhancement in the back TCO from a different perspective, we integrated the power absorption over the thickness of the conformal back TCO, averaged the results from 950 to 1300 nm weighted by the AM1.5 global solar spectrum, and plotted the lateral 2D projections in Figure 6.6. It is important to recognize that the back TCO thickness remained constant at 150 nm, regardless of surface height. Comparing these calculations to the surface height maps shows that the surface morphology influences the local power absorption in the back TCO: the locations with greatest power absorption are regions of high surface height. At the apex of a mesoscale morphological feature, there is a region of electric field intensity localization and enhanced power absorption. Similar features are seen in the sample with reduced surface roughness, but with decreased magnitude of absorbed power, due to the decreased feature height.

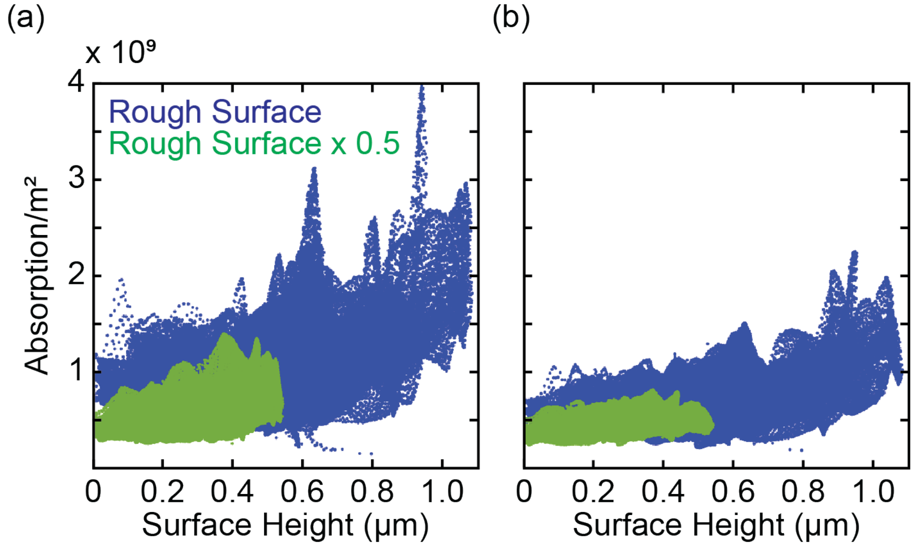

Figure 6.7: Local back TCO absorption plotted over the surface height at every location interfacing with (a) iar and (b) EVA interlayer.

The data in Figure 6.6 was also plotted in Figure 6.7 as scatter plots against surface height to help describe the relationship between the localized power absorption enhancements and surface height. It is not a monotonic trend, but as the surface height increases the power absorption maximum at that surface height also increases. The maximum power absorption obtained at each surface height increases less dramatically with the inclusion of the EVA. This reinforces that the light localization phenomenon is not eliminated by decreasing the index contrast, but the magnitude is reduced.

We attribute the electric field intensity localization and absorption enhancement to a focusing effect dominated by the mesoscale features on the $\mathrm{CdSe}_x\mathrm{Te}_{1-x}$ surface. It is similar to the nonresonant effect seen in previous studies on dielectric particles and gratings, where light is localized near the forward direction surface of the dielectric material [162–170]. The focusing effect is a function of feature size and shape, aspect ratio, index contrast, and wavelength of light. In our case, the average size of the curved surface features is approximately 0.97 μm, which is similar in length to the wavelength range of interest. The reflection and scattering of the injected plane wave off these curved surfaces cause constructive interference that focuses and localizes light around the apex of the surface features. These features are not perfectly optimized to focus the incoming light, but the collective local absorption enhancement leads to a global increase in back TCO absorption by about 141% for the samples that interface with air and about 65% for samples with the EVA interlayer.

The EVA interlayer reduces the magnitude of the back TCO absorption enhancement (and increases transmission) because it reduces the index contrast at the rough surface. Previous studies on dielectric spheres and particles demonstrate that a reduced index contrast shifts the point of focus forward into the lower index medium and creates more forward scattering [163, 164, 167, 168, 170]. Similarly, the EVA interlayer enhances forward scattering and decreases lateral scattering, which diminishes the localized absorption enhancement in the back TCO.

6.3.4 High Index Optical Coatings and Tandem Efficiency

This posed the question as to whether further reductions in index contrast could provide even greater enhancement to CdSe$_x$Te$_{1-x}$ cell transmittance. To investigate this, two lossless constant refractive index optical coatings were investigated with slightly different functionalities. First, an n = 1.7 optical coating was considered to provide a smaller stepwise transition in refractive index from the back TCO to the EVA interlayer. The second optical coating considered has a larger refractive index of n = 1.9, which index matches the back TCO at a wavelength of 1 μm.

The effects of including high index optical coatings on the transmittance of a CdSe$_x$Te$_{1-x}$ cell are summarized in Figure 6.8. The transmittance of the solar cell with only EVA is also included as a reference. Semi-infinitely thick optical coatings are first considered to view the effects the coatings have on the unpolished cell's sub-band-gap transmittance without the additional coating-EVA interface. As anticipated, the reduced index contrast results in increases in transmittance beyond devices with the EVA interlayer. The cells with the n = 1.9 optical coating have a larger transmittance than those with the n = 1.7 coating at shorter wavelengths, but their transmittance is comparable at wavelengths greater than 1050 nm

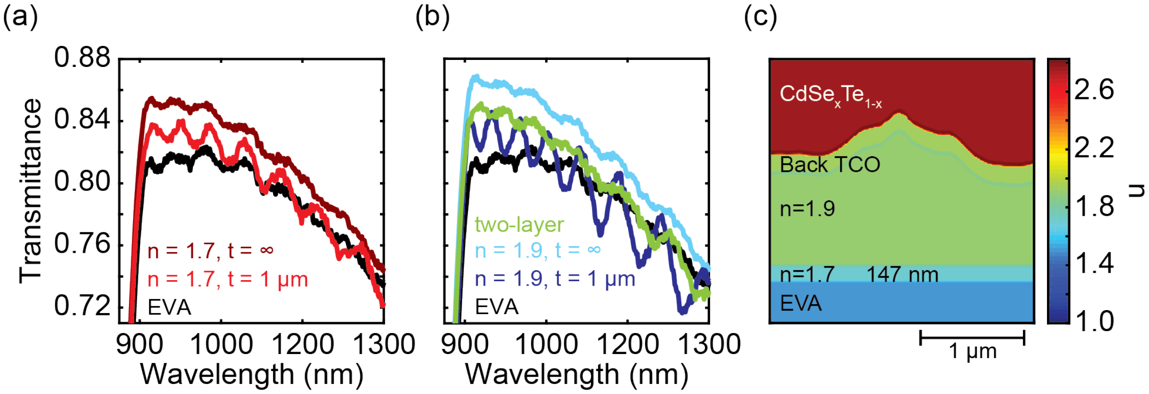

Figure 6.8: CdSe$_x$Te$_{1-x}$ cell transmittance from FDTD simulations for (a) the n=1.7 coatings and (b) the n = 1.9 coating and the two-layer coating. (c) Cross section of the refractive index for the two-layer coating.

due to dispersion in the refractive index of the back TCO, which disrupts the index matching condition of the n = 1.9 coating. These results indicate that substitution of the EVA interlayer with a higher refractive index alternative, such as the high refractive index polymers often used to encapsulate light-emitting diodes [47-50] [171–174], could be used to further enhance the optical coupling in CdTe/Si four-terminal tandem cells.

The effects of the additional coating-EVA interface are also simulated with 1-μm-thick optical coatings. The coatings are assumed to optically “flatten” the back contact by forming a planar interface with the EVA interlayer. Unfortunately, the transmittance for the devices is reduced due to reflection at the coating-EVA interface. The device with the n = 1.9 coating has the largest reduction in transmittance, decreasing below the CdSe$_x$Te$_{1-x}$ device without an optical coating at longer wavelengths due to its high refractive index contrast with the EVA interlayer. The CdSe$_x$Te$_{1-x}$ cell with an n = 1.7 coating displays a smaller reduction in transmittance and still outperforms the cell without a high index coating at most wavelengths due to its smaller stepwise transitions in refractive index.

The reflection losses at the coating-EVA interface can be significantly reduced by applying an additional coating to serve as an antireflection coating between the two layers. The proposed two-layer optical coating is schematically depicted in Figure 6.8c, consisting of a 1-μm-thick n = 1.9 coating to planarize the back contact followed by a n = 1.7 coating, the thickness of which, 147 nm, is selected to serve as a quarter-wave layer. The two-layer optical coating outperforms devices with single-layer coatings at short wavelengths. However, dispersion in the back TCO's refractive index causes poor index matching between the n = 1.9 optical coating and back TCO at long wavelengths, causing the two-layer coating device's transmittance to fall below the cell with only an EVA interlayer at wavelengths longer than 1100 nm.

After demonstrating improved transmittance through the CdSe$_x$Te$_{1-x}$ cell, we estimated the performance of the Si cell implemented as the bottom subcell. For this estimate, we assumed an industrial p-type mono-PERC silicon cell with an efficiency of 22%. The external quantum efficiency (η_{EQE}) is sourced from the literature [44]. The short circuit current density (J_{SC}) of the Si cell was calculated by

$$J_{SC} = q \int \eta_{EQE}(\lambda) x T(\lambda) x \Phi_s(\lambda)/, d\lambda \tag{6.2}$$

where T is the CdSe$_x$Te$_{1-x}$ solar cell's transmittance, Φ_s is the spectral solar photon flux, and q is the elementary charge. Equation 6.2 is integrated across the entire AM1.5G solar spectrum, and the results are displayed in Table 6.1.

The J_{SC} for the Si cell under an unfiltered solar spectrum was estimated to be 40.9 mA/cm^2. The open circuit voltage, fill factor, and efficiency of the silicon cell under the CdSe$_x$Te$_{1-x}$ device can then be calculated according to methods described in the Appendix. The efficiency estimates assumed that differences in surface roughness are only influencing the optical properties. Surface texture and other defects like lattice distortions, impurities, and dislocations can impact the material properties, electrical performance, and solar cell efficiency [175–179]. However, isolating the influence of the texture on optics alone allows us to make meaningful performance comparisons between the planarized samples and the high index optical coatings.

Both strategies increase the efficiency of the bottom Si cell. Planarizing the back contact interface results in an increase of 1.1% in silicon cell efficiency with no EVA interlayer, and

Table 6.1: Short circuit current density and efficiency of the monosilicon passivated emitted and rear contact (PERC) solar cell (η_{Si}) under different CdSe$_x$Te$_{1-x}$ solar cell samples and interlayers. The estimated tandem cell efficiency is also included (η_T).

Sample	J_{SC}(mA/cm^2)	η_{Si}(%)	η_T (%)
Rough surface air	5.7	3.0	25.0
Rough surface x0.5 air	7.4	4.0	36.0
Planar air	7.7	4.1	26.1
Rough surface EVA	8.0	4.3	26.3
Rough surface x0.5 EVA	8.4	4.5	26.5
Planar EVA	8.4	4.5	26.5
Two-layer	8.2	4.4	26.4

a 0.2% increase with the interlayer included. Applying the two-layer high index optical coating also results in a slight increase in efficiency for the cell compared to the cell with only EVA. We note that these Si cell efficiencies are similar to those predicted by Tamboli *et al.*, and when combined with the CdTe cell efficiency of 22% would exceed a single junction efficiency up to 26.5% [60, 180].

6.4 Conclusion

CdTe/Si four-terminal tandem solar cells are promising architectures that take advantage of the two most dominant single junction technologies on the market. This study characterizes the sub-band-gap transparency losses in the CdSe$_x$Te$_{1-x}$ top cell and investigates two methods to increase top cell transmittance: reducing the roughness and including high index interlayers. The loss in the back TCO is increased by mesoscale features on the CdSe$_x$Te$_{1-x}$ surface that create a focusing effect and localized absorption enhancement. Since this effect is related to both the height of the surface features and the index contrast, either planarization of the surface texture or the inclusion of higher index optical coatings mitigates the roughness induced optical losses and promote transmittance. A two-layer coating provides a 2%-3% increase in transmittance from 900 to 1000 nm compared to EVA alone.

Chapter 7

Summary and Outlook

Light management in Si solar cells is becoming increasingly important as the PV industry continues to rapidly expand. Optimal utilization of blue and UV light through downshifting, downconversion, and tandem solar cells and methods to mitigate optical loss discussed in this thesis can increase Si cell efficiencies and expand available installation sites.

In Chapter 2, we used analytical modeling to identify identify luminophore selection criteria that enhanced the efficiency and visible spectral quality of tandem LSCs. Luminophores that have high photoluminescence quantum yield, low overlap between absorption and photoluminescence spectra, and band gaps closely matched to the band gap of the luminophore were found to perform the best.

Chapters 3 and 4 investigated methods to improve and optimize LSCs for agrivoltaic applications. Bilayer LSCs combining CdSe/CdS and Si nanocrystals had enhanced absorption, efficiency, and transmission tunability. A needle insertion method was used to design thin-film stacks for LSCs that increased transmission and extraction efficiency depending on the merit function used. Recent studies investigated integrating LSCs into greenhouses and found that the electricity generation from the LSCs can help offset greenhouse energy demands, and the LSCs can provide shading during summer months to help keep the greenhouse cooler [181]. Combining methods to manipulate the extraction efficiency of LSCs to increase red light incident on the plants with the greenhouse system analysis would be beneficial to understand economic and thermal benefits of LSCs with directional emission.

Surface texturing to promote outcoupling should also be explored further as a method to control the filtered transmission spectrum and diffuse transmission [111].

Chapter 5 combined wave optics and geometric optics to model downconverting films and nanocomposites in a c-Si PERC module. We demonstrated that the downconverting film on cell configuration and the nanocomposite configuration had the highest optical coupling efficiency without disrupting internal reflection, and the greatest relative increase in power conversion efficiency was 10%. Investigating downconversion films for other state of the art Si cells like SHJ and TOPCon cells would also be useful to determine how the efficiency enhancement influences higher efficiency cells. Further consideration to the texturing at the glass/encapsulant interface would also be beneficial.

We discussed $\mathrm{CdSe}_x\mathrm{Te}_{1-x}$/Si tandem solar cells in Chapter 6 and analyzed sub-band gap transmission losses through the $\mathrm{CdSe}_x\mathrm{Te}_{1-x}$ sub-cells using UV/Vis spectrophotometry, AFM measurements, and FDTD simulations. The study revealed that a focusing effect from mesoscale sized surface features on the $\mathrm{CdSe}_x\mathrm{Te}_{1-x}$ increased the total reflection and contact absorption. High index optical coatings were found to mitigate the optical losses, increase transmission, and enhance the tandem cell efficiency by a relative increase of 5.6%. In addition to high-index optical coatings and reducing the roughness, the near-field focusing effect could also be mitigated by controlling the $\mathrm{CdSe}_x\mathrm{Te}_{1-x}$ grain size and surface feature size. Further research into the connection between $\mathrm{CdSe}_x\mathrm{Te}_{1-x}$ grain size and back contact absorption would help to further develop this technology.

The methods to more efficiently utilize blue and UV light described in this thesis will help enhance the c-Si photovoltaic efficiency beyond the Shockley-Queisser limit and advance transparent photovoltaic technologies. The optical loss analysis and waveguide design developed for LSCs contributes to agrivoltaic research and moves the field further toward LSCs with optimal multifunctional properties. Optical design of downconversion photovoltaics will help guide fabrication and experimental efforts to achieve the enhanced photocurrents predicted by simulations. The optical loss mitigation methods will help increase $\text{CdSe}_x\text{Te}_{1-x}$/Si tandem solar cell efficiency to be competitive with other state of the art tandem cells.

Bibliography

[1] G. M. Wilson, M. Al-Jassim, W. K. Metzger, S. W. Glunz, P. Verlinden, G. Xiong, L. M. Mansfield, B. J. Stanbery, K. Zhu, Y. Yan, J. J. Berry, A. J. Ptak, F. Dimroth, B. M. Kayes, A. C. Tamboli, R. Peibst, K. Catchpole, M. O. Reese, C. S. Klinga, P. Denholm, M. Morjaria, M. G. Deceglie, J. M. Freeman, M. A. Mikofski, D. C. Jordan, G. TamizhMani, and D. B. Sulas-Kern, "The 2020 photovoltaic technologies roadmap," Journal of Physics D: Applied Physics **53**, 493001 (2020).

[2] D. Feldman, K. Dummit, J. Zuboy, J. Heeter, K. Xu, and R. Margolis, "Spring 2022 Solar Industry Update," Tech. Rep. NREL/PR-7A40-82854, National Renewable Energy Lab. (NREL), Golden, CO (United States) (2022).

[3] "Solar PV – Analysis," https://www.iea.org/reports/solar-pv.

[4] W. Shockley and H. J. Queisser, "Detailed Balance Limit of Efficiency of p-n Junction Solar Cells," Journal of Applied Physics **32**, 510–519 (1961).

[5] "Electric Power Monthly - U.S. Energy Information Administration (EIA)," https://www.eia.gov/electricity/monthly/epm_table_grapher.php.

[6] J. A. Nelson, *The Physics Of Solar Cells* (World Scientific Publishing Company, 2003).

[7] T. Trupke, M. A. Green, and P. Würfel, "Improving solar cell efficiencies by down-conversion of high-energy photons," Journal of Applied Physics **92**, 1668–1674 (2002).

[8] V. Badescu and A. D. Vos, "Influence of some design parameters on the efficiency of solar cells with down-conversion and down shifting of high-energy photons," Journal of Applied Physics **102**, 073102 (2007).

[9] R. Brendel, J. H. Werner, and H. J. Queisser, "Thermodynamic efficiency limits for semiconductor solar cells with carrier multiplication," Solar Energy Materials and Solar Cells **41–42**, 419–425 (1996).

[10] M. B. de la Mora, O. Amelines-Sarria, B. M. Monroy, C. D. Hernández-Pérez, and J. E. Lugo, "Materials for downconversion in solar cells: Perspectives and challenges," Solar Energy Materials and Solar Cells **165**, 59–71 (2017).

[11] R. T. Wegh, H. Donker, E. V. D. van Loef, K. D. Oskam, and A. Meijerink, "Quantum cutting through downconversion in rare-earth compounds," Journal of Luminescence **87–89**, 1017–1019 (2000).

[12] T. J. Milstein, D. M. Kroupa, and D. R. Gamelin, "Picosecond Quantum Cutting Generates Photoluminescence Quantum Yields Over 100% in Ytterbium-Doped CsPbCl3 Nanocrystals," Nano Letters **18**, 3792–3799 (2018).

[13] D. M. Kroupa, J. Y. Roh, T. J. Milstein, S. E. Creutz, and D. R. Gamelin, "Quantum-Cutting Ytterbium-Doped CsPb(Cl1–xBrx)3 Perovskite Thin Films with Photoluminescence Quantum Yields over 190%," ACS Energy Letters **3**, 2390–2395 (2018).

[14] E. Yablonovitch, "Thermodynamics of the fluorescent planar concentrator," JOSA **70**, 1362–1363 (1980).

[15] I. Papakonstantinou, M. Portnoi, and M. G. Debije, "The Hidden Potential of Luminescent Solar Concentrators," Advanced Energy Materials **11**, 2002883 (2021).

[16] "KAUST team sets world record for tandem solar cell efficiency," https://www.kaust.edu.sa/news/kaust-team-sets-world-record-for-tandem-solar-cell-efficiency.

[17] M. A. Green, E. D. Dunlop, G. Siefer, M. Yoshita, N. Kopidakis, K. Bothe, and X. Hao, "Solar cell efficiency tables (Version 61)," Progress in Photovoltaics: Research and Applications **31**, 3–16 (2023).

[18] A. Smets, K. Jäger, O. Isabella, R. van Swaaij, and M. Zeman, *Solar Energy: The Physics and Engineering of Photovoltaic Conversion, Technologies and Systems* (Bloomsbury Publishing, 2016).

[19] S. Rühle, "Tabulated values of the Shockley–Queisser limit for single junction solar cells," Solar Energy **130**, 139–147 (2016).

[20] A. M. Smith and S. Nie, "Semiconductor Nanocrystals: Structure, Properties, and Band Gap Engineering," Accounts of Chemical Research **43**, 190–200 (2010).

[21] A. S. Sadhu, Y.-M. Huang, L.-Y. Chen, H.-C. Kuo, and C.-C. Lin, "Recent Advances in Colloidal Quantum Dots or Perovskite Quantum Dots as a Luminescent Downshifting Layer Embedded on Solar Cells," Nanomaterials **12**, 985 (2022).

[22] A. P. Alivisatos, "Semiconductor Clusters, Nanocrystals, and Quantum Dots," Science **271**, 933–937 (1996).

[23] H. Zollinger, *Color Chemistry: Syntheses, Properties, and Applications of Organic Dyes and Pigments* (John Wiley & Sons, 2003).

[24] R. M. Christie, "17 - Fluorescent dyes," in "Handbook of Textile and Industrial Dyeing," , vol. 1 of *Woodhead Publishing Series in Textiles*, M. Clark, ed. (Woodhead Publishing, 2011), pp. 562–587.

[25] A. Glenn, C. M. Loughlin, H. Ahmed, H. Akbari, S. Chandra, and S. McCormack, "The Viability of Organic Dyes in Luminescent Down-Shifting Layers for the Enhancement of Si Solar Cell Efficiency," Materials Science Forum **995**, 71–76 (2020).

[26] H. A. Höppe, "Recent Developments in the Field of Inorganic Phosphors," Angewandte Chemie International Edition **48**, 3572–3582 (2009).

[27] M. Alexandre, M. Chapa, S. Haque, M. J. Mendes, H. Águas, E. Fortunato, and R. Martins, "Optimum Luminescent Down-Shifting Properties for High Efficiency and Stable Perovskite Solar Cells," ACS Applied Energy Materials **2**, 2930–2938 (2019).

[28] D. Alonso-Álvarez, D. Ross, E. Klampaftis, K. R. McIntosh, S. Jia, P. Storiz, T. Stolz, and B. S. Richards, "Luminescent down-shifting experiment and modelling with multiple photovoltaic technologies," Progress in Photovoltaics: Research and Applications **23**, 479–497 (2015).

[29] P. Chung, H.-h. Chung, and P. H. Holloway, "Phosphor coatings to enhance Si photovoltaic cell performance," Journal of Vacuum Science & Technology A **25**, 61–66 (2007).

[30] T. Fix, A. Nonat, D. Imbert, S. Di Pietro, M. Mazzanti, A. Slaoui, and L. J. Charbonnière, "Enhancement of silicon solar cells by downshifting with Eu and Tb coordination complexes," Progress in Photovoltaics: Research and Applications **24**, 1251–1260 (2016).

[31] S. Liang, M. Zhang, G. M. Biesold, W. Choi, Y. He, Z. Li, D. Shen, and Z. Lin, "Recent Advances in Synthesis, Properties, and Applications of Metal Halide Perovskite Nanocrystals/Polymer Nanocomposites," Advanced Materials **33**, 2005888 (2021).

[32] K. R. McIntosh, G. Lau, J. N. Cotsell, K. Hanton, D. L. Bätzner, F. Bettiol, and B. S. Richards, "Increase in external quantum efficiency of encapsulated silicon solar cells from a luminescent down-shifting layer," Progress in Photovoltaics: Research and Applications **17**, 191–197 (2009).

[33] R. Rajeswari, N. Islavath, M. Raghavender, and L. Giribabu, "Recent Progress and Emerging Applications of Rare Earth Doped Phosphor Materials for Dye-Sensitized and Perovskite Solar Cells: A Review," The Chemical Record **20**, 65–88 (2020).

[34] R. Sekar, A. Ravitchandiran, and S. Angaiah, "Recent Advances and Challenges in Light Conversion Phosphor Materials for Third-Generation Quantum-Dot-Sensitized Photovoltaics," ACS Omega **7**, 35351–35360 (2022).

[35] G. Shao, C. Lou, and D. Xiao, "Enhancing the efficiency of solar cells by down shifting YAG: Ce3+ phosphors," Journal of Luminescence **157**, 344–348 (2015).

[36] A. Solodovnyk, K. Forberich, E. Stern, J. Krč, M. Topič, M. Batentschuk, B. Lipovšek, and C. J. Brabec, "Highly transmissive luminescent down-shifting layers filled with phosphor particles for photovoltaics," Optical Materials Express **5**, 1296–1305 (2015).

[37] E. Klampaftis, D. Ross, K. R. McIntosh, and B. S. Richards, "Enhancing the performance of solar cells via luminescent down-shifting of the incident spectrum: A review," Solar Energy Materials and Solar Cells **93**, 1182–1194 (2009).

[38] H. J. Hovel, R. T. Hodgson, and J. M. Woodall, "The effect of fluorescent wavelength shifting on solar cell spectral response," Solar Energy Materials **2**, 19–29 (1979).

[39] R. Lopez-Delgado, Y. Zhou, A. Zazueta-Raynaud, H. Zhao, J. E. Pelayo, A. Vomiero, M. E. Álvarez-Ramos, F. Rosei, and A. Ayon, "Enhanced conversion efficiency in Si solar cells employing photoluminescent down-shifting CdSe/CdS core/shell quantum dots," Scientific Reports **7**, 14104 (2017).

[40] Y. He, J. Liu, S.-J. Sung, and C.-h. Chang, "Downshifting and antireflective thin films for solar module power enhancement," Materials & Design **201**, 109454 (2021).

[41] "Instrumentation for Fluorescence Spectroscopy," in "Principles of Fluorescence Spectroscopy," , J. R. Lakowicz, ed. (Springer US, Boston, MA, 2006), pp. 27–61.

[42] S. K. E. Hill, R. Connell, J. Held, C. Peterson, L. Francis, M. A. Hillmyer, V. E. Ferry, and U. Kortshagen, "Poly(methyl methacrylate) Films with High Concentrations of Silicon Quantum Dots for Visibly Transparent Luminescent Solar Concentrators," ACS Applied Materials & Interfaces **12**, 4572–4578 (2020).

[43] J. Keil, Y. Liu, U. Kortshagen, and V. E. Ferry, "Bilayer Luminescent Solar Concentrators with Enhanced Absorption and Efficiency for Agrivoltaic Applications," ACS Applied Energy Materials (2021).

[44] F. Ye, W. Deng, W. Guo, R. Liu, D. Chen, Y. Chen, Y. Yang, N. Yuan, J. Ding, Z. Feng, P. P. Altermatt, and P. J. Verlinden, "22.13% Efficient industrial p-type mono PERC solar cell," in "2016 IEEE 43rd Photovoltaic Specialists Conference (PVSC)," (2016), pp. 3360–3365.

[45] V. I. Klimov, T. A. Baker, J. Lim, K. A. Velizhanin, and H. McDaniel, "Quality Factor of Luminescent Solar Concentrators and Practical Concentration Limits Attainable with Semiconductor Quantum Dots," ACS Photonics **3**, 1138–1148 (2016).

[46] H. Li, K. Wu, J. Lim, H.-J. Song, and V. I. Klimov, "Doctor-blade deposition of quantum dots onto standard window glass for low-loss large-area luminescent solar concentrators," Nature Energy **1**, 1–9 (2016).

[47] F. Meinardi, F. Bruni, and S. Brovelli, "Luminescent solar concentrators for building-integrated photovoltaics," Nature Reviews Materials **2**, 17072 (2017).

[48] C. Corrado, S. W. Leow, M. Osborn, I. Carbone, K. Hellier, M. Short, G. Alers, and S. A. Carter, "Power generation study of luminescent solar concentrator greenhouse," Journal of Renewable and Sustainable Energy **8**, 043502 (2016).

[49] C. H. Parrish, D. Hebert, A. Jackson, K. Ramasamy, H. McDaniel, G. A. Giacomelli, and M. R. Bergren, "Optimizing spectral quality with quantum dots to enhance crop yield in controlled environments," Communications Biology **4**, 1–9 (2021).

[50] G. Bai, M.-K. Tsang, and J. Hao, "Luminescent Ions in Advanced Composite Materials for Multifunctional Applications," Advanced Functional Materials **26**, 6330–6350 (2016).

[51] D. Yu, T. Yu, H. Lin, S. Zhuang, and D. Zhang, "Recent Advances in Luminescent Downconversion: New Materials, Techniques, and Applications in Solar Cells," Advanced Optical Materials **10**, 2200014 (2022).

[52] T. J. Milstein, K. T. Kluherz, D. M. Kroupa, C. S. Erickson, J. J. De Yoreo, and D. R. Gamelin, "Anion Exchange and the Quantum-Cutting Energy Threshold in Ytterbium-Doped CsPb(Cl1−xBrx)3 Perovskite Nanocrystals," Nano Letters **19**, 1931–1937 (2019).

[53] M. J. Crane, D. M. Kroupa, J. Y. Roh, R. T. Anderson, M. D. Smith, and D. R. Gamelin, "Single-Source Vapor Deposition of Quantum-Cutting Yb3+:CsPb(Cl1−xBrx)3 and Other Complex Metal-Halide Perovskites," ACS Applied Energy Materials **2**, 4560–4565 (2019).

[54] D. M. Kroupa, M. Vörös, N. P. Brawand, B. W. McNichols, E. M. Miller, J. Gu, A. J. Nozik, A. Sellinger, G. Galli, and M. C. Beard, "Tuning colloidal quantum dot band edge positions through solution-phase surface chemistry modification," Nature Communications **8**, 15257 (2017).

[55] M. J. Crane, D. M. Kroupa, and D. R. Gamelin, "Detailed-balance analysis of Yb 3+ :CsPb(Cl 1-x Br x) 3 quantum-cutting layers for high-efficiency photovoltaics under real-world conditions," Energy & Environmental Science **12**, 2486–2495 (2019).

[56] Z. J. Yu, M. Leilaeioun, and Z. Holman, "Selecting tandem partners for silicon solar cells," Nature Energy **1**, 1–4 (2016).

[57] Z. J. Yu, K. C. Fisher, B. M. Wheelwright, R. P. Angel, and Z. C. Holman, "PVMirror: A New Concept for Tandem Solar Cells and Hybrid Solar Converters," IEEE Journal of Photovoltaics **5**, 1791–1799 (2015).

[58] J. M. Russo, D. Zhang, M. Gordon, S. D. Vorndran, Y. Wu, and R. K. Kostuk, "Grating-over-lens concentrating photovoltaic spectrum splitting systems with volume holographic optical elements," in "High and Low Concentrator Systems for Solar Electric Applications VIII," , vol. 8821 (SPIE, 2013), vol. 8821, pp. 40–47.

[59] F. Fu, J. Li, T. C.-J. Yang, H. Liang, A. Faes, Q. Jeangros, C. Ballif, and Y. Hou, "Monolithic Perovskite-Silicon Tandem Solar Cells: From the Lab to Fab?" Advanced Materials **34**, 2106540 (2022).

[60] A. C. Tamboli, D. C. Bobela, A. Kanevce, T. Remo, K. Alberi, and M. Woodhouse, "Low-Cost CdTe/Silicon Tandem Solar Cells," IEEE Journal of Photovoltaics **7**, 1767–1772 (2017).

[61] E. L. Warren, W. E. McMahon, M. Rienäcker, K. T. VanSant, R. C. Whitehead, R. Peibst, and A. C. Tamboli, "A Taxonomy for Three-Terminal Tandem Solar Cells," ACS Energy Letters **5**, 1233–1242 (2020).

[62] "International Technology Roadmap for Photovoltaic (ITRPV) - vdma.org - VDMA," https://www.vdma.org/international-technology-roadmap-photovoltaic.

[63] K. Wu, H. Li, and V. I. Klimov, "Tandem luminescent solar concentrators based on engineered quantum dots," Nature Photonics **12**, 105–110 (2018).

[64] H. Zhao, D. Benetti, X. Tong, H. Zhang, Y. Zhou, G. Liu, D. Ma, S. Sun, Z. M. Wang, Y. Wang, and F. Rosei, "Efficient and stable tandem luminescent solar concentrators based on carbon dots and perovskite quantum dots," Nano Energy **50**, 756–765 (2018).

[65] G. Liu, H. Zhao, F. Diao, Z. Ling, and Y. Wang, "Stable tandem luminescent solar concentrators based on CdSe/CdS quantum dots and carbon dots," Journal of Materials Chemistry C **6**, 10059–10066 (2018).

[66] T. A. Cohen, T. J. Milstein, D. M. Kroupa, J. Devin MacKenzie, C. K. Luscombe, and D. R. Gamelin, "Quantum-cutting Yb 3+ -doped perovskite nanocrystals for monolithic bilayer luminescent solar concentrators," Journal of Materials Chemistry A **7**, 9279–9288 (2019).

[67] P.-H. Chuang, C. C. Lin, and R.-S. Liu, "Emission-Tunable CuInS2/ZnS Quantum Dots: Structure, Optical Properties, and Application in White Light-Emitting Diodes with High Color Rendering Index," ACS Applied Materials & Interfaces **6**, 15379–15387 (2014).

[68] L. Zdražil, S. Kalytchuk, K. Holá, M. Petr, O. Zmeškal, Š. Kment, A. L. Rogach, and R. Zbořil, "A carbon dot-based tandem luminescent solar concentrator," Nanoscale **12**, 6664–6672 (2020).

[69] A. Anand, M. L. Zaffalon, G. Gariano, A. Camellini, M. Gandini, R. Brescia, C. Capitani, F. Bruni, V. Pinchetti, M. Zavelani-Rossi, F. Meinardi, S. A. Crooker, and S. Brovelli, "Evidence for the Band-Edge Exciton of CuInS2 Nanocrystals Enables Record Efficient Large-Area Luminescent Solar Concentrators," Advanced Functional Materials **30**, 1906629 (2020).

[70] R. Connell, J. Keil, C. Peterson, M. A. Hillmyer, and V. E. Ferry, "CdSe/CdS–poly(cyclohexylethylene) thin film luminescent solar concentrators," APL Materials **7**, 101123 (2019).

[71] S. K. E. Hill, R. Connell, C. Peterson, J. Hollinger, M. A. Hillmyer, U. Kortshagen, and V. E. Ferry, "Silicon Quantum Dot–Poly(methyl methacrylate) Nanocomposites with Reduced Light Scattering for Luminescent Solar Concentrators," ACS Photonics **6**, 170–180 (2019).

[72] J. Benick, A. Richter, R. Müller, H. Hauser, F. Feldmann, P. Krenckel, S. Riepe, F. Schindler, M. C. Schubert, M. Hermle, A. W. Bett, and S. W. Glunz, "High-Efficiency n-Type HP mc Silicon Solar Cells," IEEE Journal of Photovoltaics **7**, 1171–1175 (2017).

[73] G. J. Bauhuis, P. Mulder, E. J. Haverkamp, J. C. C. M. Huijben, and J. J. Schermer, "26.1% thin-film GaAs solar cell using epitaxial lift-off," Solar Energy Materials and Solar Cells **93**, 1488–1491 (2009).

[74] D. Şahin, B. Ilan, and D. F. Kelley, "Monte-Carlo simulations of light propagation in luminescent solar concentrators based on semiconductor nanoparticles," Journal of Applied Physics **110**, 033108 (2011).

[75] C. Yang, D. Liu, M. Bates, M. C. Barr, and R. R. Lunt, "How to Accurately Report Transparent Solar Cells," Joule **3**, 1803–1809 (2019).

[76] I. Sychugov, "Analytical description of a luminescent solar concentrator," Optica **6**, 1046–1049 (2019).

[77] C. Pu and X. Peng, "To Battle Surface Traps on CdSe/CdS Core/Shell Nanocrystals: Shell Isolation versus Surface Treatment," Journal of the American Chemical Society **138**, 8134–8142 (2016).

[78] C. Bersani, A. Ouammi, R. Sacile, and E. Zero, "Model Predictive Control of Smart Greenhouses as the Path towards Near Zero Energy Consumption," Energies **13**, 1–17 (2020).

[79] L. La Notte, L. Giordano, E. Calabrò, R. Bedini, G. Colla, G. Puglisi, and A. Reale, "Hybrid and organic photovoltaics for greenhouse applications," Applied Energy **278**, 115582 (2020).

[80] G. A. Barron-Gafford, M. A. Pavao-Zuckerman, R. L. Minor, L. F. Sutter, I. Barnett-Moreno, D. T. Blackett, M. Thompson, K. Dimond, A. K. Gerlak, G. P. Nabhan, and J. E. Macknick, "Agrivoltaics provide mutual benefits across the food–energy–water nexus in drylands," Nature Sustainability **2**, 848–855 (2019).

[81] Q. Li and C. Kubota, "Effects of supplemental light quality on growth and phytochemicals of baby leaf lettuce," Environmental and Experimental Botany **67**, 59–64 (2009).

[82] M. A. Mickens, E. J. Skoog, L. E. Reese, P. L. Barnwell, L. E. Spencer, G. D. Massa, and R. M. Wheeler, "A strategic approach for investigating light recipes for 'Outredgeous' red romaine lettuce using white and monochromatic LEDs," Life Sciences in Space Research **19**, 53–62 (2018).

[83] M. C. Snowden, K. R. Cope, and B. Bugbee, "Sensitivity of Seven Diverse Species to Blue and Green Light: Interactions with Photon Flux," PLOS ONE **11**, e0163121 (2016).

[84] K. R. Cope, M. C. Snowden, and B. Bugbee, "Photobiological interactions of blue light and photosynthetic photon flux: Effects of monochromatic and broad-spectrum light sources," Photochemistry and Photobiology **90**, 574–584 (2014 May-Jun).

[85] O. Chen, X. Chen, Y. Yang, J. Lynch, H. Wu, J. Zhuang, and Y. C. Cao, "Synthesis of Metal–Selenide Nanocrystals Using Selenium Dioxide as the Selenium Precursor," Angewandte Chemie International Edition **47**, 8638–8641 (2008).

[86] D. B. Dement, M. Puri, and V. E. Ferry, "Determining the Complex Refractive Index of Neat CdSe/CdS Quantum Dot Films," The Journal of Physical Chemistry C **122**, 21557–21568 (2018).

[87] "Standard Test Method for Haze and Luminous Transmittance of Transparent Plastics 1," .

[88] Y. Yuan and M. Krüger, "Polymer-Nanocrystal Hybrid Materials for Light Conversion Applications," Polymers **4**, 1–19 (2012).

[89] F. Jin, M.-L. Zheng, M.-L. Zhang, Z.-S. Zhao, and X.-M. Duan, "A facile layer-by-layer assembly method for the fabrication of fluorescent polymer/quantum dot nanocomposite thin films," RSC Advances **4**, 33206–33214 (2014).

[90] J. Bomm, A. Büchtemann, A. Fiore, L. Manna, J. H. Nelson, D. Hill, and W. G. J. H. M. van Sark, "Fabrication and spectroscopic studies on highly luminescent CdSe/CdS nanorod polymer composites," Beilstein Journal of Nanotechnology **1**, 94–100 (2010).

[91] F. Meinardi, A. Colombo, K. A. Velizhanin, R. Simonutti, M. Lorenzon, L. Beverina, R. Viswanatha, V. I. Klimov, and S. Brovelli, "Large-area luminescent solar concentrators based on 'Stokes-shift-engineered' nanocrystals in a mass-polymerized PMMA matrix," Nature Photonics **8**, 392–399 (2014).

[92] H. Jeon, J. H. Jo, K. P. Yang, and K. Lee, "Improvement in efficiency and stability of quantum dot/polymer nanocomposite film for light-emitting diodes using refractive index-controlled quantum dot–silica hybrid particles," Journal of Materials Chemistry C **7**, 11764–11769 (2019).

[93] H. Du, R.-C. A. Fuh, J. Li, L. A. Corkan, and J. S. Lindsey, "PhotochemCAD‡: A Computer-Aided Design and Research Tool in Photochemistry," Photochemistry and Photobiology **68**, 141–142 (1998).

[94] S. Hemming, V. Mohammadkhani, and T. Dueck, "DIFFUSE GREENHOUSE COVERING MATERIALS - MATERIAL TECHNOLOGY, MEASUREMENTS AND EVALUATION OF OPTICAL PROPERTIES," Acta Horticulturae pp. 469–475 (2008).

[95] H. C. Bauser, C. R. Bukowsky, M. Phelan, W. Weigand, D. R. Needell, Z. C. Holman, and H. A. Atwater, "Photonic Crystal Waveguides for >90% Light Trapping Efficiency in Luminescent Solar Concentrators," ACS Photonics (2020).

[96] R. Connell, "Controlling Optical Transport in Luminescent Solar Concentrators," Doctoral, University of Minnesota, Minneapolis (2019).

[97] G. Pennisi, F. Orsini, S. Blasioli, A. Cellini, A. Crepaldi, I. Braschi, F. Spinelli, S. Nicola, J. A. Fernandez, C. Stanghellini, G. Gianquinto, and L. F. M. Marcelis, "Resource use efficiency of indoor lettuce (Lactuca sativa L.) cultivation as affected by red:blue ratio provided by LED lighting," Scientific Reports **9**, 14127 (2019).

[98] J. Zhou, J. Z. Wang, T. Hang, and P. P. Li, "Photosynthetic characteristics and growth performance of lettuce (Lactuca sativa L.) under different light/dark cycles in mini plant factories," Photosynthetica **58**, 740–747 (2020).

[99] L. Shen, R. Lou, Y. Park, Y. Guo, E. J. Stallknecht, Y. Xiao, D. Rieder, R. Yang, E. S. Runkle, and X. Yin, "Increasing greenhouse production by spectral-shifting and unidirectional light-extracting photonics," Nature Food **2**, 434–441 (2021).

[100] S. Hemming, V. Mohammadkhani, and T. A. Dueck, "Diffuse greenhouse covering materials material technology, measurements and evaluation of optical properties," in "International Workshop on Greenhouse Environmental Control and Crop Production in Semi-Arid Regions," (ISHS, 2008), pp. 469–476.

[101] G. D. Farquhar and M. L. Roderick, "Pinatubo, Diffuse Light, and the Carbon Cycle," Science **299**, 1997–1998 (2003).

[102] L. Gu, D. D. Baldocchi, S. C. Wofsy, J. W. Munger, J. J. Michalsky, S. P. Urbanski, and T. A. Boden, "Response of a Deciduous Forest to the Mount Pinatubo Eruption: Enhanced Photosynthesis," Science **299**, 2035–2038 (2003).

[103] S. Hemming, N. Van Der Braak, T. Dueck, R. Jongschaap, and N. Marissen, "FILTERING NATURAL LIGHT BY THE GREENHOUSE COVERING USING MODEL SIMULATIONS - MORE PRODUCTION AND BETTER PLANT QUALITY BY DIFFUSE LIGHT?" Acta Horticulturae pp. 105–110 (2006).

[104] S. Hemming, T. Dueck, J. Janse, and F. Van Noort, "THE EFFECT OF DIFFUSE LIGHT ON CROPS," Acta Horticulturae pp. 1293–1300 (2008).

[105] L. Shen, R. Lou, and X. Yin, "Asymmetrical interface design for unidirectional light extraction from spectrum conversion films," Optics Express **30**, 4642–4654 (2022).

[106] H.-W. Su and W.-C. Chen, “High refractive index polyimide–nanocrystalline-titania hybrid optical materials,” Journal of Materials Chemistry **18**, 1139–1145 (2008).

[107] J. L. H. Chau, C.-T. Tung, Y.-M. Lin, and A.-K. Li, “Preparation and optical properties of titania/epoxy nanocomposite coatings,” Materials Letters **62**, 3416–3418 (2008).

[108] J. Liu, Y. Gao, D. Cao, L. Zhang, and Z. Guo, “Nanoparticle Dispersion and Aggregation in Polymer Nanocomposites: Insights from Molecular Dynamics Simulation,” Langmuir **27**, 7926–7933 (2011).

[109] H. I. Elim, B. Cai, Y. Kurata, O. Sugihara, T. Kaino, T. Adschiri, A.-L. Chu, and N. Kambe, “Refractive Index Control and Rayleigh Scattering Properties of Transparent TiO2 Nanohybrid Polymer,” The Journal of Physical Chemistry B **113**, 10143–10148 (2009).

[110] C. F. Bohren and D. R. Huffman, *Absorption and Scattering of Light by Small Particles* (John Wiley & Sons, 2008).

[111] Z. Xu, M. Portnoi, and I. Papakonstantinou, “Micro-cone arrays enhance outcoupling efficiency in horticulture luminescent solar concentrators,” Optics Letters **48**, 183–186 (2023).

[112] O. M. ten Kate, M. de Jong, H. T. Hintzen, and E. van der Kolk, “Efficiency enhancement calculations of state-of-the-art solar cells by luminescent layers with spectral shifting, quantum cutting, and quantum tripling function,” Journal of Applied Physics **114**, 084502 (2013).

[113] Z. R. Abrams, A. Niv, and X. Zhang, “Solar energy enhancement using down-converting particles: A rigorous approach,” Journal of Applied Physics **109**, 114905 (2011).

[114] D. M. Kroupa, M. J. Crane, J. S. Silvia, and D. R. Gamelin, “Ray-Tracing Analysis of Module-Level Power Generation from Quantum-Cutting Ytterbium-Doped Metal-Halide Perovskites,” in “2020 47th IEEE Photovoltaic Specialists Conference (PVSC),” (2020), pp. 0868–0874.

[115] T. C. Choy, *Effective Medium Theory: Principles and Applications* (Oxford University Press, 2015).

[116] M. R. Vogt, H. Holst, H. Schulte-Huxel, S. Blankemeyer, R. Witteck, D. Hinken, M. Winter, B. Min, C. Schinke, I. Ahrens, M. Köntges, K. Bothe, and R. Brendel, “Optical Constants of UV Transparent EVA and the Impact on the PV Module Output Power under Realistic Irradiation,” Energy Procedia **92**, 523–530 (2016).

[117] T. H. Fung, M. U. Khan, Y. Zhang, N. J. Western, D. N. R. Payne, K. R. Mclntosh, and M. D. Abbott, “Improved Ray Tracing on Random Pyramid Texture via Application of Phong Scattering,” IEEE Journal of Photovoltaics **9**, 591–600 (2019).

[118] H. M. Ghaithan, Z. A. Alahmed, S. M. H. Qaid, and A. S. Aldwayyan, “Structural, Electronic, and Optical Properties of CsPb(Br1-xClx)3 Perovskite: First-Principles Study with PBE-GGA and mBJ-GGA Methods,” Materials (Basel, Switzerland) **13**, 4944 (2020).

[119] M. Ahmad, G. Rehman, L. Ali, M. Shafiq, R. Iqbal, R. Ahmad, T. Khan, S. Jalali-Asadabadi, M. Maqbool, and I. Ahmad, “Structural, electronic and optical properties of CsPbX3 (X=Cl, Br, I) for energy storage and hybrid solar cell applications,” Journal of Alloys and Compounds **705**, 828–839 (2017).

[120] “Standard Tables for Reference Solar Spectral Irradiances: Direct Normal and Hemispherical on 37° Tilted Surface,” http://www.astm.org/g0173-03r20.html.

[121] B. D. Guenther, *Modern Optics* (OUP Oxford, 2015).

[122] G. Oreski, A. Omazic, G. C. Eder, Y. Voronko, L. Neumaier, W. Mühleisen, C. Hirschl, G. Ujvari, R. Ebner, and M. Edler, “Properties and degradation behaviour of polyolefin encapsulants for photovoltaic modules,” Progress in Photovoltaics: Research and Applications **28**, 1277–1288 (2020).

[123] M. Kaur, A. Sharma, M. Olutas, O. Erdem, A. Kumar, M. Sharma, and H. V. Demir, “Cd-free Cu-doped ZnInS/ZnS Core/Shell Nanocrystals: Controlled Synthesis And Photophysical Properties,” Nanoscale Research Letters **13**, 182 (2018).

[124] S. Kurtz, K. Whitfield, G. TamizhMani, M. Koehl, D. Miller, J. Joyce, J. Wohlgemuth, N. Bosco, M. Kempe, and T. Zgonena, “Evaluation of high-temperature exposure of photovoltaic modules,” Progress in Photovoltaics: Research and Applications **19**, 954–965 (2011).

[125] I. M. Slauch, M. G. Deceglie, T. J. Silverman, and V. E. Ferry, “Optical approaches for passive thermal management in c-Si photovoltaic modules,” Cell Reports Physical Science **2**, 100430 (2021).

[126] T. J. Silverman, M. G. Deceglie, I. Subedi, N. J. Podraza, I. M. Slauch, V. E. Ferry, and I. Repins, “Reducing Operating Temperature in Photovoltaic Modules,” IEEE Journal of Photovoltaics **8**, 532–540 (2018).

[127] I. M. Slauch, M. G. Deceglie, T. J. Silverman, and V. E. Ferry, “Spectrally Selective Mirrors with Combined Optical and Thermal Benefit for Photovoltaic Module Thermal Management,” ACS Photonics **5**, 1528–1538 (2018).

[128] F. Martinho, “Challenges for the future of tandem photovoltaics on the path to terawatt levels: A technology review,” Energy & Environmental Science **14**, 3840–3871 (2021).

[129] P. J. Verlinden, “Future challenges for photovoltaic manufacturing at the terawatt level,” Journal of Renewable and Sustainable Energy **12**, 053505 (2020).

[130] M. Yamaguchi, K.-H. Lee, K. Araki, and N. Kojima, "A review of recent progress in heterogeneous silicon tandem solar cells," Journal of Physics D: Applied Physics **51**, 133002 (2018).

[131] C. Ballif, F.-J. Haug, M. Boccard, P. J. Verlinden, and G. Hahn, "Status and perspectives of crystalline silicon photovoltaics in research and industry," Nature Reviews Materials **7**, 597–616 (2022).

[132] J. Werner, B. Niesen, and C. Ballif, "Perovskite/Silicon Tandem Solar Cells: Marriage of Convenience or True Love Story? – An Overview," Advanced Materials Interfaces **5**, 1700731 (2018).

[133] M. Carmody, S. Mallick, J. Margetis, R. Kodama, T. Biegala, D. Xu, P. Bechmann, J. W. Garland, and S. Sivananthan, "Single-crystal II-VI on Si single-junction and tandem solar cells," Applied Physics Letters **96**, 153502 (2010).

[134] G. M. Hanket, B. E. McCandless, W. A. Buchanan, S. Fields, and R. W. Birkmire, "Design of a vapor transport deposition process for thin film materials," Journal of Vacuum Science & Technology A: Vacuum, Surfaces, and Films **24**, 1695–1701 (2006).

[135] T. Ablekim, J. N. Duenow, X. Zheng, H. Moutinho, J. Moseley, C. L. Perkins, S. W. Johnston, P. O'Keefe, E. Colegrove, D. S. Albin, M. O. Reese, and W. K. Metzger, "Thin-Film Solar Cells with 19% Efficiency by Thermal Evaporation of CdSe and CdTe," ACS Energy Letters **5**, 892–896 (2020).

[136] A. Romeo, E. Artegiani, and D. Menossi, "Low substrate temperature CdTe solar cells: A review," Solar Energy **175**, 9–15 (2018).

[137] F. He, J. Li, S. Lin, W. Long, L. Wu, X. Hao, J. Zhang, and L. Feng, "Semitransparent CdTe solar cells with CdCl2 treated absorber towards the enhanced photovoltaic conversion efficiency," Solar Energy **214**, 196–204 (2021).

[138] S. Chander and M. S. Dhaka, "Optimization of physical properties of vacuum evaporated CdTe thin films with the application of thermal treatment for solar cells," Materials Science in Semiconductor Processing **40**, 708–712 (2015).

[139] S. Chander and M. S. Dhaka, "Physical properties of vacuum evaporated CdTe thin films with post-deposition thermal annealing," Physica E: Low-dimensional Systems and Nanostructures **73**, 35–39 (2015).

[140] M. Isah, K. S. Rahman, C. Doroody, M. N. Harif, H. N. Rosly, K. Sopian, S. K. Tiong, and N. Amin, "Design optimization of CdTe/Si tandem solar cell using different transparent conducting oxides as interconnecting layers," Journal of Alloys and Compounds **870**, 159351 (2021).

[141] A. Rouhbakhshmeghrazi, M. Madadi, A. Rouhbakhshmeghrazi, and M. Madadi, "Novel Design of polycrystalline CdTe/Si Tandem Solar Cells Using SiO2/TiO2 Distributed Bragg Reflector," Tecciencia **15**, 67–75 (2020).

[142] M. Jošt, L. Kegelmann, L. Korte, and S. Albrecht, "Monolithic Perovskite Tandem Solar Cells: A Review of the Present Status and Advanced Characterization Methods Toward 30% Efficiency," Advanced Energy Materials **10**, 1904102 (2020).

[143] J. P. Mailoa, M. Lee, I. M. Peters, T. Buonassisi, A. Panchula, and D. N. Weiss, "Energy-yield prediction for II–VI-based thin-film tandem solar cells," Energy & Environmental Science **9**, 2644–2653 (2016).

[144] W. Qarony, M. I. Hossain, V. Jovanov, A. Salleo, D. Knipp, and Y. H. Tsang, "Influence of Perovskite Interface Morphology on the Photon Management in Perovskite/Silicon Tandem Solar Cells," ACS Applied Materials & Interfaces **12**, 15080–15086 (2020).

[145] F. M. T. Enam, K. S. Rahman, M. I. Kamaruzzaman, K. Sobayel, P. Chelvanathan, B. Bais, M. Akhtaruzzaman, A. R. M. Alamoud, and N. Amin, "Design prospects of cadmium telluride/silicon (CdTe/Si) tandem solar cells from numerical simulation," Optik **139**, 397–406 (2017).

[146] X. Wu, J. Zhou, A. Duda, J. C. Keane, T. Gessert, Y. Yan, and R. Noufi, "13·9%-efficient CdTe polycrystalline thin-film solar cells with an infrared transmission of $\sim$50%," Progress in Photovoltaics: Research and Applications **14**, 471–483 (2006).

[147] J. Li, F. He, X. Hao, S. Lin, W. Long, T. Gan, L. Wu, J. Zhang, and L. Feng, "Semi-transparent CdTe solar cell with over 70% near-infrared transmittance," Journal of Materials Science: Materials in Electronics **31**, 18198–18208 (2020).

[148] X. Wen, Z. Lu, X. Sun, Y. Xiang, Z. Chen, J. Shi, I. Bhat, G.-C. Wang, M. Washington, and T.-M. Lu, "Epitaxial CdTe Thin Films on Mica by Vapor Transport Deposition for Flexible Solar Cells," ACS Applied Energy Materials **3**, 4589–4599 (2020).

[149] O. Toma, L. Ion, M. Girtan, and S. Antohe, "Optical, morphological and electrical studies of thermally vacuum evaporated CdTe thin films for photovoltaic applications," Solar Energy **108**, 51–60 (2014).

[150] J. M. Kestner, S. McElvain, S. Kelly, T. R. Ohno, L. M. Woods, and C. A. Wolden, "An experimental and modeling analysis of vapor transport deposition of cadmium telluride," Solar Energy Materials and Solar Cells **83**, 55–65 (2004).

[151] B. McCandless, W. Buchanan, G. Sriramagiri, C. Thompson, J. Duenow, D. Albin, S. A. Jensen, J. Moseley, M. Al-Jassim, and W. K. Metzger, "Enhanced p-Type Doping in Polycrystalline CdTe Films: Deposition and Activation," IEEE Journal of Photovoltaics **9**, 912–917 (2019).

[152] X. Wu, "High-efficiency polycrystalline CdTe thin-film solar cells," Solar Energy **77**, 803–814 (2004).

[153] B. McCandless, R. Birkmire, and W. Buchanan, "Vapor transport deposition of cadmium telluride films," in "Conference Record of the Twenty-Ninth IEEE Photovoltaic Specialists Conference, 2002.", (2002), pp. 547–550.

[154] R. S. Yavorskyi, "Features of optical properties of high stable CdTe photovoltaic absorber layer," Physics and Chemistry of Solid State **21**, 243–253 (2020).

[155] M. A. Islam, Q. Huda, M. S. Hossain, M. M. Aliyu, M. R. Karim, K. Sopian, and N. Amin, "High quality 1 Mm thick CdTe absorber layers grown by magnetron sputtering for solar cell application," Current Applied Physics **13**, S115–S121 (2013).

[156] R. Yavorskyi, L. Nykyruy, G. Wisz, P. Potera, S. Adamiak, and Sz. Górny, "Structural and optical properties of cadmium telluride obtained by physical vapor deposition technique," Applied Nanoscience **9**, 715–724 (2019).

[157] S. K. Pandey, U. Tiwari, R. Raman, C. Prakash, V. Krishna, V. Dutta, and K. Zimik, "Growth of cubic and hexagonal CdTe thin films by pulsed laser deposition," Thin Solid Films **473**, 54–57 (2005).

[158] H. M. Al-Allak, A. W. Brinkman, H. Richter, and D. Bonnet, "Dependence of $\{$CdS$\}$/$\{$CdTe$\}$ thin film solar cell characteristics on the processing conditions," Journal of Crystal Growth **159**, 910–915 (1996).

[159] J. Müller, B. Rech, J. Springer, and M. Vanecek, "TCO and light trapping in silicon thin film solar cells," Solar Energy **77**, 917–930 (2004).

[160] M. A. Green, "Lambertian light trapping in textured solar cells and light-emitting diodes: Analytical solutions," Progress in Photovoltaics: Research and Applications **10**, 235–241 (2002).

[161] H. Sai, Y. Kanamori, K. Arafune, Y. Ohshita, and M. Yamaguchi, "Light trapping effect of submicron surface textures in crystalline Si solar cells," Progress in Photovoltaics: Research and Applications **15**, 415–423 (2007).

[162] J. F. Owen, R. K. Chang, and P. W. Barber, "Internal electric field distributions of a dielectric cylinder at resonance wavelengths," Optics Letters **6**, 540–542 (1981).

[163] D. S. Benincasa, P. W. Barber, J.-Z. Zhang, W.-F. Hsieh, and R. K. Chang, "Spatial distribution of the internal and near-field intensities of large cylindrical and spherical scatterers," Applied Optics **26**, 1348–1356 (1987).

[164] O. V. Minin and I. V. Minin, "Optical Phenomena in Mesoscale Dielectric Particles," Photonics **8**, 591 (2021).

[165] P. Chýlek, J. D. Pendleton, and R. G. Pinnick, "Internal and near-surface scattered field of a spherical particle at resonant conditions," Applied Optics **24**, 3940–3942 (1985).

[166] C. Rockstuhl, F. Lederer, K. Bittkau, and R. Carius, "Light localization at randomly textured surfaces for solar-cell applications," Applied Physics Letters **91**, 171104 (2007).

[167] A. Heifetz, S.-C. Kong, A. V. Sahakian, A. Taflove, and V. Backman, “Photonic Nanojets,” Journal of Computational and Theoretical Nanoscience **6**, 1979–1992 (2009).

[168] A. Darafsheh, “Photonic nanojets and their applications,” Journal of Physics: Photonics **3**, 022001 (2021).

[169] C.-Y. Liu, O. V. Minin, and I. V. Minin, “First experimental observation of array of photonic jets from saw-tooth phase diffraction grating,” EPL (Europhysics Letters) **123**, 54003 (2018).

[170] S. Lecler, Y. Takakura, and P. Meyrueis, “Properties of a three-dimensional photonic jet,” Optics Letters **30**, 2641–2643 (2005).

[171] E. K. Macdonald and M. P. Shaver, “Intrinsic high refractive index polymers,” Polymer International **64**, 6–14 (2015).

[172] J.-g. Liu and M. Ueda, “High refractive index polymers: Fundamental research and practical applications,” Journal of Materials Chemistry **19**, 8907–8919 (2009).

[173] H.-J. Yen and G.-S. Liou, “A facile approach towards optically isotropic, colorless, and thermoplastic polyimidothioethers with high refractive index,” Journal of Materials Chemistry **20**, 4080–4084 (2010).

[174] F. W. Mont, J. K. Kim, M. F. Schubert, E. F. Schubert, and R. W. Siegel, “High-refractive-index TiO2-nanoparticle-loaded encapsulants for light-emitting diodes,” Journal of Applied Physics **103**, 083120 (2008).

[175] A. Goktas, E. Aslan, F. Arslan, and A. Kilic, “Characterization of multifunctional solution-processed Sn1-xZnxS nanostructured thin films for photosensitivity and photocatalytic applications,” Optical Materials **133**, 112984 (2022).

[176] A. Tumbul, A. Göktaş, M. Z. Zarbali, and F. Aslan, “Structural, morphological and optical properties of the vacuum-free processed CZTS thin film absorbers,” Materials Research Express **5**, 066408 (2018).

[177] B. Zhou, X. Yin, J. Zhang, G. Zeng, B. Li, J. Zhang, and L. Feng, “Numerical simulation of an innovative high efficiency solar cell with CdTe/Si composite absorption layer,” Optical Materials **110**, 110505 (2020).

[178] H. Gencer, A. Goktas, M. Gunes, H. I. Mutlu, and S. Atalay, “ELECTRICAL TRANSPORT AND MAGNETORESISTANCE PROPERTIES OF La0.67Ca0.33MnO3 FILM COATED ON PYREX GLASS SUBSTRATE,” International Journal of Modern Physics B **22**, 497–506 (2008).

[179] F. Mikailzade, H. Türkan, F. Önal, M. Zarbali, A. Göktaş, and A. Tumbul, “Structural and magnetic properties of polycrystalline Zn1-xMnxO films synthesized on glass and p-type Si substrates using Sol–Gel technique,” Applied Physics A **127**, 408 (2021).

[180] M. A. Green, E. D. Dunlop, J. Hohl-Ebinger, M. Yoshita, N. Kopidakis, and X. Hao, “Solar cell efficiency tables (version 56),” Progress in Photovoltaics: Research and Applications **28**, 629–638 (2020).

[181] Y. Liu, J. Keil, V. E. Ferry, and U. R. Kortshagen, “Energy and Thermal Performance Analysis of Quantum Dot Luminescent Solar Concentrators in Greenhouses,” Advanced Sustainable Systems **n/a**, 2300107.

[182] I. M. Slauch, M. G. Deceglie, T. J. Silverman, and V. E. Ferry, “Model for Characterization and Optimization of Spectrally Selective Structures to Reduce the Operating Temperature and Improve the Energy Yield of Photovoltaic Modules,” ACS Applied Energy Materials **2**, 3614–3623 (2019).

Appendix

A Optical Coupling Efficiency Calculations

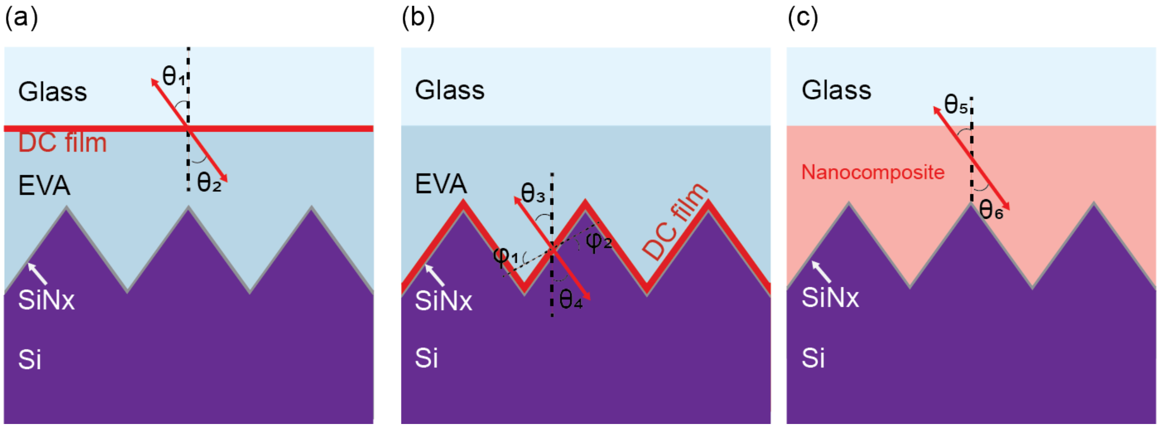

Figure A.1: Geometry diagrams of the emission angles for the (a) downconverting film on glass, (b) downconverting film on cell, and (c) nanocomposite configurations.

Figure A.1 shows the emission angles referred to when describing the optical coupling calculations (Equations A.1-A.5). For the downconverting film on glass configuration two modes were considered: light emitted upward that reflects off the glass/ARC/air interface and down to the Si, and light emitted downward through the EVA into the Si. The optical coupling efficiency for the downconverting film on glass configuration is described by the following equation:

$$\begin{aligned}\eta_{opt,DC}(h,\lambda) = [2\pi \int_0^{\frac{\pi}{2}-\xi} & F_{rad}^{glass}(h,\theta_1,\lambda) R_{ARC}(\theta_1,\lambda) T_{DC}(\theta_1',\lambda) \\ & *(1-A_{glass}(\theta_1,\lambda))^2 (1-A_{EVA}(\theta_1',\lambda)) sin(\theta_1)\, d\theta_1 \\ +2\pi \int_0^{\frac{\pi}{2}-\xi} F_{rad}^{EVA}(h,\theta_2,\lambda) & T_{SiN}(\theta_2,\lambda)(1-A_{EVA}(\theta_2,\lambda)) sin(\theta_2)\, d\theta_2]/F(h,\lambda)\end{aligned} \tag{A.1}$$

where $R_{ARC}(\theta,\lambda)$ is the reflection off the glass/ARC/air interface, $T_{DC}(\theta,\lambda)$ is the transmission through the downconverting film from the glass into EVA, $T_{SiN}(\theta,\lambda)$ is the transmission through the SiN$_x$ into the Si while accounting for the pyramidal texturing, and $F(\lambda)$ is the Purcell factor. The glass and EVA are thick enough that they were assumed to be incoherent, but the absorption was accounted for with $A_{glass}(\theta,\lambda))$ and $A_{EVA}(\theta,\lambda))$, which are the absorption probabilities for glass and EVA. θ_1 and θ_2 are the emission angle into glass and EVA with respect to the downconverting film surface normal. θ_1' used for $T_{SiN}(\theta,\lambda)$ and $A_{EVA}(\theta,\lambda))$ represents the slight angle correction done to account for glass to EVA refraction. Reflection and transmission of the thin-films and interfaces are determined *via* transfer-matrix method calculations and Fresnel coefficients. The angle dependent light transmission and reflection off the pyramidal texturing of the Si/SiN$_x$/ARC surface was treated as a single interface and calculated following analytical methods reported in literature [182].

The downconverting film on cell configuration considered three modes of optical coupling into Si: light emitted upward into EVA that reflects back down to the cell, light emitted off one pyramid to an adjacent pyramid, and light emitted directly downward through the SiN$_x$ and into the Si. The angle-resolved power density radiated into the EVA ($F_{rad}^{EVA}(h,\theta_3,\phi_1,\lambda)$) from the downconverting film on cell configuration was first rotated by 54.7°, which is the expected angle of a pyramid side. The azimuthal angle ϕ was added because the rotation breaks the radial symmetry. If the z-component of the emission direction into EVA was negative (downward), the light was assumed to be incident on an adjacent pyramid and the coupling efficiency for every θ_3 and ϕ_1 angle is expressed by this equation:

$$\eta_{opt,DC}(h,\theta_3,\phi_1,\lambda) = \frac{F_{rad}^{EVA}(h,\theta_3,\phi_1,\lambda)T_{SiN}(\beta,\lambda)}{F(h,\lambda)} \tag{A.2}$$

where β is the angle of incidence on the adjacent pyramid, and in this case $T_{SiN}(\beta,\lambda)$ is calculated with transfer-matrix calculations. If the z-component of the emission direction into EVA is positive, the light was assumed to be emitted upward into EVA, and the angle-dependent coupling efficiency is defined as:

$$\begin{aligned}\eta_{opt,DC}(h,\theta_3,\phi_1,\lambda) = F_{rad}^{EVA}(h,\theta_3,\phi_1,\lambda))R_{ARC}(\theta_3',\lambda)T_{SiN}(\theta_3,\lambda)T_{EVA-Gl}(\theta_3,\lambda)\\ *T_{Gl-EVA}(\theta_3',\lambda)(1-A_{glass}(\theta_3',\lambda))^2(1-A_{EVA}(\theta_3,\lambda))^2/F(h,\lambda)\end{aligned} \tag{A.3}$$

$T_{EVA-Gl}(\theta,\lambda)$ and $T_{EVA-Gl}(\theta,\lambda)$ are transmission at the glass/EVA interface. The power radiated directly into Si $F_{rad}^{EVA}(h,\theta_4,\phi_2,\lambda))$ does not undergo any additional reflection or transmission, so the overall coupling efficiency for the downconverting film on cell configuration is described by the following equation:

$$\begin{aligned}\eta_{opt,DC}(h,\lambda) = \int_0^{2\pi}\int_0^{\frac{\pi}{2}-\xi} \eta_{opt,DC}(h,\theta_3,\phi_1,\lambda)\,d\theta_3\,d\phi_1\\ +\int_0^{2\pi}\int_0^{\frac{\pi}{2}-\xi} F_{rad}^{Si}(h,\theta_4,\phi_2,\lambda)/F(h,\lambda)\,d\theta_4\,d\phi_2\end{aligned} \tag{A.4}$$

The coupling efficiency calculation for the nanocrystal-EVA nanocomposite did not use data from FDTD simulations or the analytical solver due to the thicker EVA material. Instead, the dipole was assumed to have isotropic PL, and the interfacial interactions were determined similarly to the other configurations. The calculation was divided into two half-spaces and the coupling efficiency was calculated using the following:

$$
\begin{aligned}
\eta_{opt,DC}(\lambda) = [2\pi \int_0^{\frac{\pi}{2}-\xi} & T_{NC-Gl}(\theta_5,\lambda) R_{ARC}(\theta_5',\lambda) T_{Gl-NC}(\theta_5',\lambda) T_{SiN}(\theta_5,\lambda) \\
& (1 - A_{glass}(\theta_5',\lambda))^2 (1 - A_{EVA}(\theta_5,\lambda))(1 - A_{EVA}(\theta_5,\lambda))^{0.5} sin\theta_5 \, d\theta_5 \\
& + 2\pi \int_0^{\frac{\pi}{2}-\xi} T_{SiN}(\theta_6,\lambda)(1 - A_{EVA}(\theta_6,\lambda))^{0.5} sin\theta_6 /, \theta_6]/4\pi
\end{aligned}
\tag{A.5}
$$

where $T_{NC-Gl}(\theta,\lambda)$ and $T_{NC-Gl}(\theta,\lambda)$ are transmission from the nanocrystal-EVA nanocomposite material to the glass and *vice versa*. The wavelength dependent optical coupling efficiencies were averaged over the PL spectrum reported in Figure 5.5 to calculate a single value for each configuration.